DISS. ETH NO. 22853

Transport Mechanisms in Continuous Reaction Systems with Porous Structures

A thesis submitted to attain the degree of

DOCTOR OF SCIENCES of ETH ZURICH

(Dr. sc. ETH Zurich)

presented by

RICHARD HÄFELI

MSc ETH PE

born on October 19, 1985

citizen of Speicher (AR), Switzerland

accepted on the recommendation of

Prof. Dr. Dr. h.c. Philipp Rudolf von Rohr, examiner

Prof. Dr. Simon Kuhn, co-examiner

2015

Abstract

There is a trend in the chemical and pharmaceutical industries to shift from batch reactors to continuous tubular reactors. In the latter, internal structures can be used as catalyst support and static mixing elements. In multi-phase reactions, the internal structure can further serve to produce small droplets or bubbles. The present thesis investigates transport mechanisms in single- and multi-phase flow through a regular foam-like porous structure.

Theoretically, the conservation equations for mass, energy, and momentum describe concentration, temperature, and velocity. However, the exact geometry of a porous structure is often unknown. Furthermore, it can be computationally too expensive to model the entire reactor. Therefore, macroscopic models are used. In macroscopic models, the fluid and solid contained in the reactor are modeled as a continuum. The transport coefficients of these macroscopic models are investigated experimentally.

To investigate transport mechanisms on the microscopic scale, optical measurements were performed inside a porous structure. Porous structures were manufactured from WaterShed, a transparent solid used in rapid prototyping. In order to allow optical measurements inside this structure, the refractive index of the fluid was matched to that of the solid. Two fluids were used: anisole and an aqueous solution of sodium iodide and zinc iodide. Since anisole dissolves the porous structure, a varnish coating was used to increase its durability. The brine was found to be more convenient because it does not attack the porous structure. The proposed system of two fluids and the solid manufactured by rapid prototyping allows optical measurements in single- and two-phase flow by particle image velocimetry and laser induced fluorescence.

Using particle image velocimetry, the velocity field was investigated inside the porous structure. At a hydraulic Reynolds number of $Re_h > 300$, isotropy of velocity fluctuations was observed. Measurements with two

different fluids and with structures of two different dimensions were then
compared using scaling laws derived by employing Reynolds similarity.
The agreement between the experiments was satisfactory, even for quan-
tities known to contain a substantial degree of uncertainty, e.g., the
dissipation rate of turbulent kinetic energy. Employing the $k - \varepsilon$ model
of turbulence, the turbulent diffusivity was then estimated. When com-
pared with the macroscopic experiments, it was concluded that longitu-
dinal dispersion is mainly governed by differences in mean velocity while
turbulent transport plays a minor role at hydraulic Reynolds numbers
between 150 and 450.

Finally, two-phase flow through a foam-like porous structure and a
Sulzer SMX$^{\text{TM}}$ static mixing element was compared. The droplet size
and position within the internal structures were observed by laser-induced
fluorescence. It is recognized that at low flowrates, droplets follow pre-
ferred paths, whereas at higher flowrates, they are more homogeneously
distributed within the structures. The droplet size distribution was
found to be well represented by the Sauter mean diameter. Measuring
along the axis of the two static mixers, I found that droplets disintegrate
more quickly in the foam-like porous structure. As both geometries have
the same porosity and hydraulic diameter, I conclude that the change in
the free cross section is also an important parameter. I observed that in
the geometry with large changes in the free cross section, the droplets
are smaller.

Zusammenfassung

Pharmazeutische Produkte werden vorwiegend in Rührkesselreaktoren hergestellt. Alternativ werden immer häufiger kontinuierliche Rohrreaktoren in Betracht gezogen. In diesen können Einbauten als statische Mischer und als Katalysatorträger verwendet werden. Darüber hinaus dienen diese in Zweiphasenströmungen der Dispergierung. In der vorliegenden Dissertation werden Wärme- und Stofftransportprozesse in geometrisch definierten porösen Strukturen untersucht.

Die Temperaturverteiling in einem Rohrreaktor mit poröser Struktur kann theoretisch mittels CFD berechnet werden. Oft ist jedoch die genaue Geometrie unbekannt. Des Weiteren ist es rechnerisch sehr aufwändig, alle Effekte ausreichend aufzulösen. Deshalb wird hier ein makroskopisches Reaktormodell angewendet. In makroskopischen Modellen wird das Fluid und die poröse Struktur als Kontinuum modelliert. Die Transportkoeffizienten in diesen makroskopischen Erhaltungsgleichungen werden experimentell bestimmt.

Mikroskopische Untersuchungen können das Verständnis von Transportvorgängen auf makroskopischer Skala verbessern. Deswegen wurden optische Messungen in einer porösen Struktur durchgeführt. Dazu wurde diese mit einem Rapid-Prototyping-Verfahren aus einem transparenten Material gefertigt. Für die Experimente wurden zwei Fluide gewählt, welche den gleichen Brechungsindex haben wie die poröse Struktur: Anisol und eine wässrige Lösung von Natriumiodid und Zinkiodid. Da Anisol die poröse Struktur auflöst, wurde diese mit einer Lackschicht überzogen um die Lebensdauer zu verlängern. Die Salzlösung eignet sich für Experimente besser, da dieses Problem nicht auftritt. Die Kombination der zwei Fluide und der transparen Struktur ermöglicht optische Messungen in Ein- und Zweiphasenströmungen durch poröse Strukturen.

Mittels Particle Image Velocimetry wurde eine Einphasenströmung durch die poröse Struktur untersucht. Es wurde beobachtet, dass ab einer hydraulischen Reynolds-Zahl von $Re_h > 300$ die Geschwindigkeitsfluk-

tuationen isotrop sind. Für die Versuche wurden die zwei Fluide und zwei poröse Strukturen unterschiedlicher Dimension verwendet. Die Übereinstimmung dieser Experimente war zufriedenstellend, auch für Grössen welche nur schwer mit Particle Image Velocimetry messbar sind, wie zum Beispiel die Dissipationsrate der turbulenten kinetischen Energie. Mit dem $k - \varepsilon$ Modell wurde schliesslich die turbulente Diffusivität aus den Geschwindigkeitsdaten berechnet. Ein Vergleich mit dem makroskopischen Experiment lässt den Schluss zu, dass im Reynoldszahlbereich zwischen 150 und 450 die axiale Dispersion hauptsächlich durch Unterschiede in der mittleren Strömungsgeschwindigkeit hervorgerufen wird. Der turbulente Massentransport spielt verglichen dazu nur eine untergeordnete Rolle.

Schliesslich wurde eine Zweiphasenströmung durch die poröse Struktur und durch einen Sulzer SMX$^{\text{TM}}$ Mischer untersucht. Mittels laserinduzierter Fluoreszenz wurde die Grösse und die Position von Tropfen innerhalb dieser Strukturen bestimmt. Bei tiefen Geschwindigkeiten folgten die Tropfen bevorzugten Pfaden, während bei höherer Geschwindigkeit eine homogene Tropfenverteilung beobachtet wurde. Es stellte sich heraus dass die Grösse der Tropfen gut durch den Sauterdurchmesser repräsentiert wird. Bei der Durchströmung der zwei statischen Mischer nimmt dieser kontinuierlich ab, wobei in der Schaumstruktur kleinere Tropfen beobachtet werden. Da beide Mischer die gleiche Porosität und den gleichen hydraulischen Durchmesser aufweisen, schlussfolgere ich, dass auch die freie Querschnittsfläche ein wichtiger Parameter ist. Im Mischer mit stark variierender freier Querschnittsfläche wurden kleinere Tropfen beobachtet.

Acknowledgements

Contents

Nomenclature

Roman letters

a_s	Solid distribution function [-]
A	Cross-sectional area of empty tube [m^2]
A_{sf}	Interface area between solid and fluid [m^2]
c_p	Heat capacity [$J\,kg^{-1}\,K^{-1}$]
c	Tracer concentration [$kg\,m^{-3}$]
C_μ	Constant of $k - \varepsilon$ model [-]
D	Empty pipe diameter [m]
D_m	Molecular diffusion coefficient [$m^2\,s^{-1}$]
D_L	Mass dispersion coefficient in longitudinal direction [$m^2\,s^{-1}$]
D_T	Mass dispersion coefficient in transverse direction [$m^2\,s^{-1}$]
$D_\parallel$	Longitudinal total thermal diffusivity [$m^2\,s^{-1}$]
$D_\parallel^d$	Longitudinal thermal dispersion [$m^2\,s^{-1}$]
$D_\perp$	Transverse total thermal diffusivity [$m^2\,s^{-1}$]
$D_\perp^d$	Transverse thermal dispersion [$m^2\,s^{-1}$]
d	Droplet diameter of an individual droplet [m]
d	Characteristic diameter [m]
d_e	Diameter of equivalent channel [m]
d_{32}	Sauter mean droplet diameter [m]
d_{10}	Largest diameter representing 10 % of volume [m]
d_{90}	Largest diameter representing 90 % of volume [m]
d_{max}	Largest droplet diameter [m]

d_h	Hydraulic diameter of a porous structure [m]
E	Residence time distribution [s^{-1}]
f_h	Friction factor [m/s]
ΔH_R	Reaction enthalpy
k	Turbulent kinetic energy [m^2 s^{-2}]
k_{eff}	Effective thermal conductivity [W m^{-1} K^{-1}]
l	Length scale related to the porous structure [m]
l_1,l_2,l_3,l_4	Dimensions of Sulzer SMX$^{\text{TM}}$ [m]
l_K	Kolmogorov length scale [m]
L	Length of a measurement section [m]
L_{macro}	Length scale for macroscopic averaging [m]
L_{pore}	Length scale of single pore [m]
L_{system}	Length scale of system [m]
n	Refractive index [-]
n_1	Refractive index of optically thinner medium [-]
n_2	Refractive index of optically thicker medium [-]
n_i	Component of surface normal vector in i direction [-]
$\dot{n}$	Reaction rate [kg m^{-3} s^{-1}]
P	Pressure [N m^{-2}]
Pe_m	Peclet number defined with D_m [-]
Pr_T	Turbulent Prandtl number [-]
Re	Reynolds number [-]
Re_{part}	Particle Reynolds number [-]
Re_h	Reynolds number based on hydraulic diameter [-]
Sc	Schmidt number [-]
t	Time [s]
T	Temperature [°C]
u	Velocity [m s^{-1}]
$\overline{u}$	Mean velocity [m s^{-1}]

u'	Velocity fluctuation $[\mathrm{m\,s^{-1}}]$
u_D	Superficial (Darcy) velocity $[\mathrm{m\,s^{-1}}]$
u_e	Actual velocity in the pore channels $[\mathrm{m\,s^{-1}}]$
u_i	Velocity in i direction $[\mathrm{m\,s^{-1}}]$
u_I	Interstitial velocity $[\mathrm{m\,s^{-1}}]$
u_1	Velocity in axial direction $[\mathrm{m\,s^{-1}}]$
u_2	Velocity in x_2 direction $[\mathrm{m\,s^{-1}}]$
u_3	Velocity in x_3 direction $[\mathrm{m\,s^{-1}}]$
u_p	Pore velocity (respecting tortuosity) $[\mathrm{m\,s^{-1}}]$
v_*	Friction velocity $[\mathrm{m\,s^{-1}}]$
V	Volume of representative elementary volume $[\mathrm{m^3}]$
V_f	Volume of fluid $[\mathrm{m^3}]$
V_s	Volume of solid $[\mathrm{m^3}]$
$\dot{V}$	Volumetric flowrate $[\mathrm{m^3\,s^{-1}}]$
We_h	Weber number based on hydraulic diameter [-]
x_i	i coordinate [-]
x_1	Axial coordinate [-]
x_2	In-plane radial coordinate [-]
x_3	Out-of-plane radial coordinate [-]

Greek letters

α	Linear coefficient of pressure drop correlation
β	Quadratic coefficient of pressure drop correlation
Δ	Resolution of PIV measurement [m]
ε	Dissipation rate of turbulent kinetic energy [$\mathrm{m^2\,s^{-3}}$]
$\dot{\varepsilon}$	Volumetric transport fraction [-]
Γ_T	Turbulent diffusivity [$\mathrm{m^2\,s^{-1}}$]
λ_s	Thermal conductivity of solid [$\mathrm{W\,m^{-1}\,K^{-1}}$]
ψ	Generic field quantity
ϕ	Porosity [-]
ρ	Density [$\mathrm{kg\,m^{-3}}$]
ν	Kinematic viscosity [$\mathrm{m^2\,s^{-1}}$]
ν_T	Turbulent viscosity [$\mathrm{m^2\,s^{-1}}$]
σ	Interface tension [$\mathrm{N\,m^{-1}}$]
τ	Mean residence time [s]
τ	Tortuosity [-]
τ_{exp}	Expected mean residence time [s]
θ_1,θ_2	Angle of incidence and refraction

Abbreviations

a.u.	Arbitrary units
b/w	Black / White
CCD	Charge-coupled device
CoV	Coefficient of variation [-]
FFKM	Perfluoroelastomer
HSV	hue, value, saturation
LIF	Laser induced fluorescence
NBR	Nitrile butadiene rubber
Nd-YAG	Neodymium-doped yttrium aluminium garnet
PIV	Particle image velocimetry
PMMA	Polymethyl methacrylate
PTV	Particle tracking velocimetry
ppi	Pores per linear inch [-]
RGB	red, green, blue
RTD	Residence time distribution
RI	Refractive index
SLS	Selective laser sintering
TLC	Thermochromic liquid crystal
w/w	Weight fraction

Sub- and superscripts

a	Anisole (disperse phase)
b	Brine (continuous phase)
$crit$	At onset of velocity fluctuations
f	Fluid phase
in	Inlet
k	Generic species
m	Experiment with model dimensions
mix	Mixture phase
o	Experiment with original dimensions
out	Outlet
rms	Root mean square
s	Solid phase
sf	Solid-Fluid interface

Chapter 1

Introduction

1.1 Continuous reaction technology

An extensive review of reactions that are frequently encountered in the pharmaceutical and fine-chemicals industry is given by Mills and Chaudhari (1997). Traditionally these reactions are conducted in batch vessels, which are used as multi-purpose plants. However, there are many alternative reactors available (Stitt, 2002). Among them are monolithic structures, spinning disc reactors and tubular reactors (e.g. Stankiewicz and Moulijn, 2004). These reactors can be operated in batch or continuous mode. The continuous operation mode allows heat integration and therefore reduces the energy consumption. For this reason, continuous processes are believed to play a key role in the transition of the industry to a sustainable production. Further, the alternative reactors are usually able to cope with much higher reactant concentrations due to their superior heat- and masstransfer capacities. The overall size of the reactor is therefore smaller, leading to an improved safety.

For reactions in the pharmaceutical and fine-chemicals industry, many continuous reactors are commercially available. Figure 1.1 shows continuous reactors provided by Ehrfeld Mikrotechnik AG. These reactors are used for lab purposes as well as for pilot and production plants and can basically be characterized as tubular reactors. A critical issue for tubular reactors is the scale-up, which can be achieved by changing the size and the length of a channel. Typically, continuous tubular reactors have a size which is small enough such that surface forces play an important role. When the channel diameter is changed, the flow regime can change. This can lead to drastic changes in the operation of a reactor. But also
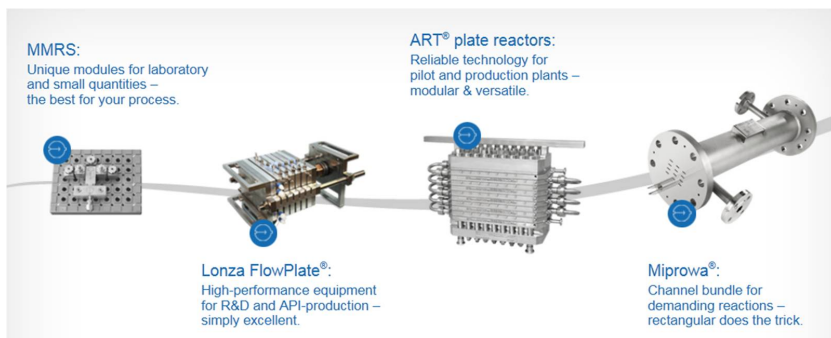
Figure 1.1: Commercially available continuous reactors from Ehrfeld Mikrotechnik BTS.

in single-phase flow the heat and mass transfer is drastically affected by changes in flow regime. The allowed scale-up factor for the channel size is therefore rather limited. Kockmann et al. (2009) proposed a scale-up factor for the cross-section area of 4 to 6. The scale-up problem can be avoided by simply building many small reactors in parallel (external numbering-up). A channel bundle reactor follows this principle without rebuilding all equipment in parallel, i.e. the cooling system is built only once for all reactors in parallel (internal numbering-up). This reactor has to be designed such, that the flow is homogeneously distributed over all channels. Flow maldistribution can lead to overheating, inhomogeneous mixing and departure from stoichiometry. Therefore the transfer from lab to production scale usually comprises a scale-up as far as possible, eventually combined with numbering up (Kockmann et al., 2009).

The decision for a certain reactor type also depends on the reaction. Roberge et al. (2005) found that from 86 reactions frequently carried out by Lonza, 50 % would benefit from a continuous process. They classified the potential reactions for continuous processes according to three types. Type A reactions are very fast ($< 1\,\mathrm{s}$) and mainly controlled by mixing. The yield of such reactions can be increased by rapid mixing and enhanced heat transfer in tubular reactors. Type B reactions are rapid ($10\,\mathrm{s}$-$10\,\mathrm{min}$) but predominantly controlled by the kinetics of the reac-

tion. The yield of these reactions can be increased by a precise control of residence time and temperature. Type C reactions are slow ($> 10\,\mathrm{min}$) but a thermal hazard is possible. Using a continuous reactor allows to intensify the reaction, reducing the volume and therefore improving safety. However, Roberge et al. (2005) claim that a large part of the reactions can at the moment not be done in microreactors due to the presence of a solid (either as reactant, catalyst or product). Therefore, continuous reactors in the fine-chemical and pharmaceutical industry are today predominantly used for homogeneous single-phase reactions or gas-liquid and liquid-liquid reactions.

1.2 Heterogeneous catalysis and porous structures

For continuous heterogeneous reactions there are two options for the catalyst. One possibility is that catalyst particles stream with the reactants through the reactor and are separated after the reactor. Alternatively, the catalyst can be immobilized within the reactor. This can be achieved by a packed bed of catalyst particles or by impregnating a porous structure (Bonrath, 2013).

Catalytic reactors with immobilized catalyst can be divided into random and structured reactors. A suitable reactor system can be found by defining the requirements of the reaction. Stankiewicz and Moulijn (2004) name the major basic concerns for catalytic reactors:

- Catalyst quality on microscopic scale (number of active sites)
- Catalyst quality on mesoscopic scale (diffusion length, loading)
- Ease of catalyst separation and handling
- Heat supply and removal
- Hydrodynamics (regimes, controllability, predictability)
- Transport resistance (rate and selectivity)
- Safety and environmental aspects (runaway, hazardous materials, selectivity)
- Costs

The random packed bed reactor is very strong in terms of catalyst loading
and costs. However, structured catalysts can be favourable in terms of
heat and mass transfer and hydrodynamics. For example, monoliths are
the dominant three-way catalysts in cars. The straight channels prevent
the accumulation of dust and provide a low pressure drop. However,
the channels are not connected and therefore no exchange of fluid in
radial direction is possible. This can lead to locally higher temperatures
when a pore is blocked. Compared to monoliths, a foam-like porous
structure has better radial heat- and mass transfer. On the other hand
the tortuosity of the flow comes along with a higher pressure drop. There
are other structured reactors such as gauzes, arrays of corrugated plates
and arrays of fibers. Depending on the requirements of the reaction, any
of these reactor types can be favourable.

Hutter (2010) proposed a chemical reactor with a foam-like porous
structure. Metallic foams are used for wide-ranging applications such as
in heat exchange, as silencers, flame arresters, and as catalyst support
(Banhart, 2001). Amongst others, manufacturing techniques for foam
structures include foaming of liquid metals, casting, and sintering. Hut-
ter (2010) proposed to use rapid prototyping to manufacture a foam-like
porous structure for the use as catalyst support. This allows to produce
foam structures of defined geometries, improving the reproducibility of
experiments. Further, the knowledge of the exact geometry of the porous
structure facilitates CFD simulations. Unlike in flow through unregular
foam structures, periodic boundary conditions can be applied for sim-
ulations as the structures are periodic in streamwise direction (Hutter
et al., 2011b). A further advantage of selective laser sintering is that
the foam structure can be physically connected to the tube. Compared
to a foam structure which is not physically connected to the wall, this
improves the heat transfer to the wall by 30 % (Hutter et al., 2011c).

A major concern for continuous reactors with porous structures for
the use in industry is the scale-up. Figure 1.2 shows three options for
transferring porous structure reactors from lab scale to production scale.
The most reliable scale-up procedure is to simply build identical reac-
tors in parallel. This scale-up procedure is frequently called numbering
up. One of the challenges in this procedure is to equally distribute the
reactants and cooling to the large number of reactors. Depending on
the scale-up factor the high number of reactors can make this solution
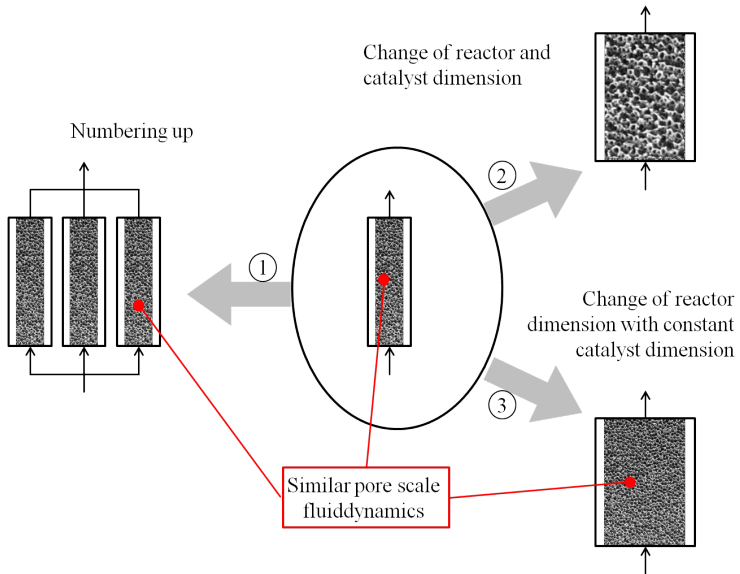
Figure 1.2: Variants for scale-up of porous structure reactors: numbering up ①, simultaneous change of reactor and catalyst dimension ②, increased reactor dimension with unchanged catalyst dimension ③.

uneconomic. Another option for the scale-up is to change the dimension of the reactor. In principle, two options exist. Either the dimension of the pore size remains unchanged or it is scaled too. When scaling the size of the pores, the fluiddynamics changes. Further, the catalyst quality in a structure of larger dimension could be different. Therefore, changing the reactor dimension while keeping the pore dimension is seen as a promising scale-up approach. The concept of parallelizing the functional element, i.e. the porous structure, and group it as a stack in a new housing is frequently called *internal numbering-up* (Schenk et al., 2004). What has to be considered is the change in temperature distribution within the reactor. A homogeneous temperature distribution promotes a high selectivity of the reaction. Therefore, one aim of this thesis is to model the temperature distribution in a tubular reactor with a porous structure. In contrast to Hutter et al. (2011c), who investigated heat transfer from a porous structure to a wall, this thesis investigates heat transfer within a porous structure.

Further objectives of this thesis are the investigation of mass transfer processes in a porous structure reactor. Using appropriate experimental techniques, transport processes should further be investigated on the pore scale of a porous structure. As many reactions involve more than one phase, transport processes should further be investigated in two-phase flow through porous structures. In the following, an introduction to fluiddynamics in porous structures is given.

1.3 Fluiddynamics in porous structures

1.3.1 Reynolds number

Different definitions of the characteristic diameter and the velocity in flow through a porous structure exist. In this thesis, the Reynolds number is defined with the hydraulic diameter and the interstitial velocity:

$$Re_h = \frac{u_I \cdot d_h}{\nu}. \tag{1.1}$$

The hydraulic diameter is defined with the volume of fluid (V_f) and the interface area between solid and fluid (A_{sf}) according to Carman (1937):

$$d_h = \frac{4V_f}{A_{sf}} \tag{1.2}$$

The interstitial velocity u_I was calculated from the Darcy velocity and the porosity of the bed as follows:

$$u_I = \frac{u_D}{\phi} \tag{1.3}$$

Note that Carman (1937) called it *diameter of equivalent channel d_e* and *actual velocity in the pore-channels u_e*. Later, Comiti and Renaud (1989) proposed a model of a porous structure with the same definition of the characteristic diameter. They modeled a packed bed as a bundle of tortuous pores of diameter:

$$d = \frac{4\phi}{\frac{A_{sf}}{V_s}(1-\phi)} \tag{1.4}$$

The mean velocity in the pore was calculated by respecting the tortuosity τ of a pore:

$$u_p = \frac{u_D\tau}{\phi} \tag{1.5}$$

The diameters defined by Eq. (1.2) and Eq. (1.4) are the same, as can be seen by replacing ϕ with $V_f/(V_s + V_f)$. In flow through porous media the diameter is frequently referred to as pore diameter according to Comiti and Renaud (1989). In flow through static mixers it is frequently referred to as hydraulic diameter, sometimes without specifying a reference, potentially because it was assumed to be general knowledge (e.g. Streiff et al., 1999). In my opinion, the term *pore diameter* is less precise. Depending on the area of research, the scientific communities have different ideas about what is a pore. In biology, a pore typically describes an opening in a membrane. In earth sciences, a pore is one of many small openings in a solid substance of any kind that contribute to the substance's porosity. In particular, a pore can be of spherical or tubular shape. Calculating the pore diameter according to Eq. (1.4) can therefore lead to a diameter that is different from the diameter of the

spherical and tubular pores that constitute a porous medium. The term *pore diameter* therefore has to be used with caution.

Other definitions of the characteristic diameter were also discussed. Suitable definitions of the characteristic diameter could be the cell diameter (Dukhan and Suleiman, 2014), ligament diameter (Zenklusen et al., 2014), particle diameter (e.g. Jolls and Hanratty, 1966), pore diameter[1] (Häfeli et al., 2013) or the diameter of particles with the same surface area per solid volume (Horneber et al., 2012). The choice of the characteristic diameter strongly influences the Reynolds number. In the foam-like porous structure that will be used in this thesis, the cell diameter is 2.8 times larger than the pore diameter. Therefore, choosing the cell diameter as the characteristic length leads to Reynolds numbers that are 2.8 times higher than if the pore diameter were chosen instead. This explains why it is generally difficult to compare studies by different authors. So, what should be chosen as the characteristic diameter? The answer depends on the dominant physics. Some porous structures are built up as a network of cylinders. In such a case, the results are frequently compared to studies on flow around single cylinders (Zenklusen et al., 2014). In that case it can be appropriate to use the cylinder diameter as the characteristic diameter. In studies of flow through packed beds of spheres, it can be more convenient to take the sphere diameter as the characteristic length scale. However, if the goal is to compare flow through porous structures of arbitrary geometry, the characteristic length can be defined based on the hydraulic diameter (Eq. 1.2).

1.3.2 Inertial flow regime

When the velocity of a Newtonian fluid streaming through a porous structure is low enough, laminar flow can be observed. The laminar flow regime can be sub-divided into the Darcy regime and the inertial flow regime. The distinction between the regimes is based on the pressure drop. At low flowrates, the pressure drop ΔP per length L is proportional to the fluid velocity u_I:

$$\frac{\Delta P}{L} = \alpha \, u_I \tag{1.6}$$

---

[1]that could have been called window diameter in order to avoid confusion with the diameter defined by Eq. (1.4).
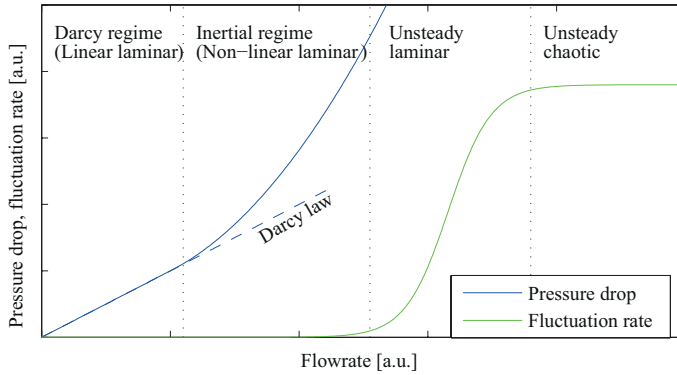
Figure 1.3: Flow regimes in porous structures. In the inertial flow regime, the pressure drop is not proportional to the flowrate, but the flow is steady.

This regime is referred to as Darcy regime. At higher velocities, the relation between pressure drop and flowrate is nonlinear. In that case the pressure drop can be described as:

$$\frac{\Delta P}{L} = \alpha\, u_I + \beta\, u_I^2 \tag{1.7}$$

This regime is referred to as inertial regime. Figure 1.3 shows the inertial flow regime between the Darcy regime and the onset of fluctuation. The physical origin of the deviation from Darcy's law is still disputed and many effects are discussed. However, what is known is that it is not associated with velocity fluctuations (Hlushkou and Tallarek, 2006). The inertial regime starts at very low Reynolds numbers, i.e. $Re \approx 1$. Of course, this depends on the definition of the Reynolds number and on the geometry of the porous structure. But certainly, the inertial regime starts at flowrates one order of magnitude lower than the onset of velocity fluctuations (Hlushkou and Tallarek, 2006). One explanation for the non-linearity of the pressure drop is that it is caused by loss of kinetic energy when the fluid changes direction or when it is accelerated and

decelerated. Another explanation is the formation of a boundary layer with an inertial core.

At very low Reynolds numbers Darcy's law is not valid. This regime is frequently called pre-Darcy regime and it can be observed at very low velocities (Bağci et al., 2014). There, other effects play a role such as non-Newtonian viscosity. In practical applications, this flow regime is however rarely encountered.

1.3.3 Laminar - turbulent transition

The transition from laminar to turbulent can be classified into four flow regimes (without the pre-Darcy regime). Dybbs and Edwards (1984) identified their limits in flow through packed beds of spheres and rods. The Reynolds number was defined based on the particle or rod diameter constituting the bed:

1. Darcy flow regime: at very low Reynolds numbers ($Re < 1$) the flow is laminar and dominated by viscous forces. In this regime the pressure drop is linearly proportional to the flowrate.

2. Inertial flow regime: at higher Reynolds numbers (between 1 and 10) inertial forces start to play a role and the relation between pressure drop and flow rate is no longer linear. The flow is however still steady.

3. Unsteady laminar flow regime: at a Reynolds number between ≈ 150 and ≈ 300 fluctuations are observed starting with laminar wake oscillations with preferred frequencies.

4. Unsteady and chaotic regime: a highly unsteady and chaotic flow regime starts at $Re \approx 300$.

The exact Reynolds numbers defining the limits between the flow regimes vary depending on the geometry under investigation. In the following, the most important literature on onset of velocity fluctuations and transition to turbulence is discussed. I will start with studies in packed beds of spheres and then discuss porous structures of other geometry.

Transition in packed beds of spheres

Jolls and Hanratty (1966) investigated the transition to turbulence for flow through a bed of spherical particles. They measured the instantaneous local mass transfer rate using an electrochemical technique. At very low particle Reynolds numbers (based on empty column velocity and sphere diameter) the electrode signal and therefore the mass transfer rate was constant. The onset of unsteady flow was observed as gentle waving of the electrode signal at particle Reynolds numbers between $Re_{part} = 110$ and $Re_{part} = 150$. The slow and periodic variation of mass transfer was associated to an unsteady laminar flow regime. The electrode measurements were further validated with an optical measurement technique. For this, a red dye was injected within the porous structure and its movement through the bed observed by a camera. The transition from a steady to an unsteady laminar regime was observed at the same particle Reynolds number as with the electrode measurements. At particle Reynolds numbers near 300 the flow was found to be turbulent.

Onset of velocity fluctuations in flow through packed beds of spheres was later investigated by several other authors (Wegner et al., 1971; Latifi et al., 1989; Seguin et al., 1998a,b). They all found that the onset of fluctuations occurs at particle Reynolds numbers between $Re_{part} = 90$ and $Re_{part} = 150$.

Flow regimes in structured packings of spheres were investigated by Bu et al. (2015). They observed that the laminar and the turbulent regimes are characterized by a defined level of the fluctuating rate of the signal of an electrode on the packing. This allowed to identify the limits between laminar, transitional and turbulent regimes. Three different arrangements were tested: standard cubic (SC), body centered cubic (BCC) and face centered cubic (FCC). The transition regime was observed at $260 < Re_{part} < 430$ (SC), $130 < Re_{part} < 350$ (BCC), and $70 < Re_{part} < 250$ (FCC). This shows that, already in packed beds of spheres, the result is strongly depending on the exact configuration.

Transition in other porous structures

Seguin et al. (1998a) investigated flow through packed beds of spheres,

packed beds of square-based parallelepipedal plates, and reticulated media (synthetic foams). The final objective was to propose a dimensionless criterion, for which a single value would characterize the onset of velocity fluctuations. They used the particle Reynolds number as above. Further they defined a pore Reynolds number using the hydraulic diameter and the pore velocity (interstitial velocity multiplied with tortuosity) and an interstitial Reynolds number (interstitial velocity and particle diameter). The pore Reynolds number was identified as the best suitable dimensionless number. For all packed beds of particles, apart from beds of flat plates in parallel configuration, the onset of velocity fluctuations was observed at pore Reynolds numbers ≈ 180. However, the study of synthetic foams showed that the stable laminar regime is maintained up to higher pore Reynolds numbers (> 400). It was therefore not possible to define a single dimensionless number which describes the onset of velocity fluctuations in arbitrary geometries.

The flow regimes in a Sulzer SMX$^{\text{TM}}$ where experimentally investigated by Hirech et al. (2003). The static mixer was considered as a porous medium and the pore Reynolds number was defined using the hydraulic diameter and the pore velocity (interstitial velocity multiplied with tortuosity). Onset of fluctuations was observed at pore Reynolds numbers of 200. Turbulent flow was observed at a pore Reynolds number between 1500 and 3000.

This overview shows that the Reynolds number, however defined, can not be used to uniquely define flow transition in porous structures of arbitrary geometry. Onset of velocity fluctuations can occur at Reynolds numbers as low as $Re_{part} = 70$, as observed by Bu et al. (2015) in face-centered cubic packed beds of spheres.

1.4 Macroscopic vs microscopic modeling

A detailed model of a porous structure reactor can be of arbitrary complexity. However, in many cases one is not interested in the details of fluiddynamics on the microscopic scale. For modeling of a chemical reactor, a macroscopic model for heat-, mass-, and momentum conservation can be more appropriate. The condition for macroscopic modeling to be applicable is that the size of a representative elementary volume has a
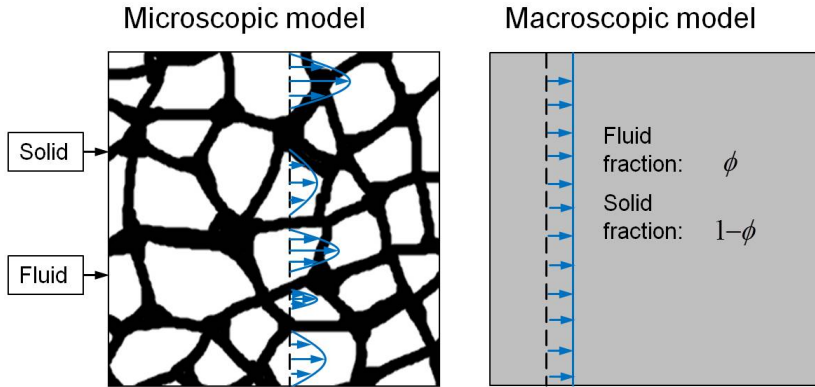
Figure 1.4: The microscopic model (left) distinguishes between solid and fluid domains. Macroscopic models (right) assume both phases as homogenous.

certain minimum size such that it leads to statistically meaningfull local average properties. When the volume is large enough, the addition of extra volume to a representative elementary volume does not change the average properties. In other words, the following relation should hold:

$$L_{system} \gg L_{macro} \gg L_{pore} \tag{1.8}$$

where L_{pore} is the characteristic length scale of a pore, L_{macro} is the length of a control volume of the macroscopic model and L_{system} is the system scale. In the macroscopic model, all quantities are continuous. Figure 1.4 visualizes the difference between microscopic and macroscopic modeling. Whereas the microscopic model distinguishes between solid and fluid domains, the macroscopic model assumes a porous structure as a continuum with a solid and a fluid fraction.

The main challenge for the derivation of macroscopic conservation equations is to avoid unwarranted simplifications. However, empiricism can not be avoided completely. Two approaches are most common for the derivation of macroscopic conservation equations: averaging methods and mixture theories of continuum mechanics (Gray and Hassanizadeh,

1998). In averaging methods, the conservation equations are written on the microscopic scale and subsequently averaged. Assumptions then have to be made about the temporal/spatial distribution of the phases. In the mixture theory approach, the development of the model starts directly on the macroscopic scale in analogy to single-phase bodies. Additional terms are then introduced to account for exchange of mass, energy and momentum among phases. Here, the macroscopic averaging method is discussed. Kaviany (1991) shows the volume averaging rules for macroscopic modeling in detail. The most important steps are summarized summarized in the following. A solid distribution function is defined as

$$a_s(x) = \begin{cases} 0 & \text{if } x \text{ is in the void region,} \\ 1 & \text{if } x \text{ is in the solid region.} \end{cases} \tag{1.9}$$

The local porosity in a representative elementary volume V can be calculated as

$$\phi(x) = \frac{1}{V} \int_V (1 - a_s(x)) dV \tag{1.10}$$

A similar averaging rule holds for any other quantity ψ (tensor of any order)

$$\langle \psi \rangle = \frac{1}{V} \int_V \psi dV \tag{1.11}$$

For the macroscopic averaging of a quantity associated to the fluid phase, the operator $\langle . \rangle^f$ is defined:

$$\langle \psi \rangle^f = \frac{1}{V_f} \int_{V_f} \psi dV \tag{1.12}$$

Wheter Eq. (1.11) or Eq. (1.12) is more suitable depends on the quantity that should be averaged.

For the volume averaging of the continuity equation, energy conservation equation and Navier-Stokes equation, the average of a gradient (or divergence) has to be replaced by the gradient (or divergence) of an average. Kaviany (1991, p. 56ff) shows the derivation of the theorems required. For single-phase flow through a porous structure, the continuity equation written in Einstein notation reads as:

$$\frac{\partial \rho}{\partial t} + \frac{\partial}{\partial x_i} \rho \, u_i = 0 \tag{1.13}$$

Volume averaging leads to (Kaviany, 1991, p. 58)

$$\frac{\partial \langle \rho \rangle}{\partial t} + \frac{\partial}{\partial x_i} \langle \rho\, u_i \rangle + \frac{1}{V} \int_{A_{sf}} \rho\, u_i\, n_i\, dA \overset{0}{=} 0 \qquad (1.14)$$

The integral of velocity over the solid-fluid phase boundary A_{sf} is zero, as the velocity normal to the surface is zero.

1.4.1 Momentum conservation

Similarly, the momentum equation can mathematically rigorously be transformed to a volume averaged version. However, the integral over the phase boundary A_{sf} does not vanish, as there is momentum transport over the phase boundary. This term has to be modeled, what requires experimental verification. Therefore, the volume averaged momentum equation is empiric to some extent. One possibility to estimate the interphase momentum transport is by dimensional analysis. In that case the volume averaged momentum equation can be written as (Kaviany, 1991, Eq. (2.97)):

$$\rho_0 \left[\frac{\partial \langle u_i \rangle}{\partial t} + \langle u_j \frac{\partial u_i}{\partial x_j} \rangle \right] = -\frac{\partial}{\partial x_i} \langle P \rangle + \mu \frac{\partial^2 \langle u_j \rangle}{\partial x_i \partial x_j} - \frac{\phi \mu}{d^2 k_s} \langle u_i \rangle \qquad (1.15)$$

where d is a characteristic length and k_s is a dimensionless parameter that has to be estimated empirically. This is not very satisfactory. First, the equation is quite complex and second, it contains empiric parameters. Therefore, other empiric models which are less complex are required. For example, in many cases it can be sufficient to model the fluid velocity as one dimensional. This is especially the case in flow through tubular reactors with porous structures. Therefore, the macroscopic velocity field is simplified as follows:

$$\langle u_1 \rangle = f(\Delta p / L, geometry, d_h, ...) \qquad (1.16)$$
$$\langle u_2 \rangle = \langle u_3 \rangle = 0 \qquad (1.17)$$

The macroscopic velocity can be defined according to Eq. (1.11), resulting in the Darcy velocity:

$$u_D = \langle u_1 \rangle = \frac{\dot{V}}{A} \qquad (1.18)$$

Alternatively, the macroscopic velocity can be defined according to Eq. (1.12), resulting in the interstitial velocity:

$$u_I = \langle u_1 \rangle^f = \frac{\dot{V}}{A\,\phi} \qquad (1.19)$$

1.4.2 Conservation of scalars

Mass conservation

On the microscopic scale, overall mass conservation in the fluid is described by:

$$\frac{\partial \rho}{\partial t} + \frac{\partial \rho\,u_i}{\partial x_i} = 0 \qquad (1.20)$$

When multiple species are present, there will additionally be transport by diffusion. On the microscopic scale, the conservation equation for a species k is given as (Kaviany, 1991, Eq. (6.54)):

$$\frac{\partial \rho_k}{\partial t} + \frac{\partial \rho_k\,u_i}{\partial x_i} = \frac{\partial}{\partial x_i}\left(D_{mk}\rho\frac{\partial}{\partial x_i}\frac{\rho_k}{\rho} \right) + \dot{n}_k \qquad (1.21)$$

where $\dot{n}_k$ is the rate of production of species k by reactions in the fluid. This conservation equation should be transformed to a macroscopic conservation equation. When thermodynamical equilibrium between all phases is assumed, a single conservation equation for the concentration in the fluid is sufficient. The concentration of species in all other phases can then be calculated by an algebraic equation from the concentration in the fluid. The macroscopic conservation equation can be obtained from Eq. (1.21) by volume averaging (Kaviany, 1991, Eq. (6.63)):

$$\begin{aligned}
\frac{\partial \langle \rho_k \rangle^f}{\partial t} + u_I \frac{\partial \langle \rho_k \rangle^f}{\partial x_1} =& D_L \langle \rho \rangle^f \frac{\partial^2}{\partial x_1^2} \frac{\langle \rho_k \rangle^f}{\langle \rho \rangle^f} \\
& + D_T \langle \rho \rangle^f \frac{\partial^2}{\partial x_2^2} \frac{\langle \rho_k \rangle^f}{\langle \rho \rangle^f} + D_T \langle \rho \rangle^f \frac{\partial^2}{\partial x_3^2} \frac{\langle \rho_k \rangle^f}{\langle \rho \rangle^f} \\
& + \langle \dot{n}_k \rangle^f + \langle \dot{n}_k \rangle^{sf}
\end{aligned} \qquad (1.22)$$

Here it was assumed that the transport coefficients are constant. Like this they can be taken out of the derivative. In contrast to (Kaviany,

1991, Eq. (6.63)), the porous structure was assumed to be isotropic. When a porous structure is isotropic, the dispersion tensor becomes diagonal. The diagonal elements of the dispersion tensor are the coefficients D_L and D_T, the dispersion coefficients in longitudinal and transverse direction. The dispersion coefficients are parameters that include the transport of mass by molecular motion, fluid flow and turbulence. Kaviany (1991) further distinguished between effective diffusivity (contribution of molecular diffusion) and mass dispersion (contribution of fluid flow) and called the sum of them *total effective mass diffusivity*. In the present thesis, these transport coefficients are called *dispersion coefficients* in accordance to many publications (e.g. Delgado, 2006; Han et al., 1985) .

The accuracy of an empiric model relies on the validity of the assumptions made. For example, a process can be limited by mass transfer between the fluid and the solid phase. In that case, two conservation equations have to be used and interphase transport resistance has to be modeled. For further details, the reader is referred to Kaviany (1991). In the present thesis, thermodynamic equilibrium between the phases will be assumed.

Energy conservation

The macroscopic equations for the conservation of energy are very similar to the ones for mass. Again, it is assumed that the phases are in local equilibrium ($\langle T_s \rangle = \langle T_f \rangle$). Therefore, a single macroscopic conservation equation can be written (Kaviany, 1991, Eq. (4.221)):

$$
\begin{aligned}
\frac{(\rho\,c_p)_{mix}}{(\rho\,c_p)_f}\frac{\partial\langle T\rangle}{\partial t} + u_D\frac{\partial\langle T\rangle}{\partial x_1} =& D_{\parallel}\frac{\partial^2\langle T\rangle}{\partial x_1^2} \\
&+ D_{\perp}\frac{\partial^2\langle T\rangle}{\partial x_2^2} + D_{\perp}\frac{\partial^2\langle T\rangle}{\partial x_3^2} \\
&+ \frac{\phi\langle\dot{n}_k\rangle^f\Delta H_R}{(\rho\,c_p)_f} + \frac{\phi\langle\dot{n}_k\rangle^{sf}\Delta H_R}{(\rho\,c_p)_f}
\end{aligned} \qquad (1.23)
$$

where the heat capacity of the mixture is given as:

$$
(\rho\,c_p)_{mix} = \left[\phi\,(\rho\,c_p)_f + (1-\phi)\,(\rho\,c_p)_s\right] \qquad (1.24)
$$

Again, constant transport coefficients and an isotropic porous structure is assumed. When a porous structure is isotropic, the diffusivity tensor can be assumed diagonal. The diagonal elements of the thermal diffusivity tensor are the coefficients $D_\parallel$ and $D_\perp$. The *longitudinal total thermal diffusivity* summarizes heat transport by the solid (*effective thermal conductivity* k_{eff}) and by the fluid (*longitudinal thermal dispersion* $D_\parallel^d$):

$$D_\parallel = \left[\frac{k_{\text{eff}}}{(\rho \, c_p)_f} + \phi \, D_\parallel^d \right] \tag{1.25}$$

The *transverse total thermal diffusivity* summarizes heat transport by the solid (*effective thermal conductivity* k_{eff}) and by the fluid (*transverse thermal dispersion* $D_\perp^d$):

$$D_\perp = \left[\frac{k_{\text{eff}}}{(\rho \, c_p)_f} + \phi \, D_\perp^d \right] \tag{1.26}$$

Thermal equilibrium between the phases is not fulfilled in every case. Exceptions are cases where a significant amount of heat is generated in one of the two phases. Also, when temperature or flowrate changes with respect to time and the two phases have significantly different heat capacities and thermal conductivities, local thermal equilibrium does not apply. In that case, two conservation equations for the fluid and the solid phase have to be used. This additionally requires modeling of heat transfer between the phases. For further details, the reader is referred to Kaviany (1991). In the present thesis, thermal equilibrium between the phases will be assumed.

Chapter 2

Investigated porous structures

In the course of this thesis, porous structures of different geometry, size and material were investigated. Figure 2.1 gives an overview. For the investigation of macroscopic heat transfer, an unstructured aluminum foam was used (a). For reaction studies (not part of this thesis) and for macroscopic mass transfer studies, a foam-like porous structure manufactured by selective laser sintering was used (b). A structure of the same geometry was manufactured by stereolithography (c). This enabled optical measurements in the porous structure. Finally, I investigated flow through a Sulzer SMX^{TM} static mixer (d). In the following, the characteristics of the porous structures and their manufacturing techniques are described.

2.1 Unstructured aluminum foam

In Chapter 3, an experimental technique for the determination of transport coefficients of heat will be shown. For this, a setup was built in which a two-dimensional temperature profile is observed. Therefore, the porous structure had to have a certain extent in two dimensions. In the final design of the setup, the foam had a size of $280 \times 200 \times 15$ mm. An unstructured foam from ERG Aerospace Corporation was used. The foam is sold under the brand name Duocel^{TM} and is available with different pore sizes and porosities. For the experiments shown in this thesis, a foam with 40ppi (pores per inch) was used. The value for the pore density is the manufacturer's designation. It is not necessarily an indication of true pore size. Perrot et al. (2007) studied geometric characteristics of Duocel^{TM} foams and compared it to other literature data. They found
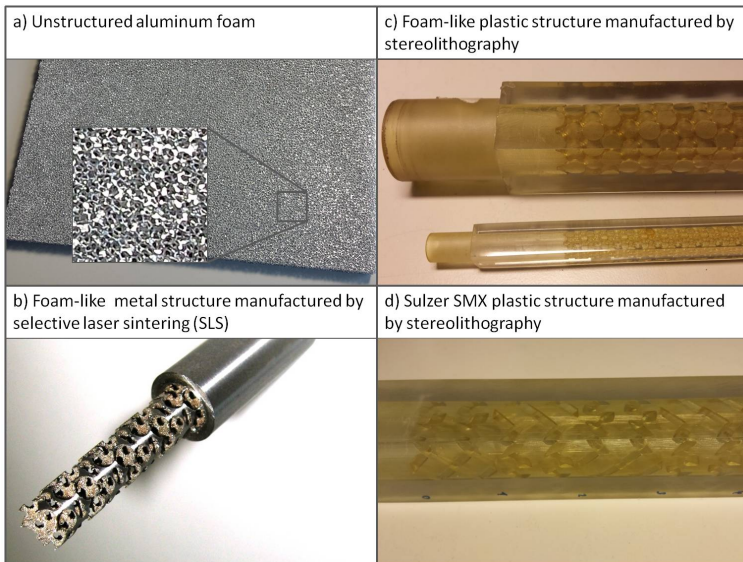
Figure 2.1: Overview of investigated structures.

that the thermal characteristic length scale of the foam is 1.85 mm (from reconstructed orthotropic unit cell). The hydraulic diameter as defined in this thesis (Eq. 1.2) corresponds to twice the thermal characteristic length of Perrot et al. (2007). I therefore estimated the hydraulic diameter of the 40ppi structure as 3.7 mm. The porosity of the foam was measured gravimetrically. It was found that the foam has a porosity of 88.6 %.

2.2 SLS and stereolithography

Rapid prototyping allows to reproducibly manufacture porous structures. In this thesis, two rapid prototyping techniques were used. The first is the so called selective laser sintering (SLS). In this manufacturing technique, a structure is built up layer by layer by sintering a powder. Laser sintering can be done with various kinds of materials like for example polyamide, stainless steel, and titanium. While the choice of material is of great importance if the porous structure is to be used as catalyst support, it is of minor importance for the study of inert systems. The requirement was therefore that it should be resistant to water with small amounts of salt. Further the manufactured structure was exposed to pressures up to 10 bar. Therefore, stainless steel was used. The parts were manufactured by Ecoparts AG (Rüti, Switzerland). The feedstock particles had a diameter of 20 µm and the layer thickness in the manufacturing process was 50 µm. The disadvantage of SLS is that it is not available for transparent materials. When optical access to the structure is required, a different manufacturing technique has to be used.

The second manufacturing technique is the so called stereolithography. In stereolithographic manufacturing, a photo-reactive resin is cured by a UV laser or a similar light source. Like this, a structure is built up layer by layer. There are various materials available. We used Somos$^{\circledR}$ WaterShed XC 11122, a transparent epoxy resin. The parts were ordered from von Allmen AG (Pfäffikon, Switzerland). The layer thickness in this manufacturing technique was 50 µm.

2.3 Geometries manufactured by rapid prototyping

The porous structure that is mainly used in this thesis is the one proposed by Hutter (2010). It is designed as the negative of tetrahedrally arranged overlapping spheres. Figure 2.2 shows one periodic unit of this porous structure inside a tube. The large void spaces inside the struc-
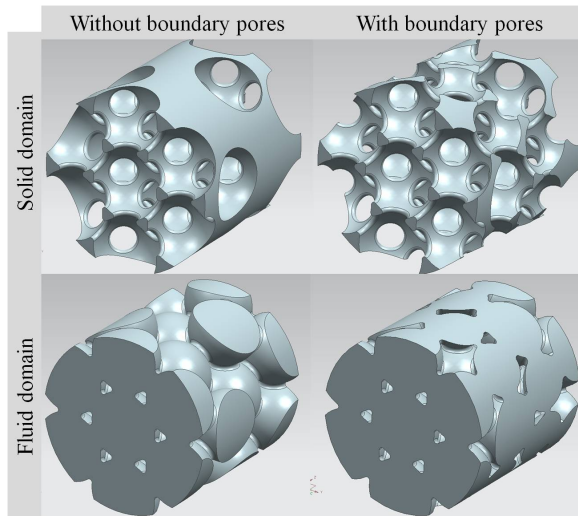
Figure 2.2: One periodic unit of the porous structure. Shown are the solid and the fluid domain for a design where small pores at the boundary are included and excluded.

ture are in the following referred to as *cells*. The openings between two adjacent cells will be called *pores*. A cell is generally connected to twelve other cells. The fluid mainly enters a cell through its three upstream neighbors and mainly leaves through the three downstream neighbors. The remaining six neighbors are found perpendicular to the main flow axis and therefore there is only minor flow to these cells. The cells at the boundary of the tube are only connected to few other cells. For example,

Table 2.1: Characteristic dimensions of the foam-like porous structures manufactured by stereolithography (SL) and selective laser sintering (SLS).

Manufacturing procedure	SL	SL	SLS
Material type	plastic	plastic	steel
Empty pipe diameter D [mm]	20	7	7
Length of periodic unit [mm]	19.25	6.74	6.74
Cell diameter [mm]	7.94	2.78	2.9
Cell distance [mm]	7.86	2.75	2.75
Rounding radius [mm]	0.34	0.12	0
Pore diameter [mm]	2.88	1.01	0.92
Porosity [%]	70.4	70.4	84.2
Bulk Porosity [%]	78.7	78.7	84.8
Hydraulic diameter [mm]	6.23	2.18	1.96
Bulk hydraulic diameter [mm]	7.86	2.75	2.73
Boundary pores included	no	no	yes

the smallest cells at the boundary are connected to only five other cells. Further, the volume of these cells is much smaller than cells in the center of the tube. Therefore, the fluiddynamics in boundary pores is expected to be different. In the optical measurements it was therefore decided to dismiss all cells which have their center outside of the tube (see Fig. 2.2).

The foam-like porous structure is made of metal by SLS and of plastic by stereolithography. The standard size was such, that they fit in a pipe of 7 mm diameter. The plastic structure was further upscaled to 20 mm to allow optical measurements with improved resolution. The geometric parameters of the structures are given in Table 2.1.

In the stereolithographic structure of 7 mm diameter, it was found that there is a significant deviation between the CAD model and the manufactured structure. Therefore the exact geometry was measured by X-ray tomography (Hutter et al., 2011b). These measurements allowed to determine the geometry with a resolution of 5 µm. The values

given in Table 2.1 for the small stereolithographic structure represent the dimensions fitted to the model from the X-ray scan. In the large stereolithographic structure the relative deviation of the designed dimension to the manufactured dimension is neglected. This is motivated by the high resolution of the manufacturing process in relation to the size of this structure. The SLS manufacturing is expected to have some uncertainty as well. Hutter (2010, Fig. 6.2) showed microscopic images of a porous structure manufactured by SLS. There it is observed that the sharp edges of the CAD model are not reproduced by SLS. A tomographic scan of the manufactured structure is however not available. Therefore the data given in Table 2.1 for the SLS structure resemble the values according to the CAD model.

Table 2.1 further distinguishes between bulk porosity and the porosity of the structure in the tube. The bulk porosity is the porosity that the porous structure would have in a medium of infinite extent. The porosity in the tube is the volume of void space divided by the volume of the empty tube. The two porosities are roughly the same if the boundary pores are included (SLS structure). When the boundary pores are excluded (stereolithographic structures), the porosity in the tube is smaller. Similarly, a bulk hydraulic diameter and a hydraulic diameter of the manufactured structure can be distinguished. It is observed that the hydraulic diameter of the manufactured structure is smaller than the bulk hydraulic diameter. The reason is that there is more wetted surface due to the boundary of the tube.

The second geometry under investigation is a Sulzer SMX$^{\text{TM}}$ static mixer. It is made up of ligaments that are inclined at 45° with respect to the axial direction (Fig. 5.6). It has the same hydraulic diameter and same porosity as the foam-like porous structure. Table 2.2 lists its dimensions. A major difference between the foam-like porous structure and the SMX is the free cross-sectional area, i.e., the area in the tube that is not occupied by the porous structure. Fig. 2.4 shows the free cross-sectional area divided by the cross section of the empty tube as a function of the axial coordinate. On average, both geometries have a free cross-section of approximately 70.5 % (70.7 % and 70.4 %). However, the foam-like structure shows a wide range of variation (from 53 % to 92 %). In comparison, the free cross section in the SMX shows only a small range of variation (from 64 % to 75 %).
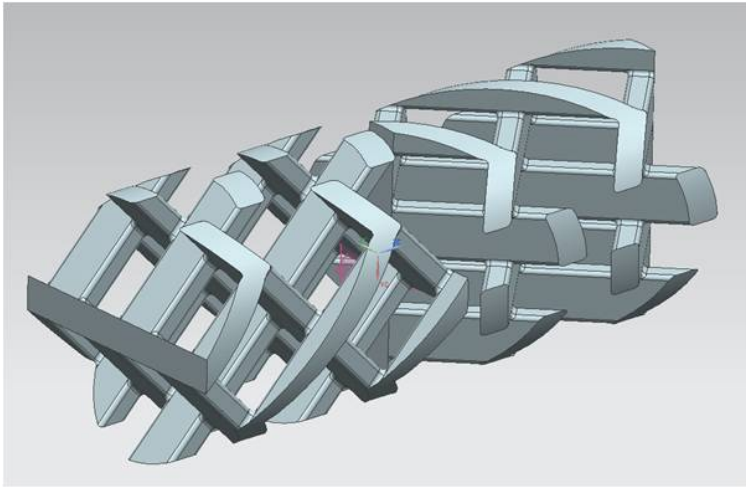
Figure 2.3: Four periodic units of a SulzerSMX$^{\text{TM}}$ static mixer. Left: auxiliary view, right: cut at measurement plane.

Table 2.2: Characteristic dimensions of Sulzer SMX

Empty pipe diameter D [mm]	20
Length of periodic unit [mm]	13.5
l_1 [mm]	27
l_2 [mm]	6.75
l_3 [mm]	2.8
l_4 [mm]	4
Porosity [%]	70.67
Bulk Porosity [%]	70.78
Hydraulic diameter [mm]	6.14
Bulk hydraulic diameter [mm]	9.48
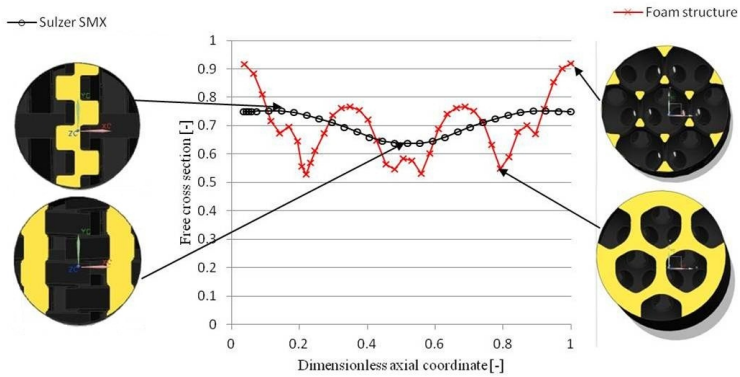
Figure 2.4: Free cross section along one periodic unit of the two geometries. Cut through Sulzer SMX^{TM} at the position of maximal and minimal free cross section (left). Cut through foam-like porous structure at maximal and minimal free cross section (right).

Chapter 3

Macroscopic study of heat transfer

This Chapter describes an experimental technique for the investigation of the total thermal diffusivity in a streamed porous structure. It is based on measuring the full 2D temperature field using a thermochromic liquid crystal foil. By a proper calibration of the color play of such foils they can be used for accurately measuring the temperature. From the observed temperature field the total thermal diffusivity is estimated by an optimum search in a numerical simulation of the macroscopic conservation equation.

3.1 Temperature measurement

Previous studies of dispersion measured the temperature point-wise by thermocouples (Kaviany, 1991, Sec. 4.8). Here, the full 2D temperature field will be measured using a thermochromic liquid crystal (TLC) foil. TLC foils show a gradual color change from red to green and blue with increasing temperature. The color change is repeatable and irreversibility is only observed when the temperature is much higher than the calibration range (Anderson and Baughn, 2004). With an appropriate calibration, the uncertainty can be as low as 1 % of the calibration range (Wiberg and Lior, 2004). For the calibration, the recorded image is transformed from RGB (red-green-blue) color space to the HSV (hue-saturation-value) color space. In this representation, the hue value uniquely relates to a temperature. Figure 3.3 shows calibration images (left) and the corresponding hue value distribution (right). The spatial

T = 22.9 °C

T = 27.5 °C

T = 33.8 °C
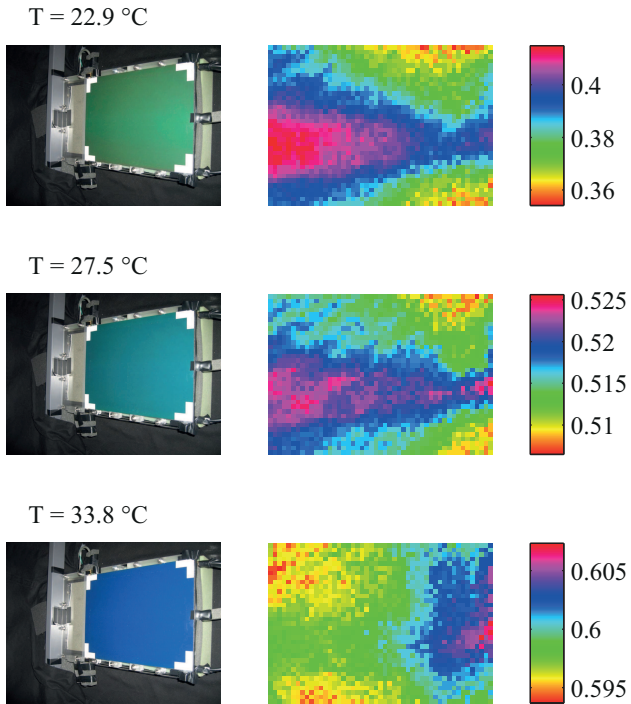
Figure 3.1: Raw images (left) and hue value distribution (right) for calibration measurements.
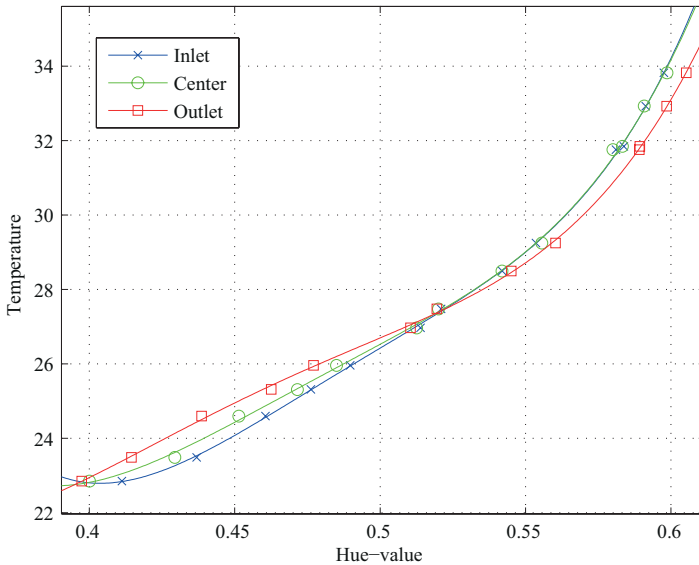
Figure 3.2: Calibration of TLC foil

variation of the hue value can stem from foil non-uniformity, viewing angle and lighting angle. In order to respect these effects, a point-wise calibration of the entire test surface was employed, like done by Sabatino et al. (2000). The first step in evaluating the image was to recognize the area of the measurement section in the image. For this, four white corners are placed on the TLC foil (see Fig. 3.1, left). The center of these white areas lies exactly at the boundary of the measurement domain. The measurement domain was then divided into 35×49 cells in cross-stream and stream-wise direction. In each of these cells, the hue value of the pixels was averaged. Figure 3.2 shows the calibration curves at three different positions along the centerline of the setup. It is observed that between $23\,°C$ and $34\,°C$, the hue value uniquely relates to a temperature. It is also observed that the colours recorded at different positions

are slightly different. This shows the necessity for a point-wise calibration of the TLC foil. The twelve calibration points are fitted by a fourth degree polynomial. The root mean square deviation of the calibration measurement and the calibration curve is $0.088\,°C$. The error of the temperature measurement is therefore assumed to be small in comparison to the useful calibration range of $11\,°C$.

3.2 Experimental setup

The setup was designed to fit the porous structure described in Section 2.1 with dimensions of $280 \times 200 \times 15$ mm. The principal scheme is shown in Fig. 3.3. Cold air flows through a porous structure. At the sides, hot water in hollow aluminum profiles provide heat. The foam and the aluminum profiles are sandwiched between two plexiglass plates. To ensure two-dimensionality, heat loss in the third dimension has to be prevented, what is achieved by cellular plastic material for insulation. The liquid crystal foil for measurement of the temperature is placed between the porous structure and the upper plexiglass plate. For the measurement, the upper cellular plastic was removed shortly before a picture was taken. For the imaging, a standard digital camera (Canon Digital IXUS 700) was used. The illumination was done by the integrated flash while the setup was isolated from other light sources. This is crucial because the color of the TLC foil depends on the color of the incident light and on its angle.

The temperature range of these experiments was only $10\,°C$. Therefore, care was taken that all effects from varying ambient temperature are excluded. All piping leading to the setup was therefore insulated. When setting new experimental conditions it was then waited until the temperature measured by thermocouples stayed withing $\pm 0.1\,°C$ for at least 30 min.

A critical issue in the design of this experiment is the assumption of two-dimensionality. To validate this assumption, the heat flux in x_3-direction and in x_2-direction is compared. The temperature difference between the fluid at the entrance and the aluminum side-walls was $\approx 10\,°C$. The maximum amount of heat that could be transferred from the aluminum profiles to the fluid (in x_2-direction) can be calculated
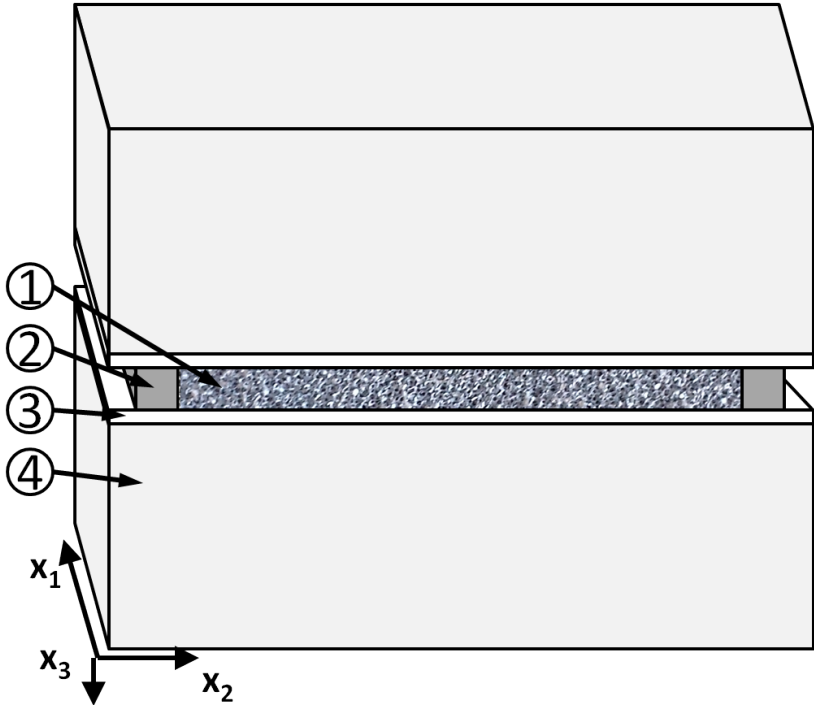
Figure 3.3: Illustration of setup showing the porous structure (1), the tempered aluminium profiles at the side walls (2), plexiglass plates on top and bottom (3) and a cellular plastic insulation both on top and at the bottom of the setup (4). The TLC foil is placed between the porous structure and the upper plexiglass plate.

by assuming that the fluid is heated by $10\,°\mathrm{C}$. The maximum heat is $54\,\mathrm{W}$ in the experiment with the highest flowrate and $18\,\mathrm{W}$ at the lowest flowrate. In x_3-direction, heat is lost to the environment. The low thermal conductivity of the plexiglass $(0.19\,\mathrm{W\,m^{-1}\,K^{-1}})$ and the cellular plastic $(0.04\,\mathrm{W\,m^{-1}\,K^{-1}})$ in series leads to a heat transfer coefficient as low as $0.5\,\mathrm{W\,m^{-2}\,K^{-1}}$. Assuming a temperature difference of $10\,°\mathrm{C}$ between the setup and the environment, the heat loss is only $0.55\,\mathrm{W}$. In other words the heat transferred through the top and bottom of the setup (x_3-direction) amounts to only $1\,\%$ to $3\,\%$ of the heat transferred to the side-walls (x_2-direction). It is therefore reasonable to model the temperature profile as two dimensional.

3.3 Model

The temperature field is modeled by a macroscopic conservation equation as introduced in Section 1.4. I assume constant thermophysical properties of the air. This is justified by the fact that the temperature variations are small, i.e. less than $10\,°\mathrm{C}$. The velocity is therefore modeled as homogeneous in the whole setup. Further assuming constant transport coefficients, isotropic porous medium, and local thermal equilibrium between the solid and the fluid, Eq. 1.23 applies. Further exploiting that there is steady state, no reaction, and derivatives in x_3 direction vanish, the equation simplifies to:

$$u_D \frac{\partial \langle T \rangle}{\partial x_1} = D_{\parallel} \frac{\partial^2 \langle T \rangle}{\partial x_1^2} + D_{\perp} \frac{\partial^2 \langle T \rangle}{\partial x_2^2} \tag{3.1}$$

For the evaluation of the experiments, the measurement domain is subdivided into square areas of $5.7\,\mathrm{mm}$ in which a homogeneous temperature is assumed. The temperature field is therefore subdivided into 35×49 values. Equation (3.1) is then discretized using a central finite difference scheme for the second derivatives and a backwards scheme for the convective term. As boundary condition for the simulation I took the measured temperatures at the boundary of the domain. In an optimum search the two transport terms are then iteratively estimated to minimize the root mean square difference between measured and simulated temperature. Figure 3.4 shows a comparison between a simulated (top) and

measured (bottom) temperature field. The cold air (22.7 °C) streams from left to right. The temperature of the water in the aluminum profiles is 32.3 °C. The fluid in the center heats up to ≈ 24 °C while at the boundary it reaches ≈ 28 °C. It was found that the simulated temperature field shows a good agreement with the measurements. This suggests that the employed model is appropriate.

3.4 Results and Discussion

I observed a good reproducibility of the lateral total thermal diffusivity. In contrast to that, the estimated longitudinal total thermal diffusivity shows a large uncertainty. The reason is that the second derivative in streamwise direction is around zero, i.e. the temperature profile is almost linear (Fig. 3.5, left). From Eq. (3.1) it is concluded that if $\frac{\partial^2 \langle T \rangle}{\partial x_1^2} \approx 0$, the longitudinal total thermal diffusivity $(D_\parallel)$ can take arbitrary values and the equation is still fulfilled. The optimum search is therefore made only for $D_\perp$. For $D_\parallel$, a value had to be assumed. As a test I set $D_\parallel$ to zero, equal to $D_\perp$, and to arbitrary other values. It was found that the estimated value of $D_\perp$ is weakly depending on the value set for $D_\parallel$. This means that $D_\perp$ can still be measured irrespective of the value of $D_\parallel$. For the following evaluations I assumed $D_\parallel = D_\perp$. This is motivated by the fact that both values equally include transport by conduction in the solid.

Figure 3.6 shows the resulting lateral total thermal diffusivity as a function of the hydraulic Reynolds number for experiments where the air is heated (x) and cooled (o). It is observed that the diffusivity is higher in the experiments where the fluid is cooled. This is attributed to heat losses to the environment, that are more important in the experiment where the air is cooled. At low flowrates, where the effect of heat losses is more important, the deviation between heating and cooling experiments is most significant. At the highest flowrate, the difference between heating and cooling experiments is not that pronounced. There, the deviation between the two experiments is 20%. Of these two experiments, the *heating* is more trustworthy, as in this experiment there is less temperature difference to the environment and therefore less heat losses. Further, the *cooling* experiments show an unexpected decrease of $D_\perp$ as
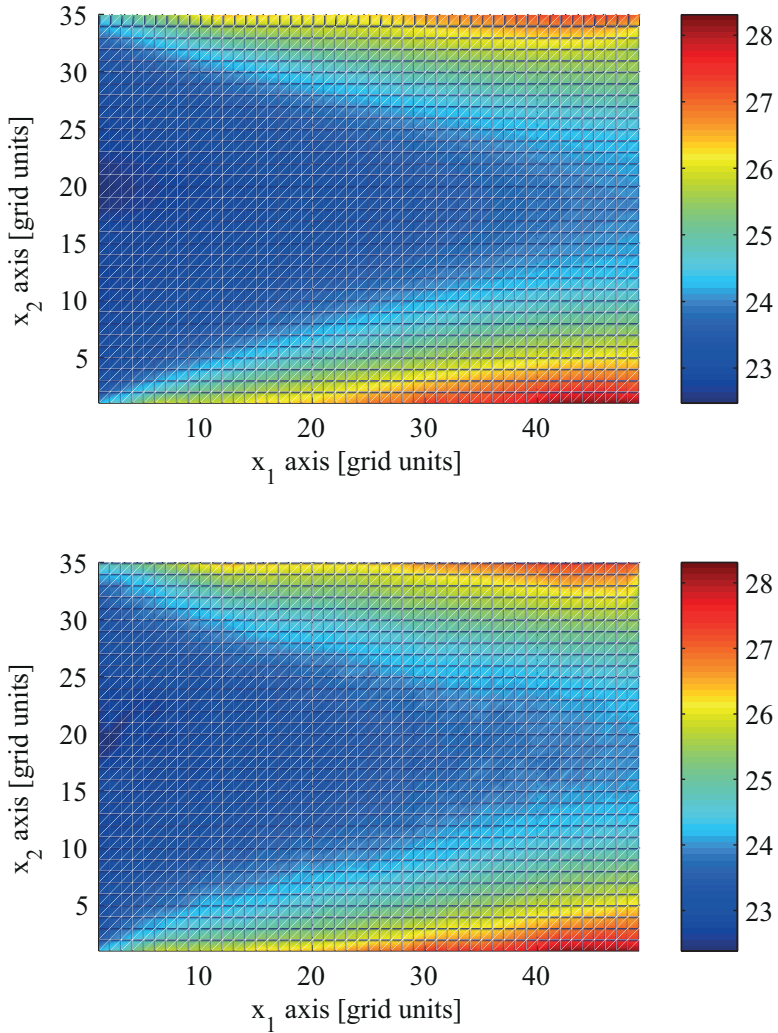
Figure 3.4: Simulated (top) and measured (bottom) temperature profiles [°C]. The cold fluid streams from left to right.
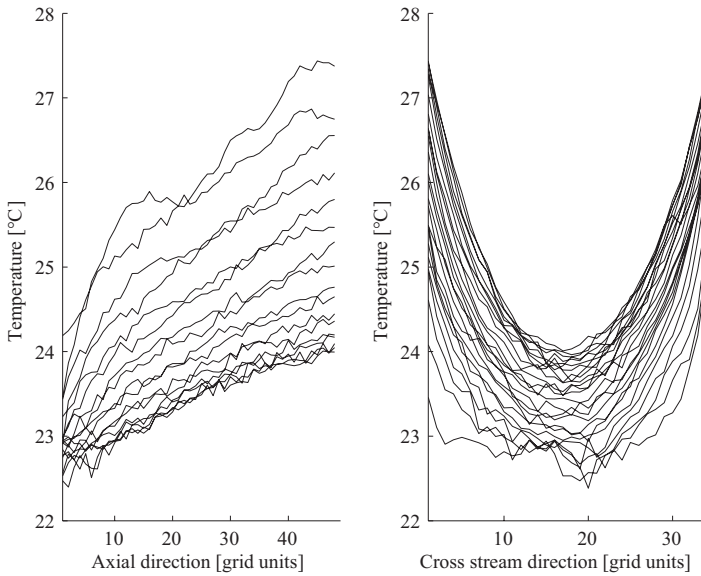
Figure 3.5: Temperature profile in longitudinal direction (left) and lat-
eral direction (right). It is observed that in longitudinal
direction the temperature profile is almost linear, i.e. the
second derivative is around zero.
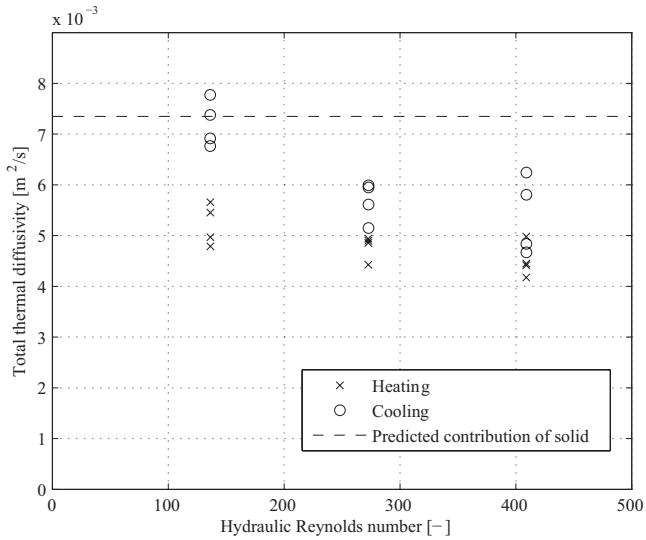
Figure 3.6: Total thermal diffusivity in lateral direction as a function of
hydraulic Reynolds number. In one case the air was heated
(x) and in the other it was cooled (o).

a function of the Reynolds number. Therefore I will compare the value of the *heating* experiment, of which the one at the highest flowrate is the most trustworthy, to values expected from theory. The experimental value at the highest flowrate is $4.5 \times 10^{-3} \, \mathrm{m^2 \, s^{-1}}$.

According to Eq. (1.26) it consists of the effective thermal conductivity of the foam structure (k_{eff}) and the thermal dispersion coefficient ($D_{\perp}^{d}$). An upper bound of k_{eff} can be calculated by assuming that the solid and the fluid in the porous structure are arranged as parallel slabs. In this case the effective thermal conductivity is given as:

$$k_{\mathrm{eff}} \leq (1 - \Phi) \, \lambda_s \tag{3.2}$$

More accurate predictions can be obtained by assuming that the porous structure is similar to some standard model. Examples can be found in Petrasch et al. (2008). If a more accurate model for k_{eff} is required, a numerical simulation or experiments could be made. For the foam used here, the effective thermal conductivity can be estimated from a simplified equation proposed by the manufacturer[1]:

$$k_{\mathrm{eff}} = 0.33 \, (1 - \Phi) \, \lambda_s = 8.85 \, \mathrm{W \, m^{-1} \, K^{-1}} \tag{3.3}$$

The idea behind this equation is that the porous structure is made up of ligaments which can be oriented in arbitrary directions. Statistically, one third of the ligaments will be directed in each direction in space. Therefore, the factor of 0.33 is contained in this correlation. To compare the effective thermal conductivity to the total thermal diffusivity (Eq. 1.26), it is divided by the volumetric heat capacity of the fluid:

$$\frac{k_{\mathrm{eff}}}{(\rho \, c_p)_f} = 0.007\,35 \, \mathrm{m^2 \, s^{-1}} \tag{3.4}$$

Below, I will compare this value to the experimental results. But first, the contribution of the fluid should be discussed.

The total thermal diffusivity will not only comprise transport by the solid, but also by the fluid (thermal dispersion). Kaviany (1991, Table 4.5) summarizes empirical correlations for thermal dispersion found in

---

[1] http://www.ergaerospace.com/Thermal-transfer.html consulted 12 Mar. 2014

the literature. Here, lateral thermal dispersion is predicted by:

$$D_\perp^d = \frac{3}{16} l \, u_D \tag{3.5}$$

according to de Josselin de Jong (1958). In this empirical correlation, l is a length scale related to the porous structure. For the theoretical considerations, de Josselin de Jong (1958) took l as the length of pores in a pore network while in the experimental validation they set l to one third of the diameter of the spheres comprising a packed bed. Assuming l as equal to the hydraulic diameter of the porous structure, the resulting thermal dispersion is $1.2 \times 10^{-4} \, \mathrm{m^2 \, s^{-1}}$ at the lowest flowrate and $3.9 \times 10^{-4} \, \mathrm{m^2 \, s^{-1}}$ at the highest flowrate.

Comparing the contribution of the solid (k_{eff}) and the fluid ($D_\perp^d$), it is observed that the contribution of the solid is more than one order of magnitude stronger. The contribution of the fluid can therefore be neglected. This means that the lateral total thermal diffusivity is predicted as follows:

$$D_\perp = \frac{k_{\mathrm{eff}}}{(\rho \, c_p)_f} \tag{3.6}$$

It is observed that the measured value of $D_\perp$ is $39\,\%$ lower than the one predicted by Eq. (3.3) and Eq. (3.6). The reason for this is that less than one third of the foam material is effectively conducting heat in the direcion of interest. This can be caused by accumulation of mass at junctions of ligaments. Further, constrictions in the ligaments could lead to a reduced effective thermal conductivity. Considering that such effects are not described by the simplified model of Eq. (3.3), the agreement between prediction and measurement is acceptable.

3.5 Conclusion

Thermochromic liquid crystal foils were used for the measurement of the full 2D temperature field in a streamed porous structure. From that, the total thermal diffusivity was estimated by fitting parameters of the macroscopic conservation equation. It is observed that the lateral total thermal diffusivity is reproducibly measureable whereas the longitudinal contains large uncertainty. The reason for this is that the temperature

field in longitudinal direction is almost linear, i.e., the second derivative is zero.

The effective thermal conductivity of the solid was predicted by a model given by the manufacturer. A correlation for lateral heat dispersion by the fluid suggests that the contribution of the fluid to heat diffusivity is more than one order of magnitude smaller than the contribution of the solid. The contribution of the fluid was therefore neglected in the model and a good agreement between the measured lateral total thermal diffusivity and the predicted effective thermal conductivity was observed.

The experience of applying the macroscopic conservation equations is that they are simple and that they can accurately describe the temperature field in a streamed porous structure. These conservation equations are useful to design and scale-up reactors with porous structures. In comparison, the scale-up of batch reactors usually involves a change of the characteristic dimension. With the change of the dimension, many parameters that define fluiddynamics and heat-/masstransfer, e.g., the Reynolds number, are changed. The temperature distribution can then be predicted by CFD models, i.e., solving momentum, mass, and energy conservation equations. The solution of these coupled equations is not trivial. In contrast to that, in a porous structure reactor the momentum conservation equation can be replaced by an algebraic equation. The task of modeling is therefore greatly simplified. The temperature distribution can be predicted by solving a simple macroscopic conservation equation.

Of course, the accuracy of the prediction is limited by the accuracy of the transport coefficients in the macroscopic model. A further complication compared to the experiments presented here is the choice of adequate boundary conditions when a real reactor is to be simulated. Boundary conditions have to be given at the inlet and outlet to the reactor and at the side walls. At the inlet and outlet nodes, the energy conservation equation has to consider the heat added/ removed by flow over the boundary. At the side walls, three cases can be distinguished. One case is where the side walls are insulated. In this case isolation boundary conditions apply. If the side wall contains a cooling jacket, the heat transfer coefficient between the wall and the porous structure has to be known. When the heat transfer coefficient can be assumed

sufficiently high, the temperature of the cooling jacket can be taken as boundary condition. Otherwise, the heat transfer coefficient has to be known for the implementation of the boundary condition.

Chapter 4

Macroscopic study of mass transfer[1]

This Chapter describes a macroscopic study of mass transfer in designed porous structures. In Section 1.4.2, a three dimensional macroscopic model of mass conservation in porous structures was introduced. Here, I use a porous structure with small extent in radial direction. Therefore, derivatives in these directions are neglected and the model becomes one dimensional. Further, it was assumed that there is no reaction and that the overall density is constant. With these assumptions, Eq. (1.22) simplifies to:

$$\frac{\partial \langle \rho_k \rangle^f}{\partial t} = D_L \frac{\partial^2 \langle \rho_k \rangle^f}{\partial x_1^2} - u_I \frac{\partial \langle \rho_k \rangle^f}{\partial x_1} \tag{4.1}$$

This model is usually referred to as the dispersion model. As the model is one dimensional, the axial coordinate will be called x instead of x_1. Further, the concentration of a substance is simply refered to as c instead of $\langle \rho_k \rangle^f$. Therefore, Eq. (4.1) reads as:

$$\frac{\partial c}{\partial t} = D_L \frac{\partial^2 c}{\partial x^2} - u_I \frac{\partial c}{\partial x} \tag{4.2}$$

In the following, the origin of the dispersion model is discussed. Then, I discuss how the dispersion coefficient depends on the length of the measurement section. Afterwards, I describe the experimental setup

---

[1] Parts of this Chapter has been published in: Häfeli R., Hutter C., Damsohn M., Prasser H.-M., Rudolf von Rohr Ph., (2013). Dispersion in fully developed flow through regular porous structures: Experiments with wire-mesh sensors. *Chem Eng Sci*, 69, $104 - 111$.

and an alternative method to evaluate pulse experiments. Finally, the results are presented and compared to literature data.

4.1 Theory

4.1.1 Dispersion in pipe flow

The dispersion model is a one dimensional model for a problem that has concentration and velocity fluctuations in three dimensions. The justification of this model has its origin in the work by Taylor G. (1953). He showed that even in laminar flow through a tube, where the velocity profile over the cross section is parabolic, the dispersion model is applicable provided that the time for convective transport

$$\tau_{\text{convection}} = \frac{L}{u} \tag{4.3}$$

is long compared to the time of decay during which radial variations of concentration are reduced to a fraction of their initial value through the action of molecular diffusion:

$$\tau_{\text{radial diffusion}} = \frac{(D/2)^2}{3.8^2 D_m} \tag{4.4}$$

where a is the empty pipe radius. From this, a criterium on the minimum length of a measurement section can be deduced:

$$L \gg \frac{u\,(D/2)^2}{3.8^2 D_m} \tag{4.5}$$

When this condition is fulfilled, the concentration profile can be modeled as one dimensional, i.e. the dispersion model is valid. He predicted the dispersion coefficient for laminar flow through a tube as:

$$D_L = \frac{D^2 u^2}{192 D_m} \tag{4.6}$$

Note: Taylor G. (1953) gives the dispersion coefficient as a function of the maximum velocity at the axis and the pipe radius. Alternatively, the

pipe diameter and the average velocity can be taken. Doing this leaves the correlation unchanged. Taylor G. (1954) recites this formula with a factor of 48 instead of 192. The reason is that there he used the pipe radius and the average velocity.

Later the dispersion model was applied to turbulent flow (Taylor G., 1954). By assuming the universal velocity profile over the cross section, he predicted mass transport by employing Reynolds analogy. Like this, he predicted the contribution of Taylor dispersion to longitudinal dispersion as:

$$D_L^u = 10.06 \ (D/2) \ v_* \tag{4.7}$$

Further assuming isotropy of turbulence, he predicted the contribution of turbulent diffusivity to longitudinal dispersion as:

$$D_L^{u'} = 0.052 \ (D/2) \ v_* \tag{4.8}$$

The sum of the two contributions gives the longitudinal dispersion coefficient:

$$D_L = 10.1 \ (D/2) \ v_* \tag{4.9}$$

In these equations, the dispersion coefficient is given as a function of the pipe diameter D and the friction velocity v_*. Taylor G. (1954, Table 2) showed that the friction velocity can be well approximated by a linear function of the logarithm of the Reynolds number. With a linear regression to his data, the friction velocity in Eq. (4.9) can be replaced. The longitudinal dispersion coefficient is therefore given as:

$$D_L = 10.1 \ (D/2) \ u \ (5.03 \, log_{10} \mathrm{Re} - 4.01) \tag{4.10}$$

In contrast to laminar flow, no criteria on the minimum length of a measurement section was proposed.

My conclusion from the works of Taylor is that the characteristic of the dispersion coefficient is different in laminar and turbulent flow. While in laminar flow the dispersion coefficient is proportional to the velocity squared $\left(D_L \sim u^2\right)$, in turbulent flow the dispersion coefficient as a function of velocity rises slower, i.e. $D_L \sim u log(u)$. This is an observation that can also be made in flow through packed beds. However, there the dispersion coefficient shows a different proportionality to the velocity. This will be discussed in the following.

4.1.2 Dispersion in packed beds

In flow through porous media, dispersion is described by a different power law than in empty pipes (Pfannkuch, 1963). Further, there is an additional length scale involved, i.e. the size of the particles. The dispersion coefficient in a packed bed of spheres can therefore be assumed to be a function of following parameters:

$$D_L = f\left(L, D, u_I, d, \rho, \mu, D_m\right) \tag{4.11}$$

where L and D are the length and diameter of the column, d the particle diameter of the packed bed, and ρ and μ the density and viscosity. When effects of the column length L and diameter D can be neglected, the dispersion coefficient is a function of only two dimensionless numbers (Delgado, 2006):

$$D_L = f\left(Pe_m, Sc\right) \tag{4.12}$$

where $Sc = \nu/D_m$ is the Schmidt number and $Pe_m = \frac{u_I d}{D_m}$ is the molecular Peclet number. Further, the dispersion coefficient can be made dimensionless by either dividing it by the molecular diffusion coefficient:

$$\frac{D_L}{D_m} \tag{4.13}$$

or by dividing it by a velocity and a length scale:

$$\frac{D_L}{u_I d} \tag{4.14}$$

Depending on the molecular Peclet number, five dispersion regimes can be identified (Pfannkuch, 1963). Figure 4.1 shows $D_L/\left(u_I d\right)$ as a function of the molecular Peclet number Pe_m. At low Pe_m (low flowrates), dispersion occurs primarily due to molecular diffusion (I). At higher Pe_m, both molecular diffusion and mechanical dispersion have to be taken into account. Some authors distinguish between a regime in which molecular diffusion is stronger (II) and one in which mechanical dispersion is stronger (III) (Pfannkuch, 1963; Fried and Combarnous, 1971). Others identify this as a single regime (Brenner, 1980). At higher Pe_m, a regime of pure mechanical dispersion (IV) can be identified. In this regime, the
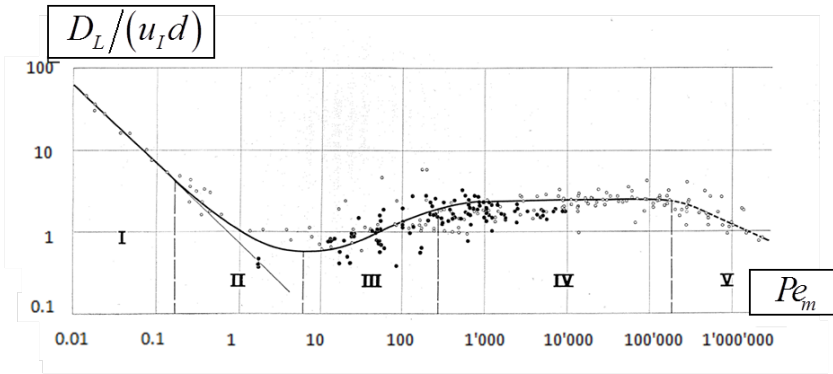
Figure 4.1: Dispersion regimes according Pfannkuch (1963). The dispersion coefficient divided by the particle size and the velocity, is plotted as a function of the Peclet number.

dispersion coefficient is directly proportional to the velocity (Pfannkuch, 1963, Eq. (4.4)):

$$\frac{D_L}{u_I\, d} = 1.8 \tag{4.15}$$

In this regime, the flow is laminar. In the last dispersion regime (V), different effects start to play a role and $D_L/(u_I d)$ in Fig. 4.1 decreases. Sahimi (1995) attributed this to turbulent effects. In contrast to that, Brenner (1980) classified the last dispersion regime as non-Darcy flow, i.e. effects in the viscous-inertial regime. Hlushkou and Tallarek (2006) argued that it would be more appropriate to describe the transition between regimes (IV) and (V) by the Reynolds number and not by the molecular Peclet number. They recalculated the Reynolds number from the Peclet numbers of Sahimi (1995) and Brenner (1980). Assuming that water was used in the experiments, they found that the transition between regimes (IV) and (V) occurs at $Re_{part} \approx 86$ and $Re_{part} \approx 172$. This corresponds to Reynolds numbers where onset of fluctuations is expected. The decrease of the dispersion coefficient in regime (V) was therefore attributed to lateral equilibration of velocity extremes. (Remark: In some of the mentioned literature, the designation of the

dispersion regimes is different, because regimes (II) and (III) are combined.)

4.1.3 Dispersion model and residence time distribution

In this section, I will discuss how the differential equation given in Eq. (4.2) is associated to the residence time distribution in a tubular reactor of length L. As the word says, the residence time distribution is the probability, how long a molecule stays inside a reactor. Experimentally, it can be measured by instantaneously injecting a tracer substance at the entrance of the reactor while measuring the mass flux of this substance at the outlet. Mathematically, the residence time distribution resulting from a system described by Eq. (4.2) can be determined by analytically solving the equation. To solve the differential equation, boundary and initial conditions have to be defined. One possibility is to assume an infinitely long section. Such a model well represents a reactor of length L, if dispersion over the entrance and exit is allowed. This boundary condition is referred to as open-open boundary condition. As initial condition, a Dirac pulse at the inlet of the reactor at time zero is assumed. Like this, the differential equation can be solved analytically. The concentration profile at the position of the outlet ($x = L$) is associated to the residence time distribution (Levenspiel, 1999, pg. 301):

$$E(t) = \frac{1}{\tau \cdot \sqrt{4 \cdot \pi \cdot \frac{D_L}{u_I \cdot L} \cdot t/\tau}} \cdot exp\left(\frac{-(1 - t/\tau)^2}{4\frac{D_L}{u_I \cdot L} \cdot t/\tau}\right) \tag{4.16}$$

The dispersion model describes the residence time distribution by only two parameters: the mean residence time τ and the longitudinal dispersion coefficient D_L. Alternatively, the dimensionless group $\frac{D_L}{u_I \cdot L}$ is used. This number is called vessel dispersion number (Levenspiel, 1999). Sometimes, its inverse is used and called Bodenstein number. The Bodenstein number is a special type of Peclet number. In this dissertation i will refer to $\frac{D_L}{u_I \cdot L}$ as *vessel dispersion number*. A narrow residence time distribution is associated with a small value of of the vessel dispersion number.

The residence time distribution given by Eq. (4.16) is only valid under certain assumptions. It is the analytical solution for the differential equation for a Dirac pulse $\delta(x_1)$ at time zero. However, what is actually required is to have a Dirac pulse $\delta(t)$ at the inlet. If the vessel dispersion number is small enough, the Dirac pulse is transported downstream before its shape changes. For large vessel dispersion numbers, the shape of a pulse will change as it travels across the boundary. According to Levenspiel (1999), "the literature for this case is profuse and conflicting, primarily because of the unstated and unclear assumptions about what is happening at the vessel boundaries". He did however not give an exact limit, up to which vessel dispersion number the model is still valid. He writes that the dispersion model is questionable when $\frac{D_L}{u_I \cdot L} > 1$. In the experiments presented below, this criterion will be evaluated.

4.1.4 Length dependence of dispersion coefficient

The following section attempts to review the most important literature on the length dependence of the dispersion coefficient and on flow in the entrance section of a pipe and of porous structures.

Danckwerts (1953) wrote in one of the first publications on the dispersion model: "D_L should, of course, be independent of L for a given u". In the same year Taylor G. (1953) showed that in laminar flow through a tube, the axial dispersion can be described by the dispersion model, provided the length of the pipe exceeds a certain minimum (Eq. (4.3) and Eq. (4.4)). When this condition is not fulfilled the dispersion is non-Fickian and cannot be described by the dispersion model. When the dispersion model is applied to laminar pipe flow without fulfilling this condition, a dispersion coefficient varying with the length is obtained. To the best of my knowledge, a similar rule for turbulent flow is not available in literature.

Levenspiel and Smith (1957) mentioned two conditions for the dispersion model to hold: uniform velocity profile or long enough measurement section. Later studies (Koch and Brady, 1985, 1987) on the length effect identified the laminar boundary layer on the surface of a solid as an effect that cannot be described by the dispersion model.

The continuing research on this topic shows that no closed theory was developed that allows to exclude all length effects. Delgado (2006)

mentioned in his review article, in a much weaker form than Danckw-
erts (1953), that the dispersion coefficient *should be* independent of the
length, if an experimental method is valid. Nevertheless he then referred
to Han et al. (1985), who gave a criterion on the minimum length of a
measurement section in order to reach a constant value of dispersion coef-
ficient. A satisfactory explanation why the dispersion coefficient changes
with the length is however not given. Han et al. (1985) only mentioned
that this behaviour is attributed to turbulence effects.

4.2 Experimental

The macroscopic study of mass transfer is done in a porous structure
manufactured by selective laser sintering. The geometric specifications
are given in Table 2.1. In this Section, I will first describe the wire-mesh
electrode used for concentration measurements. I will show experiments
where radial concentration variations are measured by the wire-mesh
sensor and by laser induced fluorescence. Subsequently, the experimen-
tal setup for pulse experiments is described. Finally, the evaluation
procedure for the dispersion coefficient is shown.

4.2.1 Measurement technique

Depending on the application, authors used various different tracers like
radioactive substances to measure in pipelines (Hull and Kent, 1952) and
fluorescent dyes to measure in microreactors (Trachsel et al., 2005). Of-
ten used tracer substances are aqueous salt solutions that can be tracked
by their conductivity. I decided to use potassium chloride as tracer in
water in combination with a wire-mesh sensor for measurement of con-
ductivity. The working principle of a wire-mesh electrode was described
by Prasser et al. (1998). The sensor built for this investigation fits in
a tubular cross-section with an inner diameter of 7 mm like shown in
Fig. 4.2. The sensor consists of two planes of parallel wires made of
stainless steel 1.4304 with a diameter of 50 μm. The two planes are or-
thogonal to the flow direction. The distance between two wires of the
same plane is 0.78 mm. The distance from the first to the second plane is
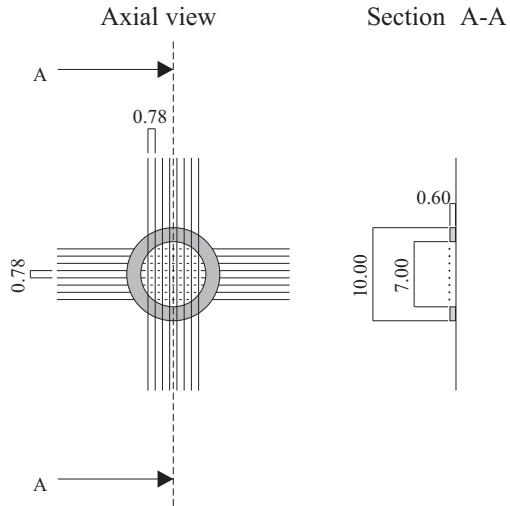0.6 mm. The upstream wires are rotated by 90 degrees against the down-

Figure 4.2: Wire-mesh sensor for measurement of conductivity distribution over cross-section of 7 mm inner diameter. Dimensions in mm.

stream wires in order to generate a plurality of sensitive nodes. The wires upstream act as transmitters, the wires downstream as receivers. The transmitters are consecutively activated applying a rectangular pulse with a positive and a negative period. The voltage applied to a single transmitter causes a current from the transmitter wire through the measuring volume to the receiving wire. Operational amplifiers in the transmitter lines guarantee that all non-active wires are kept on ground to avoid any cross talk, explained in detail by Prasser et al. (1998). The current arriving at the receiving lines is transformed into a voltage by the operational amplifiers and sampled by individual sample/hold circuits (data aquisition system of teletronic Rossendorf GmbH). After an analogue/digital conversion the signals are recorded by a data acquisition computer. The system has a high measurement frequency of 10 kHz. The data is finally stored in a matrix whose dimensions are defined by the number of transmitter (number of matrix rows) and receiver wires (number of matrix columns) for every time step. Due to the fact that not all crossing points are within the measurement section I sample only 52 points although the sensor consists of 8×8 wires. The resistance of the wires is very low compared to the resistance of the fluid. The resistance of the wires plus its connections and cables to the AD converter is measured to be $27\,\Omega$. The minimum resistance of the fluid in the electrode is $34\,\mathrm{k}\Omega$ when it has a concentration of $0.3\,\mathrm{g\,L^{-1}}$. This is the concentration of the tracer pulse that dilutes on the way from injection to the first sensor, leading to a minimum resistance that is higher than $34\,\mathrm{k}\Omega$ in all experiments. Therefore I can assume that the current at the receiver wires depends linearly on the conductivity of the fluid. In two-phase flow the conductivity is correlated to the liquid volume fraction in the measurement volume (e.g. Prasser et al., 2005). In my experiments, the measured signal is correlated to the concentration of a dissolved salt (KCl).

In order to demonstrate that the sensor is able to measure radial concentration profiles, a series of radial mixing experiments was performed with the wire-mesh sensor and by laser induced fluorescence (LIF). For the LIF experiments Rhodamine B was injected in front of a packing of 5 cm length. In a laser sheet at the outlet of the packing the radial concentration distribution was recorded with a camera. For details regarding the employed LIF technique I refer to Hutter et al. (2010). Exactly the

same measurements were done with the wire-mesh sensor with potassium chloride as tracer substance. The Schmidt numbers ($Sc = \frac{\nu}{D_m}$) of the two substances are 530 for KCl and 2400 for Rhodamine B. For this estimation, the diffusion coefficient of KCl was taken as $1.9 \times 10^{-5}\,\text{cm}^2\,\text{s}^{-1}$ according to Harned and Nuttall (1947). The diffusion coefficient of Rhodamine B is taken as $4.2 \times 10^{-6}\,\text{cm}^2\,\text{s}^{-1}$ according to Gendron et al. (2008). The difference in Schmidt numbers means that molecular diffusion is not equally important in the two experiments. However, at the Reynolds numbers under investigation, the convective transport outweighs diffusive transport.

For the evaluation of the mixing performance, the coefficient of variation (CoV) is chosen. The CoV of a single frame is defined as the standard deviation divided by the mean of the concentration distribution over the cross section. The temporal mean CoV is then calculated as the mean of fifty measurements. A low value represents a homogeneous concentration distribution.

Figure 4.3 shows the CoV measured by LIF and with the wire-mesh sensor at different hydraulic Reynolds numbers. At low flowrates I observe an inhomogeneous tracer distribution. At higher flowrates the mixing performance steadily increases as the flow becomes more turbulent. The CoV of a well mixed Rhodamine tracer measured by LIF is 7.12×10^{-3} In the experiments I observe a CoV at the highest flowrate of 8.24×10^{-2}. This means I did not reach the limit of the experimental method. The observed flattening of the curve at high flowrates must therefore be physical. What acts against a further decrease is the shorter residence time at higher flowrates.

It has to be mentioned that a quantitative comparison of mixing experiments done with different methods is generally not possible, however trends should be similar allowing a semi-quantitative comparison Wadley and Dawson (2005). There are various reasons like the different temporal and spatial resolution of the two methods. The different spatial resolution, which is $778\,\mu\text{m}$ with the wire-mesh sensor and $50\,\mu\text{m}$ with LIF, leads to different results for the CoV as length scales smaller than the characteristic sampling size cannot be detected. Another reason why the two measurement techniques do not lead to identical results is that the tracers do not have the same diffusion coefficient. And finally the two sensors do not show the same characteristic regarding non-homogeneous
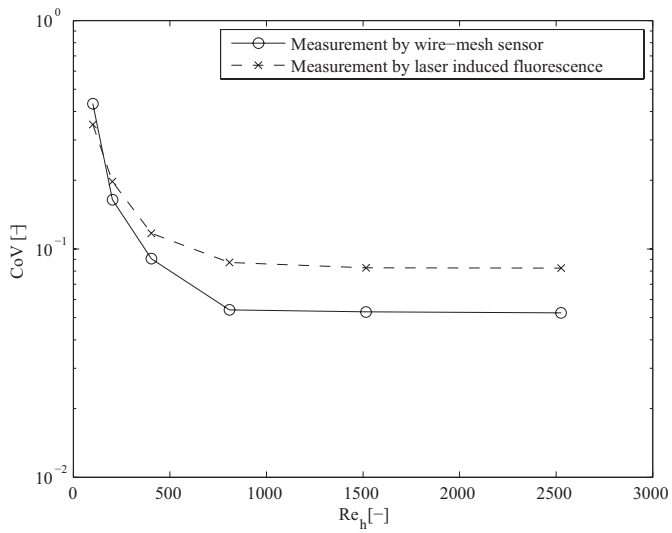
Figure 4.3: Radial mixing expressed with the coefficient of variation (CoV), measured by LIF and by the wire-mesh sensor.
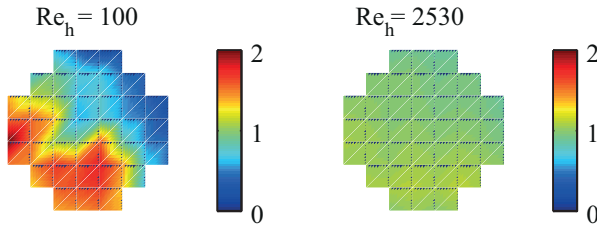
Figure 4.4: Normalized radial concentration distribution c/c_{mean} measured by the wire-mesh sensor after a mixing element of 50 mm length.

tracer within a measurement volume. The local conductivity reading of the wire-mesh sensor is a result of a three-dimensional electrical potential field established between crossing wires of the sensor. The local conductivity enters as a factor in the potential field equation. In case of strong non-uniformity of the tracer concentration, the sensor signal is therefore not exactly proportional to the tracer concentration within the measuring volume formed by the electrodes. In contrast to that, I can expect that the fluorescence intensity in the LIF measurements is always proportional to the mean concentration of Rhodamine in the corresponding volume, irrespective of the spatial distribution of the tracer. This difference might contribute to the deviation between the two techniques.

In spite of the differences of the two measurement techniques there is a fairly good agreement of the results (Figure 4.3). The maximal deviation of the CoV obtained by the wire-mesh sensor to the one obtained by LIF is 36.3 %. For both measurement techniques the CoV is decreasing with increasing hydraulic Reynolds number and the absolute values are also comparable.

Figure 4.4 shows a normalized concentration distribution over the cross section measured by the wire-mesh sensor. It is observed that at low flowrates ($Re_h = 100$), the tracer is inhomogeneously spread over the cross section, i.e. it is concentrated on the bottom left of the reactor. At higher flowrates ($Re_h = 2530$) the turbulent mixing increases, leading to
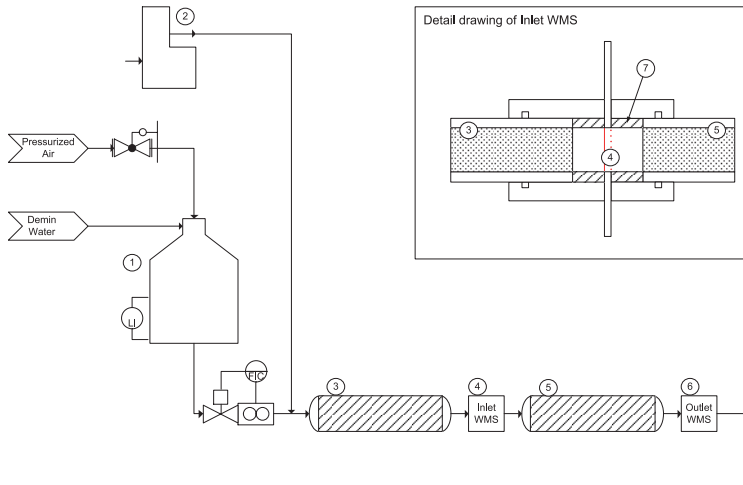
Figure 4.5: Experimental setup used for pulse experiments. 1: demineralized water tank pressurized by an air cushion up to 7 bar. 2: Syringe pump for tracer pulse injection. 3: First porous structure (premixing section). 4: inlet wire-mesh sensor. 5: Second porous structure (measurement section). 6: Outlet wire-mesh sensor. 7. Teflon ring for defined axial spacing of 5 mm.

a smooth tracer distribution over the cross-section.

These measurements have proven that the wire-mesh sensor is able to measure radial concentration variations. If radial concentration variations will be observed in the axial dispersion experiments, this would be recorded by the measurement device. As will be seen below, no radial concentration variations are observed in the axial dispersion experiments.

4.2.2 Setup for pulse experiments

The experimental setup for the axial dispersion measurements is shown in Fig. 4.5 with a detail drawing of the arrangement at the inlet wiremesh sensor. The configuration at the outlet sensor is similar. The

demineralized water is supplied from a tank pressurized with air. The mass flow controller (Bronkhorst CORI-FLOW M55C4) allows to control the flow up to $180\,\mathrm{kg\,h^{-1}}$ with an accuracy of $0.2\,\%$. The water flows through a calming section of $1\,\mathrm{m}$ length and $7\,\mathrm{mm}$ diameter before it enters the first porous structure. The function of the first porous structure is to homogenize the tracer in radial direction and to allow the flow field to develop. The dispersion is then measured over the second porous structure where, based on the literature reviewed above, I expect fully developed flow. The distance of the wire-mesh to the porous structure is $5\,\mathrm{mm}$ in axial direction to avoid electrical current through the porous structure. For the pulse injection a syringe pump was used with KCl as tracer substance.

4.2.3 Determination of RTD from pulse experiments

Due to manufacturing tolerance, not every node of the wire-mesh sensor has the same sensitivity. For this reason a calibration measurement has to be done. This is achieved by measuring the conductivity of water with a defined salt concentration and with demineralized water. The measured signal from the experiment can then be linearly interpolated between the concentrations in the calibration. When the tracer is not distributed homogeneously, it is questionable wheter a linear characteristic between conductivity and concentration can be assumed. I consider this as an error source in the measurements of radial mixing discussed above. However in the measurements of axial dispersion I will show that the tracer distribution is one-dimesional (Fig. 4.6). This justifies the assumption of proportionality between tracer concentration and conductivity.

The mean value over the cross section of both inlet and outlet sensor was then calculated. Further, when no tracer mass is lost in the reactor, the inlet and outlet mass flow has to be equal. Therefore, the area under the curves $c_{in}(t)$ and $c_{out}(t)$ were both normalized to be 1.

Injecting a Dirac pulse of tracer at the inlet of the reactor would allow the direct measurement of the residence time distribution at the outlet of the reactor. However, if the tracer pulse at the inlet is broad, the outlet signal is given as the convolution of the inlet signal and the residence

time distribution:

$$c_{out}(t) = \int_0^t c_{in}(t^*) \cdot E(t - t^*) \cdot dt^* \qquad (4.17)$$

When the concentration profiles are measured at the inlet and at the outlet, the residence time distribution can be determined by deconvolution of the signals. This requires a Fourier transformation, filtering and inverse Fourier transformation (Hutter et al., 2011a). Alternatively, the residence time distribution can be determined from experimental data by fitting parameters of a RTD model to fulfill Eq. (4.17). It was found that this is a very convenient evaluation procedure. In contrast to the method with the Fourier transformation that requires filter parameters, this method does not require any manual settings. Further, it allows to treat any experimental data, i.e. with arbitrary $c_{in}(t)$. For $E(t)$ in Eq. (4.17) I used the dispersion model (Eq. 4.16), that gives the residence time distribution as a function of two parameters: the mean residence time τ and vessel dispersion number $\frac{D_L}{u_I \cdot L}$.

4.3 Results and Discussion

4.3.1 Dispersion in foam-like porous structure

The radial distribution of the tracer pulse is shown in Fig. 4.6 as a pseudo sideview. It can be seen that the tracer arrives as a plug, i.e. simultaneously at the center and at the boundary of the tube. I conclude that the radial mixing is very fast and a one dimensional model for mass conservation is appropriate. With other electrodes this information cannot be obtained, what emphasizes the advantages of the wire-mesh sensor for the measurement of dispersion.

The data of the individual nodes of the wire-mesh sensor are then averaged. This results in two concentration profiles at the inlet and at the outlet respectively (Fig. 4.7). Additionally the convoluted signal of the inlet profile and the residence time distribution are shown. It can be seen that this curve shows a good qualitative agreement to the concentration profile at the outlet. This implies that the dispersion model can accurately describe axial dispersion in the porous structure.
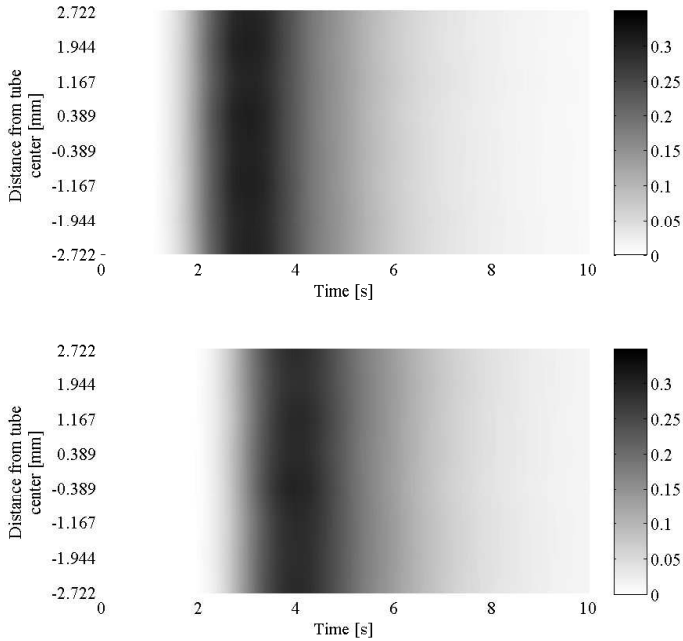
Figure 4.6: Pseudo side-view of tracer pulse (normalized concentration $\frac{c(t)}{\int_0^\infty c(t)dt}$) at inlet (top) and outlet (bottom). The graph contains the measurements of a wire in the center of the tube at a hydraulic Reynolds number of $Re_h = 400$. This graph shows that a radial concentration gradient was not observed in the measurement of axial dispersion.

Figure 4.7: Comparison of measured concentration profile at the outlet and convolution of inlet concentration profile with residence time distribution.

Figure 4.8: Estimated mean residence time versus expected mean residence time.

The dispersion model contains two parameters: the mean residence time and the vessel dispersion number. The measured mean residence time can be compared to the expected mean residence time:
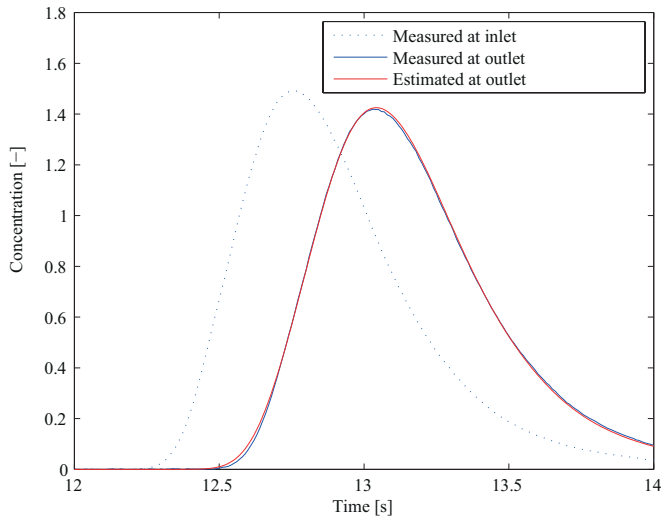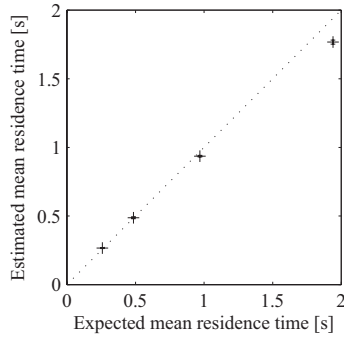
$$\tau_{exp} = \frac{L}{u_I} \tag{4.18}$$

The comparison in Fig. 4.8 shows a good agreement. The deviation is increasing with increasing residence time, what is attributed to the higher uncertainty of the flow controller at low flowrates. The relative deviation is always lower than 9 %.

The second parameter of the dispersion model is the (dimensionless) vessel dispersion number. Alternatively, results can be discussed based on the dispersion coefficient, that has units of $\mathrm{m^2\,s^{-1}}$. In Fig. 4.9, the dispersion coefficient is plotted over the hydraulic Reynolds number. Each point reflects the mean of five pulse experiments. The standard deviation of these five experiments is very low, except for the experiment at $Re_h = 810$ where the standard deviation is 21 %. The reason is that in one of the five experiments a lower dispersion coefficient was measured.
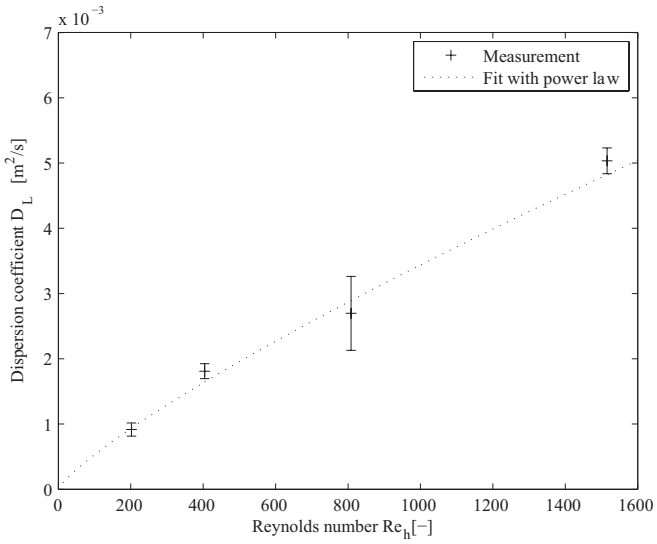
Figure 4.9: Dispersion coefficient as a function of hydraulic Reynolds number.
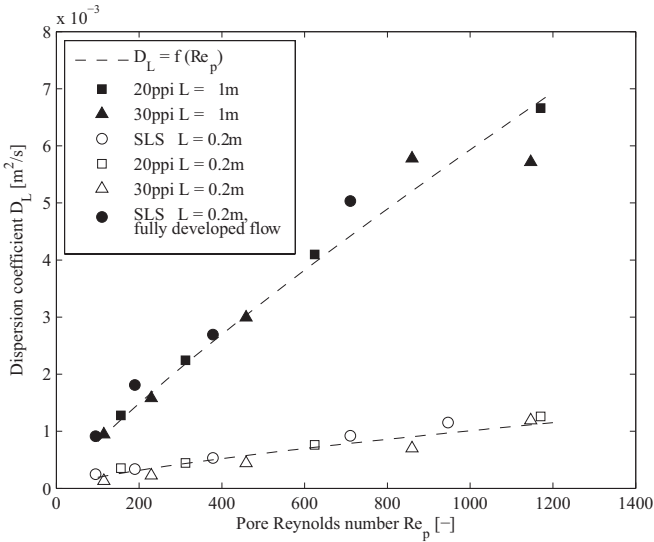
Figure 4.10: Dispersion coefficients in fully developed flow through the
selective laser sintered (SLS) structure of 0.2 m length,
compared to experiments by Hutter et al. (2011a). Ex-
periments where the entry section is expected to play a
major role are represented by white symbols. Note that
here, Reynolds numbers are defined with the pore diame-
ter (Hutter et al., 2011a).

4.3.2 Entrance section

The obtained dispersion coefficients are compared to experiments where
the porous structure in front of the inlet sensor (③ in Fig. 4.5) was
replaced by an empty pipe. Like this, two situations are investigated:
dispersion in fully developed flow and dispersion in the entry region.
Figure 4.10 shows the dispersion coefficient for the experiment with a
porous structure at the inlet (•) and with an empty pipe (◦). The two
experiments differ by a factor of ≈ 5. Figure 4.10 further includes the
dispersion coefficient in unregular foam structures (Hutter et al., 2011a).

The pore size of these foams is given by the manufacturer as 20ppi and 30ppi (pores per inch). Hutter et al. (2011a) observed that the different packings of 0.2 m length have similar axial dispersion coefficients (white symbols in Fig. 4.10). As all structures have similar characteristic dimensions and geometry, it can be expected that also the dispersion coefficient is similar. In the porous structures of 1 m length they observed a higher dispersion coefficient (■, ▲). As was discussed in Section 4.1.4, the dispersion coefficient can depend on the length of a measurement section. It should be discussed here wheter one of the reasons given there applies in my measurements. One reason is that the measurement section has to have a minimum length in order to allow modeling the concentration profile as one dimensional. For laminar flow, Taylor G. (1953) derived an analytic expression for the minimum length that is required to model the concentration as one dimensional (Eq. 4.5). To the best of my knowledge, a similar rule for turbulent flow is not available in literature. However, from the radial concentration profiles (Fig. 4.6), it can be concluded that it is adequate in my case to model the concentration as one-dimensional. A second reason for a length dependent dispersion coefficient can be that the vessel dispersion number is too high (Section 4.1.3). At high vessel dispersion numbers (> 1) it is questionable wheter the relation between dispersion model and residence time distribution is applicable. In my experiments, the vessel dispersion number was between 0.033 and 0.045. It can therefore be expected that the residence time distribution model given in Eq. (4.16) is applicable. In summary, no effect was found that would explain the differences between short and long measurement sections.

Therefore, I propose the hypothesis that the entrance region is an effect that leads to a length dependent dispersion coefficient. When a pulse experiment is made in the entrance region of a porous structure, the result is different from a measurument in fully developed flow. If a measurement is made in a long section that includes the entrance region, the dispersion coefficient is an average of dispersion in the entrance region and in fully developed flow. When the measurement section is much longer than the entrance section, the entrance section eventually becomes negligible and a dispersion coefficient characteristic for fully developed flow can be observed.

To judge the importance of the entrance effect, the length of the en-

trance section has to be known. In Section 6.1, the most important literature about entrance flow will be reviewed. Dukhan and Suleiman (2014) found that the entrance length in flow through porous structures is about six cells. In the foam-like porous structure, the entrance length will be studied by particle image velocimetry (Section 6.1). According to these measurements the flow can be considered as fully developed after maximal five periodic units. This is rather short (≈ 30 mm) compared to the total length of the measurement section in the dispersion experiments (200 mm). Therefore, judging from the PIV measurements, entrance effects are present but their importance is expected to be small in measurement sections that are long enough. It is still possible that other characteristics of the flow, e.g., recirculation zones and the laminar boundary layer in the vicinity of the wall, are only developed after a longer entrance section. These phenomena are known to effect axial dispersion (Koch and Brady, 1985). Due to the limitation of the measurement technique, these effects could however not be investigated by particle image velocimetry.

4.3.3 Dispersion regime

The obtained value of the dispersion coefficient can be assigned to a dispersion regime by comparison to literature (Section 4.1.2). Figure 4.11, shows my experimental results as a function of the molecular Peclet number in comparison to experiments collected by Pfannkuch (1963). For the calculation of $\frac{D_L}{u_I d}$, the hydraulic diameter of the structure was taken as the characteristic diameter. My experimental values are in the dispersion regime (V). According to Fig. 4.11 they could also be in dispersion regime (IV). However, the limit between the two regimes is defined by the onset of velocity fluctuations (see Section 4.1.2). And the onset of velocity fluctuations is defined by a Reynolds number Re_{crit}. The molecular Peclet number that defines the onset of velocity fluctuations (Pe_{crit}) can be written as a function of the Reynolds number:

$$Pe_{m,crit} = Re_{crit} \cdot Sc \tag{4.19}$$

The Peclet number that defines the onset of velocity fluctuations is therefore a function of the Schmidt number Sc. The decision whether my experiments are in the dispersion regime (IV) or (V) can therefore not
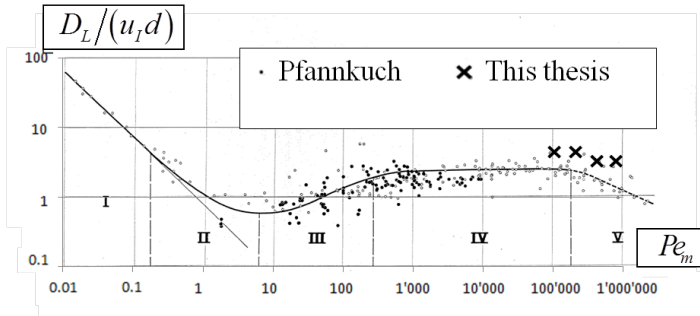
Figure 4.11: Assignment of experiments in foam like porous structure ($\times$) to a dispersion regime according to Pfannkuch (1963).

be made based on the limit given in Fig. 4.11. There are two options to check wheter the experiments are in dispersion regime (IV) or (V). The first option is to calculate the Reynolds number to check wheter velocity fluctuations are expected. The Reynolds number in the experiments was between $Re_h = 200$ and $Re_h = 1500$. According to Section 1.3.3 the flow is not laminar in this range of Reynolds numbers. Judging from the Reynolds number it can therefore be expected that the experiments lie in dispersion regime (V). The second option is to evaluate the slope of $D_L/(u_I d)$ as a function of the molecular Peclet number. In regime (IV), $D_L/(u_I d)$ is constant while in dispersion regime (V) it decreases with increasing molecular Peclet number. In my experiments I observed a decrease in $D_L/(u_I d)$ with increasing molecular Peclet number. Also this consideration suggests that the experiments lie in dispersion regime (V).

The decrease in $D_L/(u_I d)$ can be explained by the change in the mean velocity profile. Figure 4.12 shows velocity profiles inside the porous structure measured by PIV (see Section 6). The position where this profile was collected is shown in Fig. 6.3 (page 101). At this position, two regions can be identified. In the lower part, the velocity is about three times the interstitial velocity. This high velocity is the result of the constriction through which the fluid passed shortly before. It can be
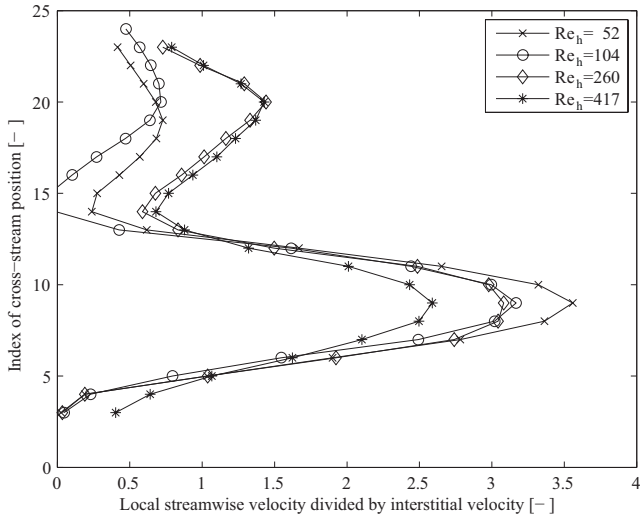
Figure 4.12: Radial profile of streamwise velocity in a porous structure. The axial position of the profiles is indicated in Fig. 6.3. At low hydraulic Reynolds numbers, the velocity variation over the cross-section is larger.

observed that the maximal (relative) velocity is lowest in the experiment with the highest Reynolds number. In the upper half of the cross-section the velocity is lower. There, the opposite is observed: the (relative) velocity is higher at higher Reynolds numbers. Therefore, the radial variation of velocity is lower at higher Reynolds numbers. This leads to less axial dispersion and therefore $D_L/(u_I d)$ decreases with increasing flowrate.

An additional observation in Fig. 4.11 is that the experimental values of the dispersion coefficient in the foam-like porous structure are higher than in packed beds of particles. Apart from the difference of the geometry, this is also caused by the difference in the definition of the characteristic diameter. Pfannkuch (1963) took the particle diameter as the characteristic length scale. For better comparability, the hydraulic diameter can be calculated from the particle diameter by Eq. (1.4). With the porosity of the packed bed of $40\,\%$, the hydraulic diameter is 2.25 times smaller than the particle diameter. This means that if Pfannkuch (1963) took the hydraulic diameter instead of the particle diameter, $D_L/(u_I d)$ would be a factor of 2.25 higher and Pe_m would be a factor of 2.25 lower. His data in Fig. 4.11 would therefore shift to the top left. Like this the agreement would be better, both in terms of absolute values as well as in terms of the limit between dispersion regimes (IV) and (V). This shows that the deviation between the observed dispersion coefficients in packed beds of spheres and in the foam-like porous structure is strongly affected by the choice of the characteristic diameter.

4.4 Conclusions

Radial mixing was investigated by the use of a wire-mesh sensor and by LIF. It was found that a wire-mesh sensor is a convenient measuring device for radial concentration profiles.

Wire-mesh sensors were then used for pulse experiments in a regular highly porous structure. The experiments were evaluated by fitting parameters of the dispersion model such, that the convolution of the inlet concentration profile with the residence time distribution fits the outlet concentration profile. It was found that this is a very convenient evaluation procedure. In contrast to the method with the Fourier trans-

formation, this method does not require any manual settings.

Measurements of axial dispersion were made at different positions but with equal length of the measurement section. This showed that in the entrance section, the dispersion coefficient is lower than further downstream. I discussed the entrance flow of a fluid into a porous structure. The build-up of the radial velocity profile and of the turbulence intensity is an effect that could produce a length dependence of the dispersion coefficient. This was the motivation for the study of the entrance length by particle image velocimetry. It was observed that the length of the entrance section is maximal 5 periodic units. This is rather short compared to the length of the measurement section in the dispersion experiments. It is therefore concluded that entrance effects play a role for dispersion, but that it is questionable wheter they are responsible for all differences observed between measurements in the entrance section and further downstream.

Finally, it was found that at hydraulic Reynolds numbers between $Re_h = 200$ and $Re_h = 1500$, turbulent dispersion is observed. Further, the decrease of $D_L/(u_I d)$ with increasing Pe_m was assigned to an equilibration of velocity extremes over the cross section of a pore.

Chapter 5

Optical measurements in porous structures [1]

Optical measurements were used to study the fluiddynamics in single-phase flow and two-phase flow. The results will be presented in Chapter 6 and Chapter 7. Here, I describe the measurement technique. First the literature about optical measurement techniques is reviewed. Then, the material properties of the solid and the two index-matched fluids are described. Next follows a description of the setup. Finally, the laser based measurement techniques particle image velocimetry (PIV) and laser-induced fluorescence (LIF) are described including a detailed description of the evaluation procedure.

5.1 Literature review

Many tomographic methods including X-ray radiography, neutron transmission tomography, nuclear magnetic resonance imaging, electrical capacitance tomography, and optical methods have been applied for visualizing the phase distribution (Chaouki et al., 1997). In the present study, an optical measurement technique is used with RI matching. Below, I review optical measurement techniques with a focus on studies that employed refractive index (RI) matching. I start with two-phase flows in

---

[1] Parts of this Chapter has been published in Häfeli R., Altheimer M., Butscher D., Rudolf von Rohr Ph., (2014). PIV study of flow through porous structure using refractive index matching. *Exp Fluids*, 55 : 1717; Häfeli R., Rüegg O., Altheimer M., Rudolf von Rohr Ph., Investigation of emulsification in static mixers by optical measurement techniques using refractive index matching. *submitted*

ducts, continue to single-phase flows in porous structures, and end with
two-phase flows in porous structures.

5.1.1 Two-phase flow in ducts

For phenomenological studies such as column flooding (Stemmet et al.,
2005) or phase inversion (Piela et al., 2006), a standard camera can be
used without RI matching. For quantitative measurements by LIF and
PIV a system consisting of an illuminating laser and a camera is needed.
When used for investigating multiphase flows, the main challenge faced
with these optical measurement techniques is the refraction of light at
phase boundaries. Some authors have applied optical measurement tech-
niques without RI matching (Unadkat et al., 2009; Lindken et al., 1999;
Fujiwara et al., 2004). In this case, a laser-based measurement technique
is frequently combined with shadowgraphy. The limitation of the shad-
owgraphy method is that it is only applicable to two-phase flows in a
bubbly flow regime with low hold-up of the dispersed phase. This lim-
itation can be overcome by matching the RI of the disperse phase and
the continuous phase.

RI matching was applied by Svensson and Rasmuson (2006) for two-
phase flow in stirred tanks. RI-matched two-phase flow through ducts
was investigated by LIF (Liu et al., 2005) and PIV (Conan et al., 2007).
Augier et al. (2003) applied simultaneous PIV and LIF measurements
in RI matched liquid/liquid flow through a duct. The images of the
particles and fluorescent dye were separated based on their gray values.
This allowed simultaneous PIV and LIF with only one camera. Similarly,
Morgan et al. (2013) investigated RI-matched liquid/liquid flow in a
duct. They simultaneously measured the droplet size by LIF and the
velocity field by PIV/PTV.

5.1.2 Single-phase flow in porous structures

RI matching between a solid and a liquid allows optical measurements
inside porous structures. Budwig (1994) reviewed RI matching tech-
niques for a single-phase flow. Wiederseiner et al. (2011) recently re-
viewed RI matching for particle suspensions. These two reports provide
an overview of fluid recipes corresponding solid materials for RI match-

ing. Whereas many studies have focused on RI matching between one fluid and one solid, few have focused on using RI matching for two-phase flow in porous structures.

5.1.3 Two-phase flow in porous structures

Ng et al. (1978) investigated liquid/liquid two-phase flow through a porous structure by RI matching of the wetting liquid and the solid. The motion of single droplets was observed by viewing the setup from two perpendicular directions. Kong et al. (2011) investigated gas/liquid two-phase flow inside a porous structure by RI matching of the continuous liquid phase and the solid. A moving laser sheet allowed an incremental 3D scan of the gas phase, in turn allowing a 3D reconstruction of the distribution of the gas phase.

Few studies have employed RI matching between two fluids and a solid. Burdett et al. (1981) was the first to match the RI of two fluids and a solid for optical measurements. Silicone rubber with $n = 1.422$ was used owing to its low RI. This allowed the use of methylcyclohexane and a 67.9 % w/w glycerine/water mixture. The mean hold-up along a line was estimated using a light absorption technique. Montemagno and Gray (1995) were the first to apply RI matching for investigating two-phase pore scale flow. Two aqueous and two nonaqueous liquids were used in a random packing of fused silica ($n = 1.46$). Tracer dyes were added to both phases. The aqueous phase was doped with a dye that congregates along the fluid-fluid interface. Plane illumination by a coherent laser enabled identification of the two phases. A 3D scan of the two fluids in the porous structures was obtained by using precision translators for the optical measurement equipment. Alternatively, Stöhr et al. (2003) measured the 3D field by the translation of the porous structure. They used silicone oil and a zinc chloride solution as RI matching fluids for fused silica. Two optical filters were mounted on a PC-controlled filter wheel to allow separate LIF measurements of the phases with one camera. Ovdat and Berkowitz (2006) obtained similar measurements from polymethyl methacrylate (PMMA). The phases were distinguished using a fluorescent dye in the disperse phase. Finally, Krummel et al. (2013) used two fluids that closely match the RI of glass beads to measure the 3D phase distribution. This was achieved using a

confocal microscope that (slice-by-slice) observed the fluorescence of a tracer in the wetting continuous liquid phase.

In comparison to the abovementioned studies that used particles with random packing, the porous structure investigated in this thesis has a defined geometry that is manufactured by rapid prototyping. This enables optical measurement techniques for one- and two-phase flow in designed porous structures.

5.2 Materials

5.2.1 The solid

For optical measurements, the porous structures are made of Somos$^{®}$ WaterShed XC 11122, in the following called WaterShed. It is a transparent material developed for the manufacturing with stereolithography. To enable optical measurements, two liquids with the same RI as WaterShed were used: anisole and a brine. They will be described in more detail in Section 5.2.2. First, the properties of WaterShed should be discussed.

The most important physical property of WaterShed for optical measurements is its RI. For the measurement of the RI, an Abbe refractometer from CarlZeiss AG was used. As the RI changes with temperature the measurement instrument was connected to a thermostat. There are two measurement principles, that both base on the measurement of the angle of total reflectance. Either, the angle can be measured in reflected light or in transmitted light. For the liquids the measurements were done in transmitted light whereas for the solid the measurement was done in reflected light. I measured the RI of WaterShed as being 1.519. According to the datasheet of the manufacturer, the RI of the WaterShed is between 1.512 and 1.515 (DSM, 2012). The reason for this deviation could be a result of the difference in manufacturing procedure or in measurement inaccuracy.

One problem observed during the experiments was that WaterShed absorbs water. After 1 month in still water a plate of WaterShed of 4 mm thickness is 1 % heavier due to absorbed water. It was found that this significantly increases the refractive index (RI). While the dry

Table 5.1: Properties of the two fluids (own measurements) (Häfeli et al., 2014).

	Anisole	Brine
Density [g/l]	990	1994
Viscosity [m^2/s]	1.56E-6	2.26E-6
RI @20 °C [-]	1.517	1.5195
Price per litre for 1 L [USD]	≈ 90	≈ 900
Price per litre for 10 L [USD]	≈ 70	≈ 400

structure has a refractive index of $n = 1.519$, a structure that absorbed water reaches a RI above $n = 1.53$. In order to prevent RI changes, WaterShed was cleaned every day with distilled water and then flushed with dry compressed air in order to allow drying and desorption. By control of the weight of the structure it was checked that no water was absorbed over time.

For the measurements with anisole, the structure had to be coated because it would be dissolved otherwise. For that, DS nuvovern (Mäder Aqualack AG, Switzerland), a varnish based on a polyurethane resin, was used. For the measurements with brine, no coating is required. From that perspective, the brine is the more convenient fluid.

5.2.2 The liquids

Two fluids that match the RI of WaterShed were used. The first is anisole, an organic liquid that was found by Butscher et al. (2012) to be suitable as fluid to match the RI of WaterShed. The second fluid is an aqueous solution of sodium iodide and zinc iodide. An overview of the properties is given in Table 5.1. The question might occur why a mixture of two salts is used instead of only one. The reason is that with sodium iodide alone the achievable RI near the solubility limit is $n = 1.5$ (Budwig, 1994). At increased temperatures the solubility is higher and theoretically a RI of $n = 1.519$ could be reached. This would however require tempering the whole setup at an elevated temperature. On the other hand, a solution of only zinc-iodide can reach a RI of up to $n = 1.62$
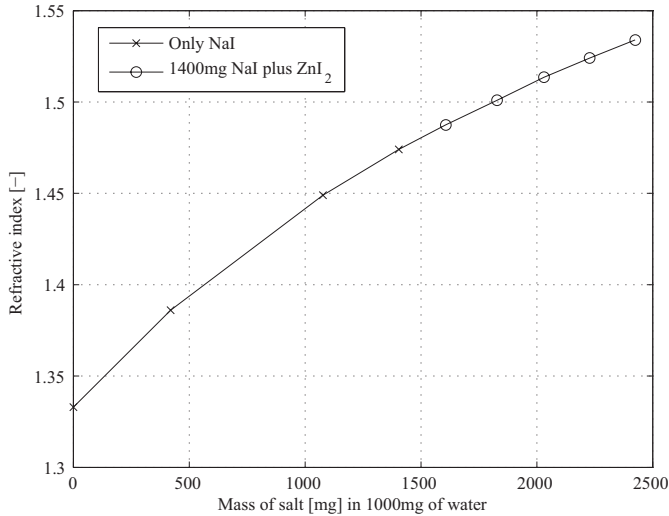
Figure 5.1: RI as a function of the composition of the brine.

due to its very high solubility in water (Budwig, 1994). However such a solution would lead to a liquid of high viscosity. Further the price of zinc iodide is rather high. Therefore I propose to use a mixture of both fluids: sodium iodide as a cheap material to increase the RI and zinc-iodide to further increase and match the RI to the one of the solid. The RI as a function of the composition is shown in Fig. 5.1. Starting with $1000 \, \mathrm{mg}$ of pure water with a RI of $n = 1.33$, the addition of NaI increases the RI and reaches $n = 1.47$ when $1400 \, \mathrm{mg}$ is added. To further increase the RI, zinc iodide is added. It was found that $730 \, \mathrm{mg}$ of zinc iodide is sufficient to reach $n = 1.519$.

In the two-phase flow experiments it was decided to match the RI to $n = 1.515$ according to the datasheet of the manufacturer (DSM, 2012). This can be achieved by adding $680 \, \mathrm{g}$ of zinc iodide. I have done this as I found that the measurements of the RI of the solid could contain some uncertainty due to the use of a contact liquid (Monobromonaphtalene)

in the Abbe refractometer. The Monobromonaphtalene can be absorbed by WaterShed, increasing its RI. Therefore, the real RI of WaterShed could be lower than the one that is measured.

The brine has several advantages over anisole. The WaterShed structure was found to be chemically stable in the brine. This is the main advantage over anisole which dissolves an uncoated structure rapidly. Even with a protective coating the structure decomposes after some time. Further the RI could be adjusted compared to anisole which is a pure substance with a fixed RI. A disadvantage of the brine is its discoloration over time. In contact with oxygen, the brine changes its color from transparent to yellow (Fig. 5.2). As I want to do optical measurements with a laser of wavelength 532 nm, I checked the absorption spectrum of the yellow (oxidized) brine. I found that the maximum absorbance is at lower wavelengths, i.e. around 350 nm (blue light is absorbed, therefore the solution appears yellow). At the wavelength of the laser the absorbance was negligible. This ensures that measurements can be made even if the solution is partly oxidized.

The yellow color is attributed to the formation of iodine by oxidation of zinc. In small samples this process was successfully prevented by inertizing the liquid with nitrogen. Even though initially I didn't flush the storage vessel with nitrogen, the discoloration was very slow. This was probably because of the low surface to volume ratio. Therefore I could work with the same liquid for a very long time i.e. for more than one year. If the discoloration occurs and an isolation from oxygen is not feasible, sodium thiosulfate ($Na_2S_2O_3$) can be used to reduce the iodine to iodide (Narrow et al., 2000). Important to note is that the effect on the physical properties of the fluid is very small. Neither density, viscosity nor RI changed by discoloration. I conclude from this observation that the amount of substance that was oxidized must be very small. Nonetheless, a nitrogen bottle was then connected to the experimental setup. It was found that by flushing it with nitrogen, oxydation can be prevented.

For the use in two-phase flow experiments, the two fluids have to fulfill some requirements in addition to the RI. The two fluids have to be immiscible, a fluorescent dye should be stable in the discontinuous phase and PIV particles should be dispersible in the continuous phase. It was found that Rhodamine B dissolves in anisole and is stable. As tracer for PIV I used 2 μm aluminum oxide particles that were dispersed
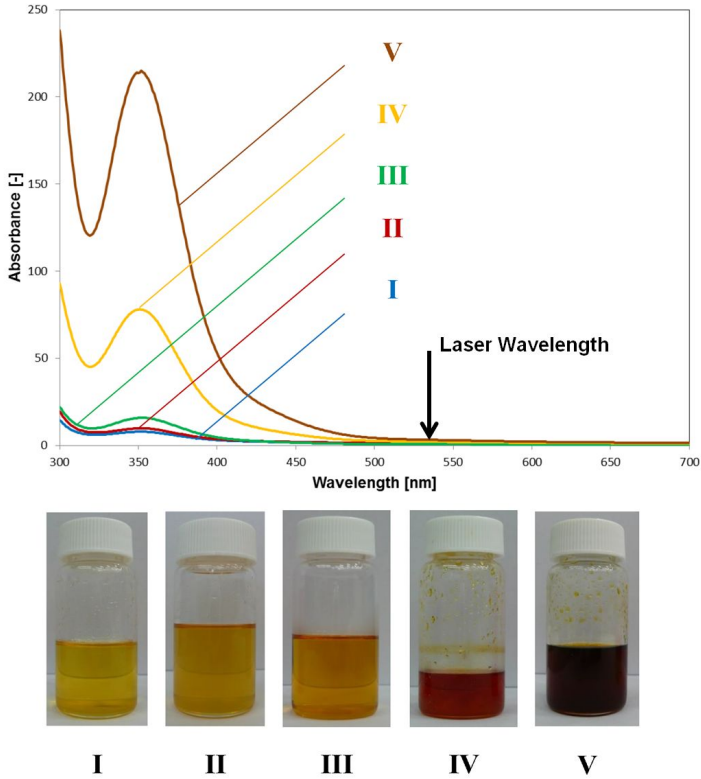
Figure 5.2: Light absorption spectrogram of brine with different extent of oxidation.

in the brine. To bring these particles to the brine they had to be mixed directly with the brine. What was not possible is to enter the particles in the two-phase separator where they first come in contact with the lighter anisole. If this is done, the particles accumulate at the phase boundary.

The simultaneous use of the two fluids brought some new problems as they are not completely inert. In the two-phase separator I observed the formation of a slurry. It must be formed from anisole as it is present only in that phase and collects near the liquid-liquid interphase in the two-phase separator. I did however not observe any change in density or RI.

The interface tension between two fluids strongly affects the two phase flow. A high interphase tension generally results in larger/ rounder droplets. The interface tension between a liquid and air is called surface tension. The surface tension is a property of the liquid while the interface tension depends on the properties of the two involved liquids. Water has a comparably high surface tension of $72\,\mathrm{mN\,m^{-1}}$. The surface tension of the brine was estimated as $55\,\mathrm{mN\,m^{-1}}$. For comparison, the brine was filtrated using a binder free glass microfiber filter (Whatman GF/C $1.2\,\mathrm{\mu m}$). The surface tension of this filtrated brine was measured as $56\,\mathrm{mN\,m^{-1}}$. I conclude that the filtering did not affect the surface tension. An important step in the measurement of the surface tension is the separation of brine from anisole. This should be described in more detail. One possibility is to take a sample of brine from the two phase separator in the setup (① in Fig. 5.3). As the anisole is the lighter phase that is on top of the brine, some anisole will always be entrained. In the measurement of the surface tension, this small amount of anisole collects at the surface, where it acts as a surfactant. The RI measured like this is therefore considerably smaller and unreproducible. Therefore, a larger sample containing both anisole and brine is taken from the two-phase separator. The two fluids are then separated using a separatory funnel from which the brine can be drawn from below. Like this it is ensured that no anisole contaminates the brine during the surface tension measurements. The interfacial tension between the brine and anisole was found to be smaller than the surface tension of the brine. The reason can be found in the attraction between molecules of the two liquids. I measured a value of $9.64\,\mathrm{mN\,m^{-1}}$. For this measurement, the fluids were filtered and then separated by a separatory funnel. The surface and in-

terface tension measurements described above were made with a K100 tensiometer by Krüss using the Wilhelmy plate method.

5.3 Experimental setup

5.3.1 Pumps and valves

Due to the relatively high price of the liquids a closed system was built (Fig. 5.3). The liquid-liquid separator is a simple glass vessel with a volume of 2.5 L. The heavier brine is collected at the bottom of the vessel whereas the lighter anisole is collected at the top. Two gear pumps (VGS200 from Verder Catag) are used to convey the liquids. The flowrate is controlled by a massflow controller that works based on the coriolis principle (Bronckhorst M55-AGD-22-O-S). The massflow controllers measure the flowrate with an accuracy of 0.2%. Additionally, they measure density and temperature. A thermostat is used to remove the heat from the pumps and bring the system to a constant temperature of 20 °C. The brine then enters an empty pipe with an inner diameter of 20 mm and a length of 100 mm. After this section and right in front of the porous structure the anisole is injected through a nozzle with a diameter of 1 mm. After the measurement section the fluids are guided back to the two-phase separator.

The choice of materials that are compatible with anisole and the brine is somehow limited. The piping and fittings are made out of stainless steel and polyamide. The plant further comprises some sealings. In a first attempt I used nitrile butadiene rubber (NBR) sealing rings. These are chemically resistant to both fluids but they swell in anisole. This brought some problems when dismantling the plant and the sealing rings had to be replaced from time to time. In the end it was found to be worth investing in more expensive perfluoroelastomer (FFKM) sealing rings. These proved to be chemically resistant to both fluids.

5.3.2 Laser and cameras

The setup is configured for simultaneous PIV and LIF measurements. Fig. 5.4 shows the arrangement of laser, measurement section and cameras. A pulsed Nd-YAG laser with a wavelength of 532 nm is used (Litron
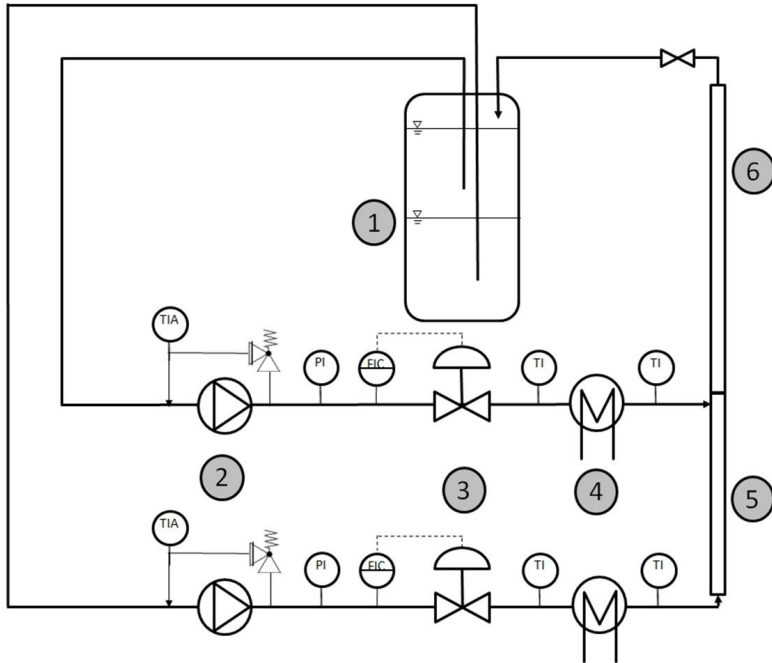
Figure 5.3: Experimental setup. Fluids are stored in a liquid-liquid
separator ①. From there they are sucked by two gear
pumps ②. The flowrate is controlled by massflow con-
trollers ③. After tempering ④, the brine enters a calming
section ⑤. The anisole is injected via a nozzle right in front
of the porous structure ⑥. Several positions are equiped
with temperature (T), pressure (P) and flowrate (F) indi-
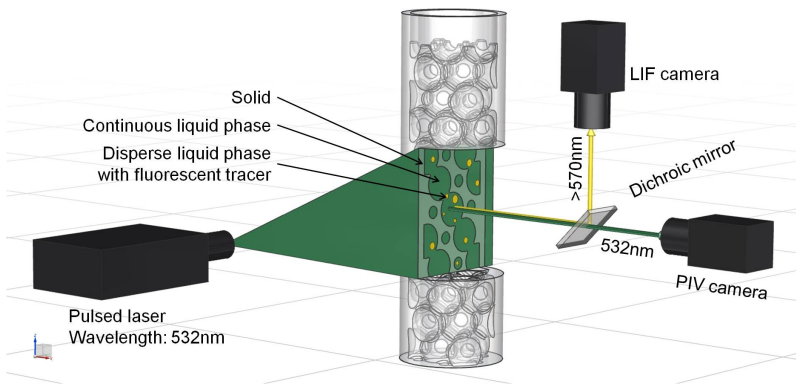cators (I), controllers (C) and alarms (A).

Figure 5.4: Illustration of the measurement equipment. A green laser illuminates a plane in the porous structure. The laser light is reflected by PIV particles (green) and excites the fluorescent tracer dye (orange). The light from the two sources is separated by a dichroic mirror and recorded by two cameras equipped with filters.

Nano L 135-15). The laser has a pulse energy of 120 mJ and a frequency of 15 Hz. A set of cylindrical lenses expands the laser beam to a sheet of 100 µm in thickness. The light is then reflected by PIV particles in the continuous phase and it excites the fluorescent dye in the disperse phase. The reflected light from PIV particles has the same wavelength as the laser (532 nm). The light emitted by the fluorescent dye has a higher wavelength (> 570 nm). This allows to separate the two images by a dichroic mirror. In addition to that I mounted filters on the two camera lenses. The images are recorded by a CCD camera with a resolution of 1600×1200 pixels and 14bit dynamic range (PCO1600). A BNC575 timing unit is used for the synchronization. The software for control and evaluation of measurements is Dantec DynamicStudio v3.31.

5.3.3 Measurement plane

Figure 5.5 shows an auxiliary view of one periodic unit of the porous structure (left) and a top view on the measurement plane (right). The measurements were made in a plane through the center of the tube. From the total of twelve pores per cell only two are in the measurement plane. As a consequence there is only one entrance and one exit visible in the PIV images.

In the Sulzer SMX$^{\text{TM}}$ static mixer, it is not possible to place the measurement plane centered in the tube. The problem is that one face of the ligaments lies in the centered plane. When a solid-fluid interface lies in the plane of the laser, there are strong effects of refraction. The reason is that due to the surface roughness, the light crosses the interface several times. I can therefore be strongly deviated even if the RI matching is very good. Therefore the measurement plane in the Sulzer SMX$^{\text{TM}}$ static mixer was chosen 2 mm off-centered. Like this the measurement plane is exactly between two ligaments (Fig. 5.6).

5.4 PIV measurements

5.4.1 Evaluation procedure

For the evaluation of the images the mean image was calculated from a series of measurements. The mean image was then subtracted from each
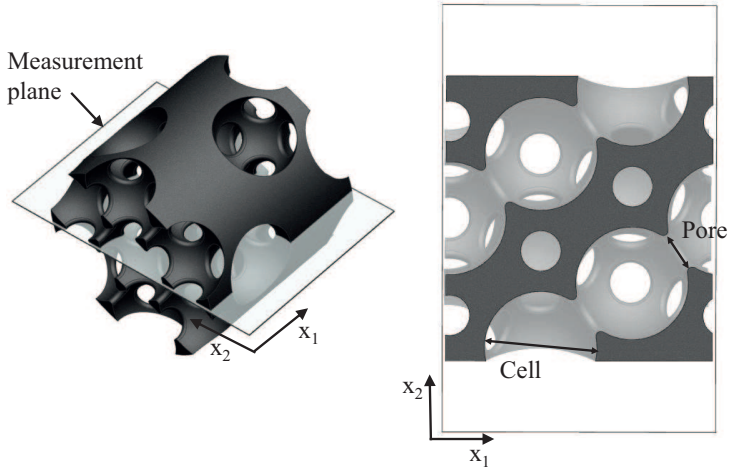
Figure 5.5: One periodic unit of the porous structure (Häfeli et al., 2014). Fluid flow in axial direction x_1. Left: auxiliary view, right: cut at measurement plane.
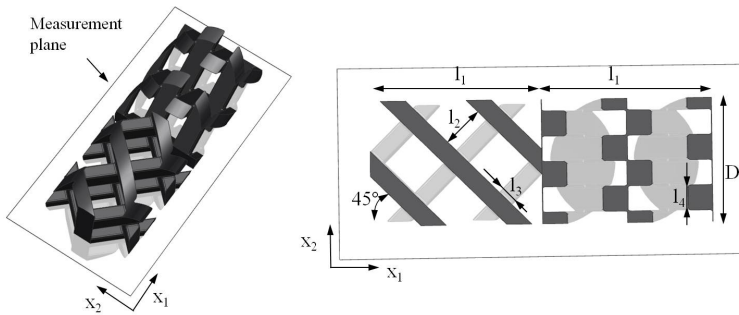

Figure 5.6: Four periodic units of a SulzerSMX^{TM} static mixer. Left: auxiliary view, right: cut at measurement plane.

image in order to eliminate perturbations from the background. It was observed that not all tracer particles had the same brightness, probably due to differences in size and surface properties. To ensure that all particles have the same weight in the cross correlation, the image could have been converted to black-white. This would however have imposed problems in sub-pixel interpolation and therefore peak-locking would be observed. The alternative is to clamp the image such that bright and dark particles have the same weight. Both background subtraction and clamping was done by a built-in function in the commercial software DynamicStudio from Dantec. Figure 5.7 shows an image after background subtraction and clamping. The interrogation area size for the cross-correlation was 64×64 pixel for the measurements in the 20 mm structure and 32×32 pixel for the measurements in the 7 mm structure. In any case, a 50% overlap of interrogation areas was used. With these settings the resolutions were $\Delta_{20mm} =$268 µm and $\Delta_{7mm} =$152 µm. The resulting velocity vector field had to be postprocessed to remove spurious vectors. This was done by a moving average validation. The procedure compares each vector to the vectors in its surrounding, in my case a region of 3×3 vectors. If the deviation exceeded an acceptance threshold the vector was replaced by the average of its surrounding vectors as a reasonable estimate of the true velocity.

5.4.2 PIV particles

Different seeding particles were evaluated. It was found that glass beads and polyamide particles cannot be dispersed in the brine. Due to their low density they float on the surface of the liquid. I therefore chose particles of higher density and found aluminum oxide to be suitable. The aluminum oxide seeding particles had a mean diameter of 2 µm. This is rather small compared to other PIV studies in liquid flows (Melling, 1997). An advantage of small seeding particles is their better flow tracking capability. Another rule for the selection of seeding particle size is that they should cover more than one pixel on the image, preferably around 2.5 pixels in order to prevent peak-locking. Even though the pixel size on the image was 8 µm, the scattered light from 2 µm particles illuminated an area of ≈ 2.5 pixels. It is therefore considered as a suitable particle size both from flow tracking capability and image quality.
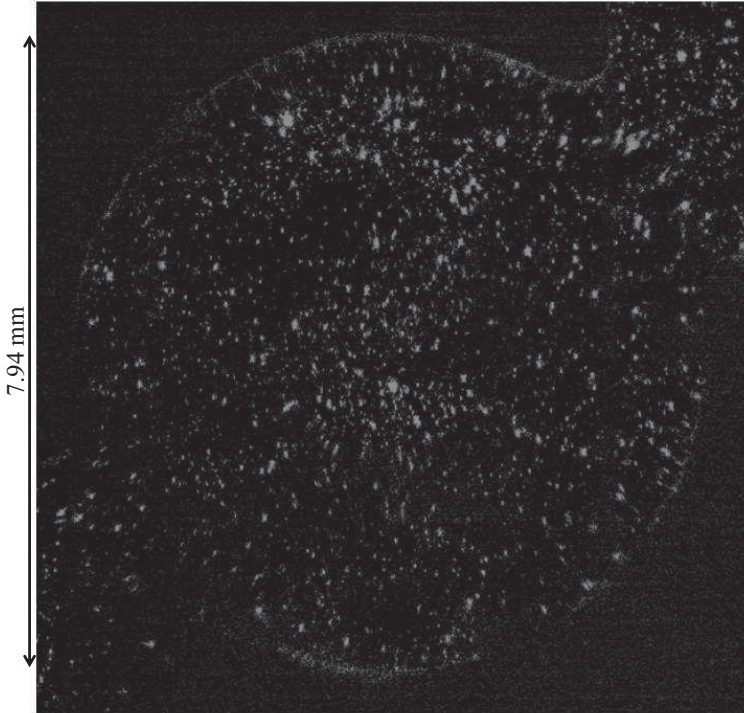
Figure 5.7: Image of PIV particles inside a cell of the porous structure after subtraction of mean image and gray value clamping. The image is of a measurement with the large diameter, i.e. with a cell size of 7.94 mm (Häfeli et al., 2014)

5.4.3 Sample size

The sample size for experimental work must be known a priori. Too small sample sizes results in large statistical uncertainty. With too large sample sizes, time and effort is wasted without increasing the accuracy. In order to find the appropriate sample size delivering a statistically meaningful result I applied bootstrapping. Bootstrapping is a resampling technique that allows to estimate statistical quantities from a set of measurements (Efron, 1979). For this a series was recorded consisting of 10000 measurements. Then, a sample of n values was drawn out of these 10000. From these n values the average was calculated. Repeating this procedure B times, the standard deviation of the B mean values was calculated. It was found that for a sample size $n > 500$ the statistical deviation of the result (turbulent kinetic energy) does not decrease significantly. With a sample size of 500 the statistical uncertainty is below 0.5 % and no time or effort is wasted. The same procedure for the dissipation rate suggests that for a sample size of $n = 500$ the statistical uncertainty is below 5.2 %.

5.5 LIF measurements

5.5.1 Evaluation procedure

The procedure to evaluate the LIF images started with background subtraction and masking of the solid region. The image was then converted to a black/white image (b/w). To find the right threshold, the gray-value histogram of the image was analyzed. An intensity peak was found at a gray value corresponding to the background. The peak of the histogram plus two times its standard deviation was then set as the initial threshold. After this step, all droplets that contain less than 65 pixels are rejected. This corresponded to droplets with a diameter of 88 µm. Dark spots inside the droplets were then closed. A disadvantage of this step is that if there are brine droplets inside anisole droplets, this area is falsely attributed as anisole. This has to be kept in mind when images with many droplets in droplets are analyzed. The number of pixels in a droplet multiplied by the area of one pixel gave the cross-sectional area of the droplet. This was used to define the characteristic diameter of

the droplet. The characteristic diameter of a droplet was defined as the diameter of a circle with equal cross section. The effect of observing a sectional plane of the droplet instead of the real droplet diameter will be discussed in Section 5.5.2.

Some droplets were so close to each other that they were recognized as a single droplet. I therefore developed a postprocessing procedure that can identify sticking droplets. I found that the center of a droplet is brighter than its border. This causes droplets to be smaller when the b/w threshold is higher. I therefore developed a procedure that is based on incrementally increasing the b/w threshold. When two droplets sticked together in the b/w image with a low threshold, they were separated at a certain higher threshold. If the two new droplets were more round than the original, they were defined as two droplets; however, if they were less round, it was assumed that the original was the real droplet. The reason for this distinction was that the laser sheet was not completely homogeneous, but contained some darker stripes. Figure 5.8 shows the change in b/w images for droplets that are very near (top) and a droplet that is inhomogeneously illuminated (bottom). In the images on top, three droplets are very close to each other. In a b/w image with low threshold (top,center), the three droplets are recognized as a single droplet. However, in an image with higher threshold (top,right), the three droplets are separated. The bottom of Fig. 5.8 shows a droplet that is in a region of inhomogeneous laser illumination. With a low b/w threshold, the droplet is recognized correctly. However, at higher threshold, the droplet appears as three non-round regions. Such droplets are identified correctly using the above-described procedure.

This post-processing is quite simple compared to other measurement techniques. In shadowgraphy, for example, one observes overlapping bubbles and bubbles that are out-of-focus. Lelouvetel et al. (2011) distinguished focused bubbles from unfocused ones by filtering the gradient of the gray value at the boundary of the bubble. Bröder and Sommerfeld (2007) used a Sobel filter to identify the bubble contours and then used the gray value gradient to identify unfocused bubbles. Honkanen et al. (2005) have shown an algorithm that identifies strongly overlapping bubbles by fitting ellipses on the clustered arcs of the perimeter of bubbles. As I applied plane illumination, I did not observe unfocused droplets, and could use a relatively simple detection method.
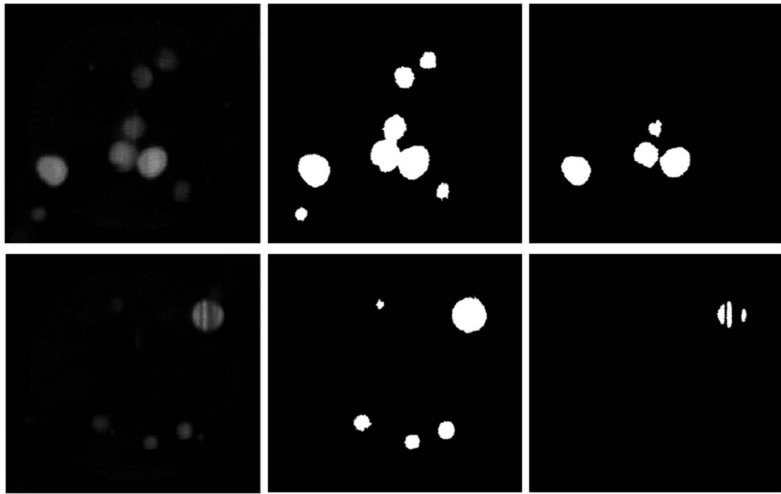
Figure 5.8: Influence of changing threshold for sticking bubbles (top) and bubbles in a laser sheet with stripes (bottom). The left shows a grayscale image, the middle shows a b/w image with a low threshold, and the right shows a b/w image with a higher threshold.

5.5.2 Error sources

Effect of dichroic mirror

A dichroic mirror was used to separate the PIV and the LIF image. It was found that the light reflected by the mirror is blurred. Figure 5.9 shows an image (of droplets inside a cell) obtained without a dichroic mirror. For comparison, Fig. 5.10 shows an image of the light reflected by the dichroic mirror. In a direct comparison of measurements obtained
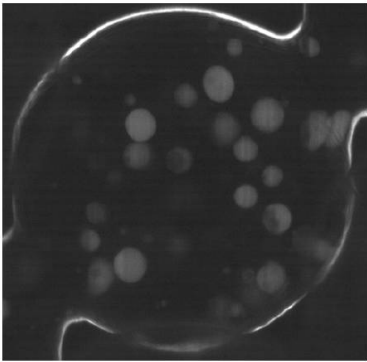

Figure 5.9: LIF image obtained without a dichroic mirror.
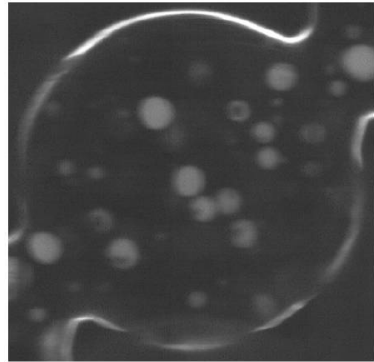
Figure 5.10: LIF image obtained with a dichroic mirror.

with and without the mirror, I found that the droplet size is 9.3 % larger when a mirror is used. It could therefore be argued that it is better to not use a mirror. However, I found that the evaluation of the images is more difficult when no mirror is used because the droplet images can show many fine stripes from inhomogeneous laser illumination. This makes it difficult to correctly identify the droplets. Therefore, the dichroic mirror was used for the LIF measurements even when no PIV measurements were performed simultaneously.

Figure 5.11: Measured droplet size on image as a function of its po-
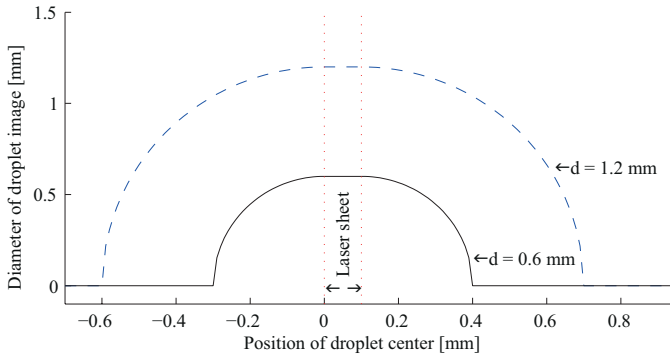sition relative to the laser sheet. A small droplet $d =$
$0.6\,\text{mm}$ and a large droplet $d = 1.2\,\text{mm}$ are shown.

Error due to plane-illumination

As plane-illumination was applied, a slice of the droplet is observed. The
measured droplet diameter was therefore smaller than the real diameter.
In the following, I estimate the error due to plane-illumination. For
the calculation, spherical droplets were assumed. Figure 5.11 shows the
measured droplet size as a function of the droplet position relative to
the laser sheet. The laser sheet is located between $0\,\text{mm}$ and $0.1\,\text{mm}$ on
the x-axis. A droplet with a diameter of $0.6\,\text{mm}$ is not visible when its
center is at a position $x < -0.3\,\text{mm}$. When the center of the droplet is in
the laser sheet, the largest diameter of the droplet is illuminated and the
correct droplet size is measured. When the center is between $-0.3\,\text{mm}$
and $0\,\text{mm}$, a slice of the droplet is illuminated. It is assumed that the
largest illuminated diameter of that slice is observed in the image. In
this case, the observed diameter as a function of the position is between
$0\,\text{mm}$ and the actual size when the droplet travels from $-0.3\,\text{mm}$ to $0\,\text{mm}$
on the x-axis.

Averaged over all positions, the measured droplet size is slightly lesser
than the actual droplet size. The relative error depends on the droplet
size and the thickness of the laser sheet. In my experiments, the laser

sheet had a thickness of 100 µm. Based on the calculation above, a droplet with a diameter of 0.6 mm is measured as being 0.49 mm across. A droplet with a diameter of 1.2 mm is measured as being 0.96 mm across. The ratio between the measured and the real droplet size is 81.5% for the small droplet and 80.1 % for the large droplet. If the laser sheet were infinitesimally thin, the measured diameter would be $\frac{\pi}{4} = 78.5\,\%$ of the real diameter. The maximal error due to plane illumination is therefore $-21.5\,\%$. One could conclude that a thick laser sheet is beneficial for the measurement of the droplet size. However, if the laser sheet is too thick, overlapping droplet images are observed. This makes it difficult to identify single droplets in the images. A thin laser sheet is therefore preferred.

Chapter 6

Microscopic study of mass transfer[1]

In Chapter 3 and Chapter 4, the transport of a scalar was investigated by macroscopic studies. In both cases, the domain of observation was much larger than the size of the pores. Here, I will show experiments of scalar transport on the microscopic scale of the pores. The measurements were made by particle image velocimetry as described in Chapter 5.

First, I discuss the entry region length in flow through a porous structure. Then, I show how scalar transport can be estimated from particle image velocimetry measurements. Next, the scaling laws necessary to compare experiments with different fluids and dimensions are introduced. Finally, the results of turbulent kinetic energy, dissipation rate and turbulent diffusivity measurements are presented.

6.1 Entry-region length

6.1.1 Literature

When a flow through an empty pipe enters a porous structure, the flow quantities change. For example, the turbulent kinetic energy changes from a value characteristic for the empty pipe to a value characteristic for the porous structure. Figure 6.1 illustrates the evolution of turbulence intensity when an empty pipe flow enters a porous structure.

---

[1]Parts of this Chapter has been published in Häfeli R., Altheimer M., Butscher D., Rudolf von Rohr Ph., (2014). PIV study of flow through porous structure using refractive index matching. *Exp Fluids*, 55 : 1717.
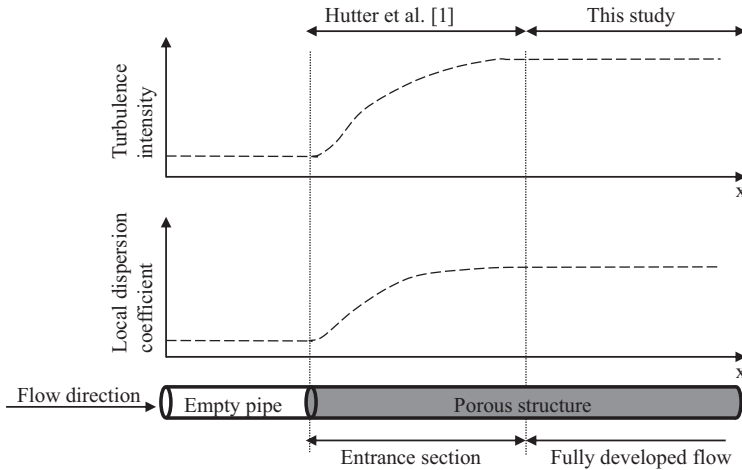
Figure 6.1: Build-up of turbulence intensity and local dispersion coefficient in the entrance section of a porous structure (qualitative illustration).

Similarly, other quantities of the flow gradually change, including the local dispersion coefficient. After a certain length, the flow quantities will not change anymore. This region is refered to as fully developed flow. The length it takes until the flow is fully developed is referred to as *entrance length*. In the following, I review literature about the entrance length in pipes and in porous structures.

In pipes, developing turbulent flow is a transition from a boundary layer type flow at the entrance to a fully developed flow downstream (Kumara et al., 2010). In turbulent flow the entrance section contains six flow regimes, for which theoretical models were developed (Salami, 1986). Despite the identification of flow regimes many researchers investigated the length that it takes for the flow to be fully developed. This knowledge is of great importance for the design of rigs for internal flow investigations. Barbin and Jones (1963) observed that developed turbulent flow is not attained in a pipe length corresponding to 40 di-

ameters. Weir et al. (1974) stated that for developed flow it takes longer than usually assumed, in their case more than 70 diameters. Further, they observed that the entrance length depends on inlet flow conditions. Recent studies presented numerical treatments of the entrance flow. Kumara et al. (2010) found that in laminar flow, after 31.78 diameters the centerline velocity reaches 99 % of its final value, what they defined as fully developed. In the turbulent case they found that, after an overshoot of centerline velocity at about 30 diameters, developed turbulent flow is attained at about 65 diameters.

Similar studies in porous structures are rare. While the entrance flow in a pipe is expected to share some characteristics with entrance flow in a porous structure, there are also considerable differences, e.g., the periodic acceleration and deceleration of the flow in porous structures. Mokrani et al. (2009) investigated the flow over vortex generators mounted in a pipe. Mean and statistic quantities of the flow were measured using laser Doppler velocimetry. They found that after four rows of vortex generators the flow reaches a steady periodic regime. Horneber et al. (2012) made a numerical simulation of the flow through a row of 8 units of a Kelvin cell. It was observed that fully developed flow, when judging from the development of mean velocity, is reached after very few cells. Butscher et al. (2012) experimentally investigated the entrance length in a porous structure. They used particle image velocimetry with RI matching between the solid and the fluid. In the resolved length scales the flow was developed after about two periodic units. Dukhan and Suleiman (2014) investigated the entrance length by pressure drop measurements and simulations. They found that the entrance length in a porous structure is a function of the Reynolds number. At high flowrates the entrance length appeared to reach a fixed value of six cells.

These studies imply that in porous structures the length until the flow is fully developed is much shorter (less than 10 cells) than in pipe flow (more than 50 diameters).

6.1.2 Experiments

In this thesis, the length of the entrance section was investigated by particle image velocimetry. Figure 6.2 shows the evolution of the velocity fluctuation as a function of the position in the porous structure. A
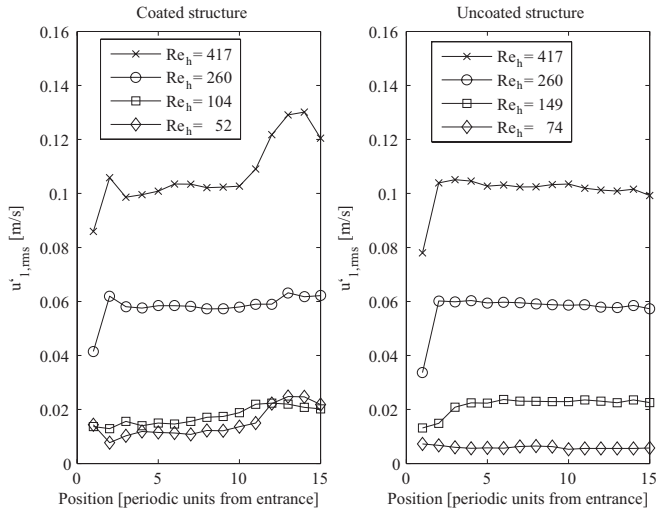
Figure 6.2: Root mean square velocity fluctuation as a function of position in the porous structure. Comparison between an coated structure (left) and an uncoated structure (right).

constant velocity fluctuation is observed over a wide range of positions in the porous structure. Only near the inlet to the porous structure did I observe different (mostly lower) levels of velocity fluctuations. Further, it was observed that in a coated porous structure (left hand side of Fig. 6.2) the root mean square velocity fluctuation increases. The reason why experiments were made in a coated structure is that anisole dissolves an uncoated structure. To investigate the effect of the coating, experiments with the brine were made in the coated and in the uncoated structure. It was observed that varnish tears formed near the end of the coated structure (periodic units 11 to 15). As a consequence of that, an increase in velocity fluctuation was observed starting in the eleventh periodic unit. In the pores where there are no varnish tears, i.e. up to the tenth periodic unit, a good agreement between the coated and the uncoated structure was observed.

In the first periodic unit the velocity fluctuation was usually lower than further downstream. The reason is that the flow upstream of the porous structure was a laminar pipe flow. When the fluid then entered the porous structure, velocity fluctuations were induced. I observed that after very few periodic units the velocity fluctuation reached a constant value. Due to the uncertainty of the measurement, an exact value of the entrance length cannot be evaluated. However, it can be stated that after two to five periodic units the velocity fluctuation did not change significantly. This length corresponds to roughly three to fifteen times the hydraulic diameter.

6.2 Scalar transport modeling

In Section 1.4, it was discussed how *macroscopic* conservation equations can be used to model heat and mass transport in porous structures. Here, I will investigate turbulent mass transport on the *microscopic* scale of the pores by means of particle image velocimetry.

Various models exist that relate the turbulent heat and mass transport to certain characteristics of a turbulent flow. One of them is the standard k-ε model developed by Jones and Launder (1972) and slightly modified by Launder and Sharma (1974). This model gives the turbulent

diffusivity as:

$$\Gamma_T = \frac{\nu_T}{Pr_T} \left[m^2/s \right] \tag{6.1}$$

where ν_T is the turbulent viscosity and $Pr_T = 0.9$ the turbulent Prandtl number. The turbulent viscosity is estimated as:

$$\nu_T = C_\mu k^2/\varepsilon \tag{6.2}$$

where $C_\mu = 0.09$ is one of the five model constants, k is the turbulent kinetic energy and ε is the dissipation rate of turbulent kinetic energy. In this thesis, k and ε were measured by means of particle image velocimetry (PIV). Combining Eq. (6.1) and Eq. (6.2) the turbulent diffusivity can be calculated as:

$$\Gamma_T = \frac{C_\mu \cdot k^2}{Pr_T \cdot \varepsilon} \tag{6.3}$$

The velocity fluctuations used for the determination of the turbulent kinetic energy are obtained by Reynolds decomposition of the velocity vector:

$$u_i = \overline{u_i} + u_i' \tag{6.4}$$

where u_i [m/s]: measured velocity, $\overline{u_i}$ [m/s]: mean velocity and u_i' [m/s]: velocity fluctuation in direction x_i.

From the velocity fluctuation in all three dimensions the turbulent kinetic energy is calculated as follows:

$$k = \frac{1}{2} \cdot \overline{u_i' u_i'} = \frac{1}{2} \cdot \left(\overline{u_1' u_1'} + \overline{u_2' u_2'} + \overline{u_3' u_3'} \right) \tag{6.5}$$

With 2D PIV measurements, only two components of the velocity field are measured. I therefore have to make assumptions to calculate the turbulent kinetic energy. A discussion of this can be found in Section 6.4.1.

The dissipation rate for a fluid with viscosity ν is defined as:

$$\varepsilon = \frac{1}{2}\nu \overline{\left(\frac{\partial u_i'}{\partial x_j} + \frac{\partial u'_j}{\partial x_i} \right)^2} \tag{6.6}$$

This equation can be expanded leading to:

$$\varepsilon = \nu \left\{ \begin{array}{l} 2\left(\overline{\left(\frac{\partial u_1'}{\partial x_1}\right)^2} + \overline{\left(\frac{\partial u_2'}{\partial x_2}\right)^2} + \overline{\left(\frac{\partial u_3'}{\partial x_3}\right)^2}\right) + \overline{\left(\frac{\partial u_1'}{\partial x_2}\right)^2} \\ +\overline{\left(\frac{\partial u_2'}{\partial x_1}\right)^2} + \overline{\left(\frac{\partial u_1'}{\partial x_3}\right)^2} + \overline{\left(\frac{\partial u_3'}{\partial x_1}\right)^2} + \overline{\left(\frac{\partial u_2'}{\partial x_3}\right)^2} + \overline{\left(\frac{\partial u_3'}{\partial x_2}\right)^2} \\ +2\left(\overline{\frac{\partial u_1'}{\partial x_2}\frac{\partial u_2'}{\partial x_1}} + \overline{\frac{\partial u_1'}{\partial x_3}\frac{\partial u_3'}{\partial x_1}} + \overline{\frac{\partial u_2'}{\partial x_3}\frac{\partial u_3'}{\partial x_2}}\right) \end{array} \right\} \quad (6.7)$$

The terms containing u_3 or x_3 are not measured by 2D PIV. Instead, the unknown terms need to be estimated from the known terms by proper assumptions. If homogeneous and isotropic turbulence is assumed, the dissipation rate can be simply calculated from one gradient (de Jong et al., 2009):

$$\varepsilon = 15\nu \overline{\left(\frac{\partial u_1'}{\partial x_1}\right)^2} \quad (6.8)$$

There are various models available that lie between Eq. (6.7) and Eq. (6.8) depending on the assumptions made. Depending on the flow situation, axisymmetry (George and Hussein, 2003) or isotropy (Sharp and Adrian, 2001) can be assumed. Further the mixed derivative moments can be transformed by using the incompressible continuity equation (George and Hussein, 2003). Finally some authors used the continuity equation to estimate the cross product gradients (Doron et al., 2001).

Delafosse et al. (2011) investigated the flow in a stirred tank by PIV. They observed that the isotropy ratios, defined as ratios between squared gradients and cross-product gradients, are not all equal to unity. Based on that a formula for ε was proposed:

$$\varepsilon = \nu \left\{ \begin{array}{l} 3\overline{\left(\frac{\partial u'_1}{\partial x_1}\right)^2} + 3\overline{\left(\frac{\partial u'_2}{\partial x_2}\right)^2} + 3\overline{\left(\frac{\partial u'_1}{\partial x_2}\right)^2} + 3\overline{\left(\frac{\partial u'_2}{\partial x_1}\right)^2} \\ +6\overline{\left(\frac{\partial u'_1}{\partial x_2}\frac{\partial u'_2}{\partial x_1}\right)} \end{array} \right\} \quad (6.9)$$

Much more sensitive than the choice of the right model is the requirement to have an appropriate spatial resolution of the measurements. As the dissipation occurs at the smallest scales of motion, i.e. at the Kolmogorov scale, the measurement should resolve even these motions. It was observed in several studies that the error can be high when the resolution is insufficient. For example, Saarenrinne et al. (2001) observed

that if the resolution is around $2l_K$ the estimated dissipation rate is 90 %
of the true value. If the resolution is $9l_K$ the measured value corresponds
to 65 % of the true value. Baldi and Yianneskis (2003) observed that dou-
bling (improving) the spatial resolution leads to a 250 % increase of the
dissipation rate. Delafosse et al. (2011) observed that doubling the spa-
tial resolution the estimated dissipation rate increased by 220 %. Also in
the experiments presented here, the Kolmogorov scale was not resolved,
as will be discussed in Section 6.4.2. Therefore, the estimated value of
the dissipation rate of turbulent kinetic energy has to be considered as
underestimated.

6.3 Scaling laws

Scaling laws are applied in order to compare experiments with anisole
and the brine as well as experiments in ducts of 7 mm and 20 mm diam-
eter. In wind-tunnel experiments it is common to adjust size, viscosity
and velocity in a way that makes the experiment realizable in a wind-
tunnel but keeping the Reynolds number constant:

$$\frac{u_o D_o}{\nu_o} = Re_o = Re_m = \frac{u_m D_m}{\nu_m} \qquad (6.10)$$

Here, o indicates the original experiment with original size, velocity, and
viscosity and m the experiment with the model settings. When the
size of the object under investigation is changed this has to be done
uniformly in all three dimensions, i.e. geometric similarity has to be
given. If two objects are geometrically similar and experiments are done
at equal Reynolds number then kinematic similarity holds. This means
that ratios between corresponding velocities are equal in the original and
in the model experiment, for example:

$$\left.\frac{u'_{rms}}{\overline{u}}\right|_o = \left.\frac{u'_{rms}}{\overline{u}}\right|_m \qquad (6.11)$$

With the help of this, the ratio of the turbulent kinetic energy can be
calculated from the ratio of the mean velocity:

$$\frac{k_m}{k_o} = \frac{\overline{u'u'}\big|_m}{\overline{u'u'}\big|_o} = \frac{\overline{u_m u_m}}{\overline{u_o u_o}} \qquad (6.12)$$

In the experiments the diameter and the viscosity is given a priori. In a series of measurements the velocity is then varied. I therefore like to have a scaling law that bases on a priori known and constant variables, i.e. ν and D. Combining Eq. (6.10) and Eq. (6.12) leads to:

$$\frac{k_m}{k_o} = \frac{\nu_m^2 D_o^2}{\nu_o^2 D_m^2} \tag{6.13}$$

or:

$$k \propto \frac{\nu^2}{D^2} \tag{6.14}$$

The same procedure is applied to scale the values of the dissipation rate:

$$\frac{\varepsilon_m}{\varepsilon_o} = \frac{\frac{1}{2}\nu \overline{\left(\frac{\partial u_i'}{\partial x_j} + \frac{\partial u'_j}{\partial x_i}\right)^2}\bigg|_m}{\frac{1}{2}\nu \overline{\left(\frac{\partial u_i'}{\partial x_j} + \frac{\partial u'_j}{\partial x_i}\right)^2}\bigg|_o} = \frac{\nu_m \left(\frac{\overline{u_m}}{D_m}\right)^2}{\nu_o \left(\frac{u_o}{D_o}\right)^2} \tag{6.15}$$

If we again replace u by employing that $Re_o = Re_m$ we obtain a scaling law that is only depending on a-priori known variables:

$$\varepsilon \propto \frac{\nu^3}{D^4} \tag{6.16}$$

Finally, the scaling law of the turbulent diffusivity is given as follows:

$$\frac{\Gamma_{T,m}}{\Gamma_{T,o}} = \frac{k_m^2/\varepsilon_m}{k_o^2/\varepsilon_o} = \frac{\nu_m}{\nu_o} \tag{6.17}$$

or simply:

$$\Gamma_T \propto \nu \tag{6.18}$$

I define that the original experiment is the one with brine in a structure with a diameter of $20\,\text{mm}$ and the other experiments are model experiments that are scaled to the values of the original. Table 6.1 shows the numerical values of the scaling factors.

Table 6.1: Scaling factors for the experiments with anisole and in the small structure. The experiment with salt in the large structure remains unscaled.

	k	ε	Γ_T
Large structure with saltwater (reference)	1	1	1
Large structure with anisole	0.4876	0.329	0.69
Small structure with saltwater	8.163	66.64	1

6.4 Results and Discussion

I first discuss the results on turbulent kinetic energy and dissipation rate of turbulent kinetic energy. After the evaluation of the necessary assumptions I show local distributions and compare the results by means of Reynolds similarity. In the end I then discuss scalar transport mechanisms in flow through porous structures by analyzing the turbulent diffusivity.

6.4.1 Turbulent kinetic energy

The following experiments were made in the tenth periodic unit from the entrance to the porous structure. According to Section 6.1, fully developed flow is expected at this position. The measurements were done with brine and anisole in the large structure and with brine in the small structure. Figure 6.3 shows the mean velocity field for the reference measurement with brine in the large structure. Only one of three inlets and outlets is visible in the measurement plane. Part of the fluid enters through the pore on the left and then leaves the cell through the two pores on the lower right side (not visible in the measurement plane). This means that the fluid entering through the lower left pore is leaving the plane of measurement. Similarly the fluid on the upper half of the cell enters through the two pores on the upper left (not in the measurement plane) and leaves through the pore on the upper right. As a consequence of this, there is a horizontal line through the center of the pore across which no fluid flows in average.

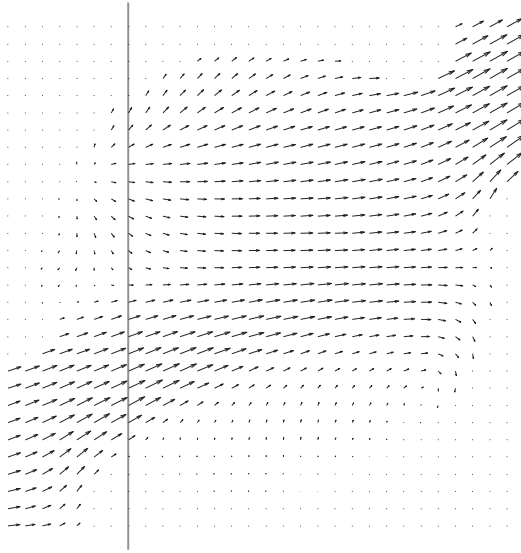As only two components of the velocity fluctuation are measured by

Figure 6.3: Mean velocity of an experiment with brine in the uncoated
large structure at a hydraulic Reynolds number of $Re_h =$
417. The vertical line indicates the position of the velocity
profile of Fig. 4.12.

PIV the third component had to be estimated from the first two. Com-
paring the two components measured by PIV it was observed that the
velocity fluctuations in x_1 and x_2 directions are not equal, especially
at low flowrates (Fig. 6.4). Only at hydraulic Reynolds numbers larger
than 300, velocity fluctuations can be considered as isotropic. At low
flowrates the fluctuations perpendicular to the main flow axis are lower
than in the main flow direction. It was therefore decided to calculate
the turbulent kinetic energy by assuming axisymmetric flow, i.e. the two
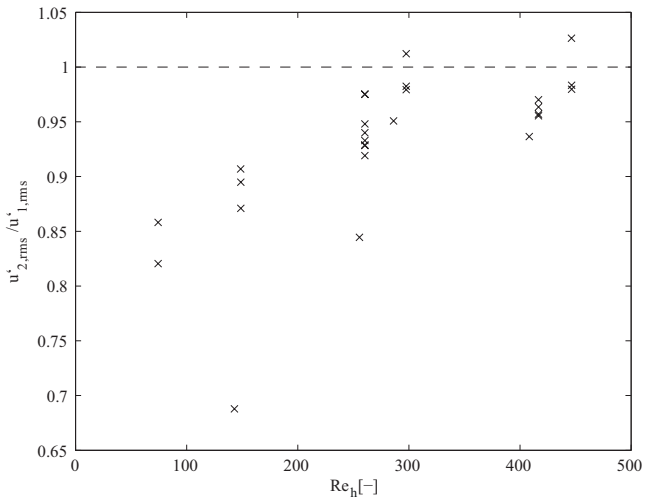components perpendicular to the main flow direction were assumed to

Figure 6.4: Ratio between root mean square velocity fluctuation in x_1 and x_2 direction.
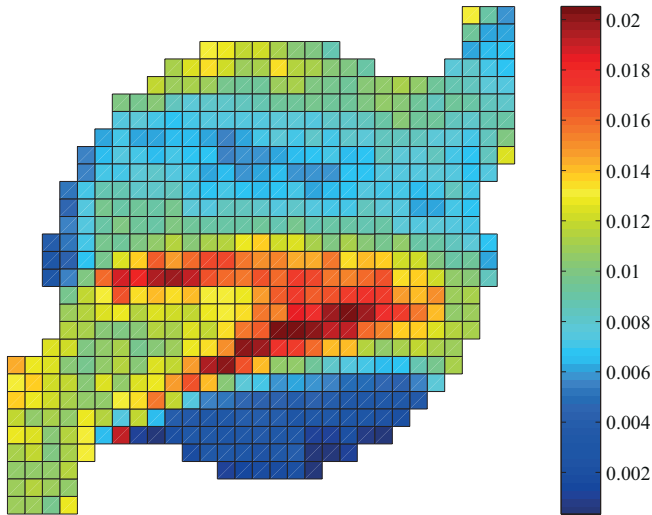
Figure 6.5: Turbulent kinetic energy field of an experiment with brine in the uncoated large structure at $Re_h = 417$.

be equal:

$$k = \frac{1}{2} \cdot \left(\overline{u'_1 u'_1} + 2 \cdot \overline{u'_2 u'_2} \right) \tag{6.19}$$

In Fig. 6.5 the profile of turbulent kinetic energy within a cell of the porous structure is shown. The turbulent kinetic energy is highest at the boundary of the jet. In comparison, the turbulent kinetic energy is very low on the upper half of the pore. What is also observed is that in the region of the outlet the turbulent kinetic energy is underestimated and periodicity is not given. This was observed also with anisole and in the small structure. I therefore attribute this to a measurement error, probably steming from refraction in the region of the pores. The reason is that the light is passing the phase boundary at a very high angle relative
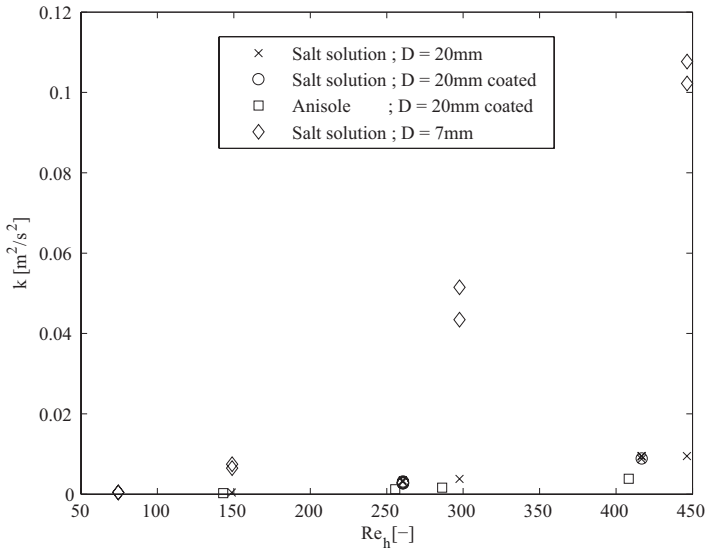
Figure 6.6: Turbulent kinetic energy as a function of hydraulic Reynolds number for different fluid viscosities and structure dimensions without scaling.

to the interface normal. As the RI matching is never perfect, this will always lead to some optical distortions that could lead to the lower value of k in the region of the outlet. Similar observations will be made in the two-phase flow experiments shown in Chapter 7. In the center of the cell however I observed good agreement between the measurements and a corresponding large-eddy simulation (Hutter et al., 2011b).

From the profile of the turbulent kinetic energy, the spatial mean value was calculated. The result is shown in Fig. 6.6. As expected, the turbulence intensity increases with increasing Reynolds number. What can be clearly seen is that for a given Reynolds number the turbulent kinetic energy is highest in the measurement in the small structure. The reason is that the characteristic dimension of this structure is a factor of 2.857
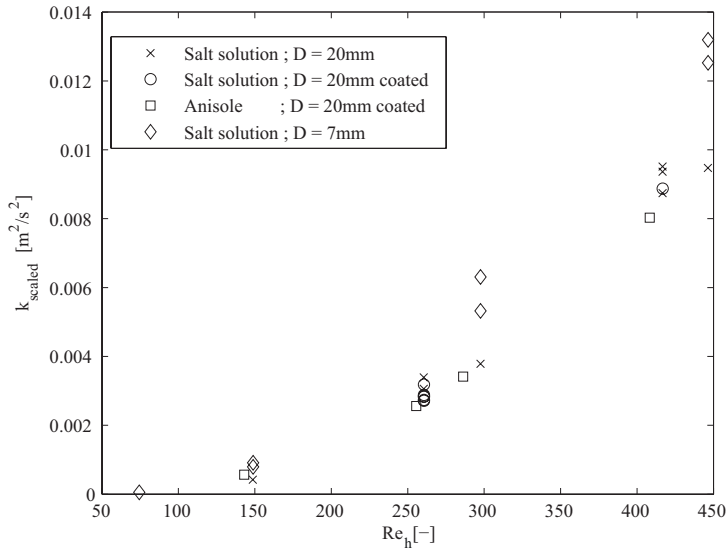
Figure 6.7: Scaled turbulent kinetic energy as a function of hydraulic Reynolds number.

smaller. I therefore scaled the turbulent kinetic energy with the scaling laws given in Section 6.3. The scaled results are given in Fig. 6.7. A good agreement is found between the measurements. Generally the turbulent kinetic energy can be measured with a high accuracy by PIV because the turbulent kinetic energy is mainly contained in the big (and therefore resolved) scales. The small scale motion, that may be unresolved in the PIV measurements, does not contain high kinetic energy and therefore their negligence does not impose large errors.

6.4.2 Dissipation rate of turbulent kinetic energy

Next, I evaluated the dissipation rate from the vector field obtained by PIV. First the isotropy ratios based on Delafosse et al. (2011) were
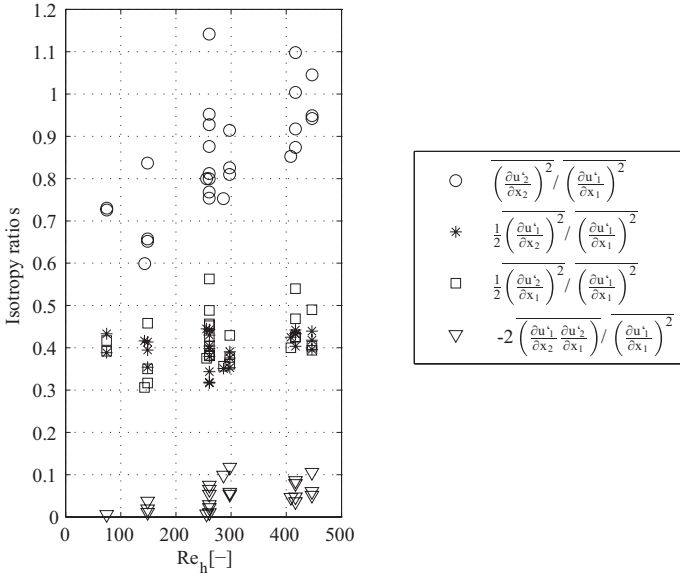
Figure 6.8: Ratio between squared gradients and cross product gradients in x_1 and x_2 direction as a function of the hydraulic Reynolds number.

calculated. Figure 6.8 shows the mean isotropy ratio of every experiment as a function of the hydraulic Reynolds number. It can be seen that the ratio of the square gradients is ≈ 1 respectively ≈ 0.5 the ratio between cross-product gradient and square gradients is ≈ 0.1. This observation is in very good agreement to the work by Delafosse et al. (2011) who measured dissipation rate in a stirred tank. Therefore, their dissipation rate model (Eq. 6.9) seems appropriate also for my case.

If the dissipation rate is plotted against the Reynolds number without scaling, I observe the highest values in the measurements in the small structure. The scaling laws introduced in Section 6.3 were used to compare the results (Fig. 6.9). It is observed that the results have
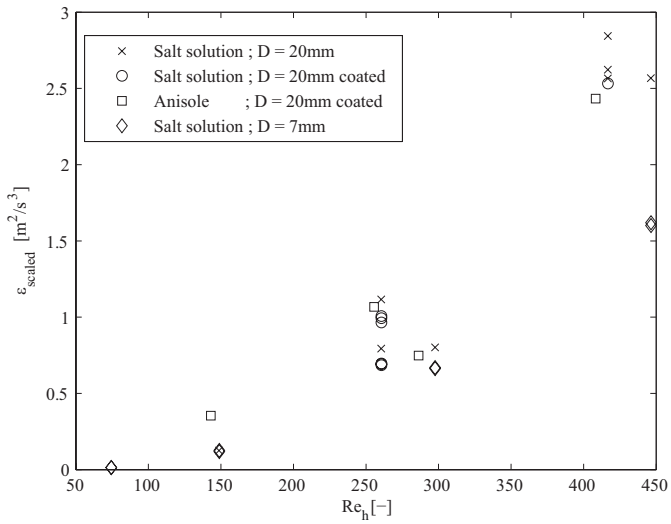
Figure 6.9: Scaled dissipation rate as a function of hydraulic Reynolds number.

a reasonably small standard deviation for measurements of dissipation rate. In comparison to the measurement of k, the deviation between the measurements is higher. What stands out is that the values for the small structure ($D = 7\,\text{mm}$) are considerably lower than the others. The reason for this is that the relative resolution in these measurements is worse. It is well known that the dissipation rate is a quantity that cannot be measured accurately with PIV because of the high demands on the spatial resolution (Xu and Chen, 2013). As dissipation occurs at the smallest scales of motion a measurement should resolve these scales. In my case the resolution Δ was larger than the Kolmogorov length scale, that was calculated as:

$$l_K = \left(\frac{\nu^3}{\varepsilon}\right)^{1/4} \tag{6.20}$$

To simplify the discussion, I restrict myself to the spatially averaged value of the experiment with saltwater in the large structure. I found that $l_{K,max} = 98\,\mu\text{m}$ at the lowest Reynolds number and $l_{K,min} = 45\,\mu\text{m}$ at the highest Reynolds number. The resolution of the PIV measurements in the same experiment was $\Delta = 268\,\mu\text{m}$. Therefore in relation to the Kolmogorov scales, the resolution is a factor of $2.7 - 6$ lower. When the resolution is insufficient the estimated values are lower than the real ones because small scale velocity gradients are filtered. The discussion of the effect of measurement resolution is found in many publications (Saarenrinne and Piirto, 2000; Saarenrinne et al., 2001; Baldi and Yianneskis, 2003; Delafosse et al., 2011; Sharp and Adrian, 2001). These publications illustrate the inherent uncertainties of PIV for dissipation rate measurements. A further challenge is that the dissipation rate is not homogeneous and therefore there are regions in the porous structure where the Kolmogorov length scale is even smaller. A local distribution of measured dissipation rate values is shown in Fig. 6.10. The region of maximum dissipation rate is found at the boundary of the jet entering the cell. Local values of the dissipation rate are more than 2.5 times higher than the average. Therefore, according to Eq. (6.20) the Kolmogorov length scale in these regions are $\approx 20\,\%$ lower than the average. In these regions the error from insufficient resolution is even higher. The most important challenge regarding resolution is however that the true value of the dissipation rate is unknown. l_K was determined by using
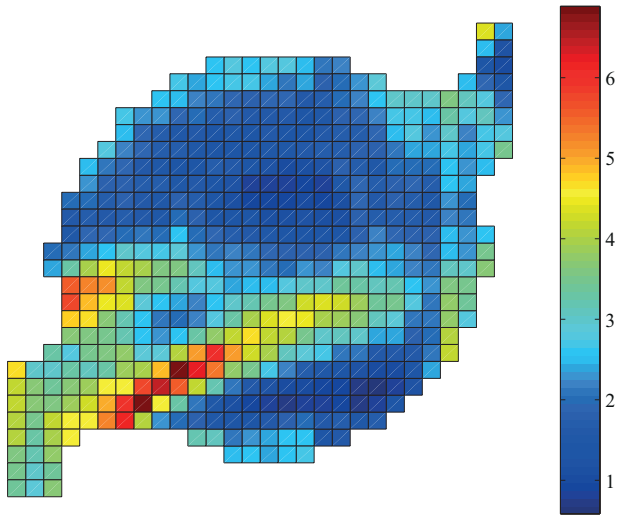
Figure 6.10: Local values of the dissipation rate for the experiment with brine in the uncoated large structure at $Re_h = 417$.

the measured dissipation rate which is known to be underestimated. In the following, I discuss the error propagation in the estimation of the Kolmogorov length scale. According to Saarenrinne et al. (2001) a resolution of $\Delta = 9l_K$ leads to a dissipation rate that corresponds to 65 % of the true value. Assuming $\Delta = 9l_K$, I recalculated the Kolmogorov length scale with a corrected dissipation rate of $\hat{\varepsilon} = 1/0.65 \cdot \varepsilon$. With this assumption, $\hat{l}_{K,min} = 40\,\mu m$ and $\hat{l}_{K,max} = 88\,\mu m$ is obtained. This corresponds to a 10 % decrease. This means that large changes in the dissipation rate only lead to small changes in the Kolmogorov length scale. Even if the dissipation rate was ten times higher, this would only result in a 44 % smaller Kolmogorov length scale. The relative resolution would then be $4.8 - 10$. With this resolution the estimated values would still have a reasonably low error. From this I conclude that Δ/l_K is not much larger than the above estimated $2.7 - 6$.

6.4.3 Turbulent diffusivity

Finally, I want to use the measured quantities to investigate mass transport phenomena. In Chapter 4, the axial dispersion in a flow through the porous structure was investigated. Dispersion of mass in axial direction is governed by three effects: molecular diffusion, Taylor dispersion and turbulent mixing. By pulse experiments, the dispersion coefficient is obtained that includes all of these effects. The relative contribution of different mechanisms remains however unknown. Therefore, PIV measurements can be used to estimate the contribution of turbulent mixing to axial dispersion. This was done by employing the $k - \varepsilon$ model as introduced in Section 6.2. The resulting turbulent diffusivity is shown as a function of hydraulic Reynolds number in Fig. 6.11. It is observed that the turbulent diffusivity is a strong function of the Reynolds number. Overall, it increases by more than an order of magnitude when the hydraulic Reynolds number is increased from 150 to 450. Comparing the values of the turbulent diffusivity to the longitudinal dispersion, it is observed that the values are three orders of magnitude lower even at the highest Reynolds number. Recalling that the dissipation rate is underestimated, it is expected that the *real* turbulent diffusivity is even smaller (Eq. 6.3). The longitudinal dispersion is therefore dominated by other effects. The molecular diffusion ($D_m = 1.9 \times 10^{-9}\,\mathrm{m\,s^{-1}}$) can be
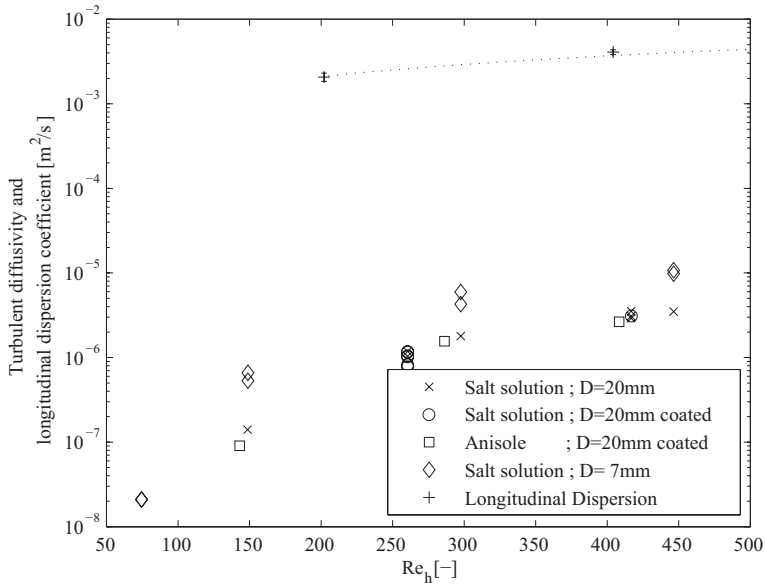
Figure 6.11: Comparison of turbulent diffusivity measured by PIV to
              longitudinal dispersion coefficient determined by pulse
              experiments.

excluded as it is even smaller than the turbulent diffusivity. I therefore conclude that the axial dispersion at the investigated Reynolds numbers is mainly governed by Taylor dispersion.

In Section 4.3.3 it was observed that at hydraulic Reynolds numbers between 200 and 1500, dispersion can be assigned to the turbulent dispersion regime. In this regime, equilibration of lateral velocity extremes led to a decrease in the relative longitudinal dispersion coefficient. By PIV experiments it was observed that at $Re_h > 300$, velocity fluctuations are isotropic. Further, a steep increase of turbulent diffusivity was observed between $Re_h = 150$ and $Re_h = 450$. These two observations suggest that the flow is turbulent. However, it was estimated that turbulent diffusivity is about three orders of magnitude smaller than axial dispersion. Therefore, at the investigated hydraulic Reynolds numbers between 150 and 450, Taylor dispersion outweighs the turbulent transport.

6.5 Conclusions

PIV measurements were conducted in a designed porous structure manufactured by rapid prototyping. This allowed measuring the velocity field along the axis of the porous structure. It was found that the length until the flow field is developed is maximal 5 periodic units. Experiments were then made with brine and anisole in the tenth periodic unit with structures of two different characteristic diameters. Scaling laws were deduced by employing Reynolds similarity, allowing to compare the results. It was found that at hydraulic Reynolds numbers $Re_h > 300$, velocity fluctuations are isotropic. The measurements were further used to discuss the local distribution of turbulent kinetic energy and of the dissipation rate. For the determination of the dissipation rate, a model had to be used because not all velocity gradients are observed by PIV. It was found that the ratios between squared velocity gradients are in good agreement to those observed by Delafosse et al. (2011). Generally, the dissipation rate of turbulent kinetic energy is a quantity that is only accurately measurable if the flow field is resolved down to the Kolmogorov length scales. Usually, this is not possible in PIV experiments and therefore the measured dissipation rate is underestimated. In

relation to the mean Kolmogorov length scale the resolution was $2.7 - 6$ times higher what means that dissipation rate is underestimated. From the dissipation rate and turbulent kinetic energy the turbulent diffusivity was calculated using the standard k-ε model. By comparison to the macroscopic experiments, it was concluded that turbulent transport is a minor contribution to longitudinal dispersion at hydraulic Reynolds numbers between 150 and 450.

Chapter 7

Two-phase flow through porous structures [1]

This Chapter compares a two-phase flow through a foam-like porous structure and a Sulzer SMX$^{\text{TM}}$ static mixing element. RI matching between two immiscible fluids and the internal structures enabled optical measurements to be performed. The droplet size and position within the internal structures were observed by laser-induced fluorescence. Details on the experimental procedure as well as the fluids used, can be found in Chapter 5.

Nondimensional numbers in two-phase flow are defined with continuous phase properties, hydraulic diameter, and interstitial velocity. Discussions about the characteristic diameter can be found in Section 1.3.1. The interstitial velocity u_I was calculated from the total volumetric flowrate $\dot{V}_a + \dot{V}_b$, where $\dot{V}_a$ denotes the volumetric flowrate of the disperse phase (anisole), and $\dot{V}_b$ the flowrate of the continuous phase (brine). The hydraulic Reynolds number for two-phase flow is defined as follows:

$$Re_h = \frac{u_I d_h}{\nu_b}. \tag{7.1}$$

with the viscosity of the continuous phase (ν_b). The hydraulic Weber number is defined as follows:

$$We_h = \frac{\rho_b u_I{}^2 d_h}{\sigma} \tag{7.2}$$

---

[1] Parts of this Chapter is published in Häfeli R., Rüegg O., Altheimer M., Rudolf von Rohr Ph., Investigation of emulsification in static mixers by optical measurement techniques using refractive index matching. *submitted*

It can be thought of as the ratio between inertial forces and surface forces. It will be used to correlate the droplet size. The volumetric transport fraction of the disperse phase is defined as follows:

$$\dot{\varepsilon} = \frac{\dot{V}_a}{\dot{V}_a + \dot{V}_b}. \tag{7.3}$$

In the following, I will show local droplet concentrations within the porous structures. Next, the droplet size distribution is discussed. Then, the droplet size along the structures is discussed. Finally, droplet size as a function of flowrate and volumetric transport fraction will be analyzed and compared to literature.

7.1 Local droplet concentration

The LIF image was used to identify the regions of the disperse phase in the porous structure. From this, the local hold-up and droplet size were estimated. Figure A.6 shows the local distribution of the hold-up in the Sulzer SMX$^{\text{TM}}$ static mixer in an experiment with a volumetric transport fraction of 4 %.

The fluid streams upwards and the ligaments in the measurement plane are aligned from bottom left to top right. It is observed that at low hydraulic Reynolds numbers, the droplets are inhomogeneously distributed. The highest local hold-up is observed below the ligaments. The accumulation of droplets below the ligament can be described by buoyancy. As the droplets have a lower density than the continuous phase, they possess a higher velocity and collect below the ligaments of the static mixer. At higher hydraulic Reynolds numbers ($Re_h = 142$), droplets are distributed more homogeneously. However, there remain some regions of higher droplet concentration. Apart from the area below the ligament, there are two areas with higher droplet concentration. At hydraulic Reynolds numbers of $Re_h = 190$ and $Re_h = 285$, droplets can be found at any position within the static mixer. At these hydraulic Reynolds numbers, only the small zone behind the ligament near the wall exhibits higher droplet concentrations, possibly because droplets are guided there by other ligaments.
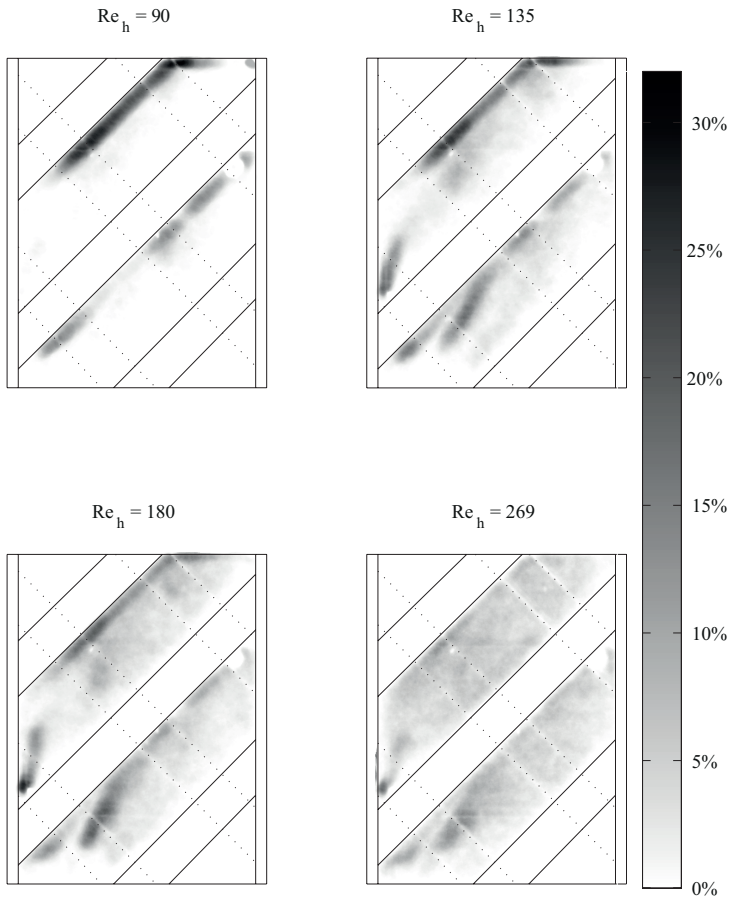
Figure 7.1: Average distribution of hold-up in SMX static mixer at volumetric transport fraction of 4 %. The boundary of the tube as well as the in-plane ligaments are indicated by solid lines. Out-of-plane ligaments are indicated by dotted lines. Figures for higher volumetric transport fractions can be found in Appendix A.

An additional observation is that there seem to be lines where very few droplets are observed. These lines appear due to the refraction of light at the ligaments that are between the measurement plane and the camera. As the RI of the solid and the fluid was matched, refraction should not have occurred. However, the match was not perfect, and some refraction always occurs. This is especially the case when a light ray crosses a phase interphase with an incident angle close to 90°. According to Snell's law, the relation between the angle of incidence (θ_1) and the angle of refraction (θ_2) is given as follows:

$$\frac{sin(\theta_1)}{sin(\theta_2)} = \frac{n_2}{n_1} \tag{7.4}$$

If the RI of the solid and the fluid show a mismatch in the third digit, e.g., $n_2 = 1.515$ and $n_1 = 1.514$, an incident light beam with an angle of 90° leaves the interface with an angle of 87.9°. In contrast, an incident light beam with an angle of 10° is refracted with an angle of 9.99°. This shows that even though refraction was generally not a problem, it can still have disturbed the experiments in cases where the light passed a phase interface with a high angle to the normal.

In the foam-like porous structure, droplets were not observed to accumulate due to buoyancy. Figure 7.2 shows the velocity field inside the porous structure (from Section 6.4.1) and the local hold-up at three different hydraulic Reynolds numbers. The velocity field was measured by PIV in single-phase flow. Preliminary measurements by PIV were also done for two-phase flow as indicated in Fig. 5.4. It was observed that PIV particles are well observable in the light transmitted by the dichroic mirror. Instead of doing simultaneous PIV and LIF measurements, it was decided to focus on LIF for the investigation of droplet size in porous structures. Therefore, PIV measurements with sufficient quality were not made in two-phase flow through porous structures. Even though it is expected that the average velocity profile is different in single- and two-phase flow, it is here assumed that single-phase PIV measurements can be used as a first approximation of the velocity profile in two-phase flow. From the vector field in Fig. 7.2 it is concluded that there is a horizontal line over which there is few mass flux in average. This means that the fluid entering the cell from the bottom left leaves the measurement plane and exits the cell via two pores on the bottom right of the
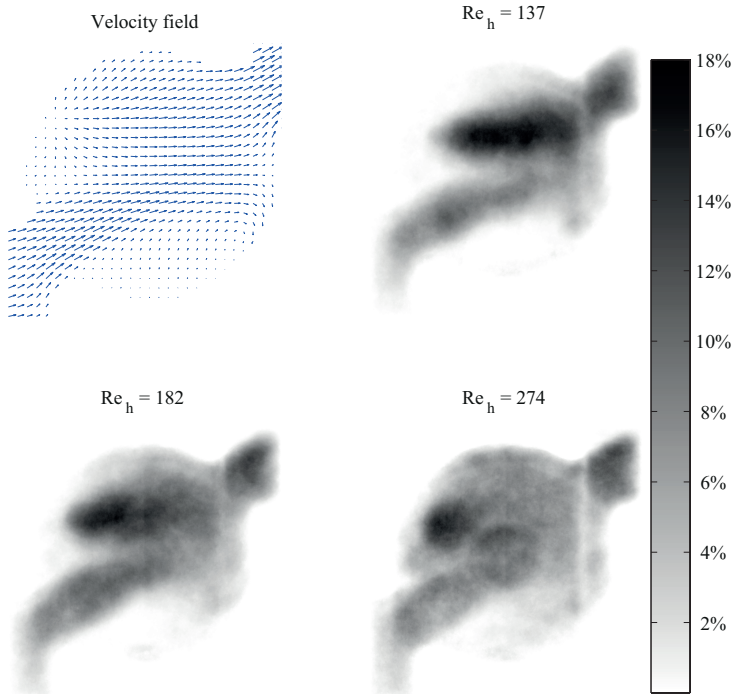
Figure 7.2: Velocity field (see Section 6.4.1) and average distribution of hold-up in foam-like porous structure. The volumetric transport fraction is 4 %. Figures for higher volumetric transport fractions can be found in Appendix A

cell (not visible in the measurement plane). Similarly, the fluid enters through two pores on the top left of the cell and leaves the cell through the visible pore at the top right. It is expected that in a first approximation, this feature of the flow through the porous structure remains the same in two-phase flow. At a hydraulic Reynolds number of 145 it can be seen that droplets are mainly found in the bulk flow. An exception is found in the recirculation zone where droplets are encountered more frequently. Apart from that, the hold-up near the boundary of the cell is lower. At higher flowrates, the distribution of droplets is more homogeneous.

Again, the limitation of the RI matching technique for the measurement of local hold-up distributions is visible. At the right of the pore, there is a band of low hold-up because the illuminating laser crosses a phase interface at a very high angle to the interface normal. As discussed above, this leads to strong refraction even for accurately matched RIs. A similar effect occurs on the path of light between the measurement plane and the camera. It crosses a phase interphase perpendicularly and is refracted. This produces a circle of low hold-up in the center of the measurement plane. This effect is less pronounced at low flowrates because droplets are larger and can still be correctly identified even when a stripe within the droplet is insufficiently illuminated.

7.2 Droplet size distribution

The droplet size was estimated from 2000 images. The histogram of the number distribution was obtained by classifying the size in bins of 0.05 mm. For the modeling of mass transfer in the chemical reactor, we are interested in the area rather than the number of droplets. Therefore, the number distribution was transformed into the area distribution. Figure 7.3 shows the number and area distributions of measurements upstream and inside the foam-like porous structure. The mode of the area distribution is at a larger diameter than the mode of the number distribution because larger droplets have a larger surface area.

A meaningful characteristic of the droplet size distribution is the maximum stable droplet diameter d_{max}. Instead of estimating d_{max}, droplet sizes are frequently related to d_{90}, a value that is measured with more
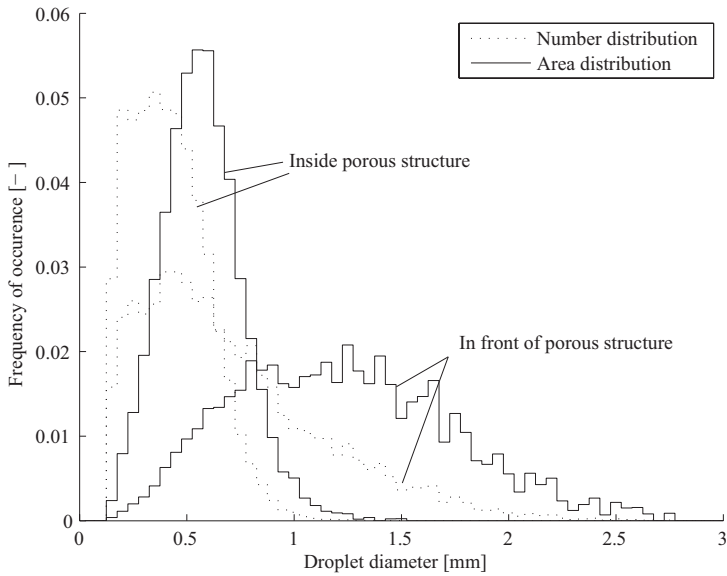
Figure 7.3: Histogram of droplet sizes for an experiment with 10 % vol-
umetric transport fraction and $Re_h = 204$: size distribu-
tion in front of porous structure and inside porous structure
(201 mm from the entrance).

confidence (Theron and Le Sauze, 2011). d_{90}, d_{50} and d_{10} are the largest diameters that represent 90 %, 50 %, and 10 % of the volume of the droplets, respectively. Instead of using d_{max} or d_{90} to characterize the droplet size distribution, models in the literature usually report the Sauter mean diameter (Lemenand et al., 2003):

$$d_{32} = \frac{\sum_i n_i d_i^3}{\sum_i n_i d_i^2} \tag{7.5}$$

where n_i is the number of droplets of size d_i. The Sauter mean diameter is the diameter of monodisperse droplets that have the same area to volume ratio as the measured droplet collective. This is motivated by a study by Sprow (1967), who found that in emulsification in a stirred tank, numerous average diameters are directly proportional to the maximum drop size. Figure 7.4 shows that in my experiments, both d_{90} and d_{10} are linearly correlated to the Sauter mean diameter. It is also observed that the ratios d_{90}/d_{32} and d_{10}/d_{32} are similar for the Sulzer SMX$^{\text{TM}}$ static mixer and the foam-like structure. I conclude that the droplet size distribution can be well characterized by the Sauter mean diameter.

7.3 Droplet size along the structures

Figure 7.3 already showed that in front of the porous structure, the droplets are larger and have a wider size distribution. Inside the porous structure, the droplets were smaller and showed a narrower size distribution. More quantitative insight into the break-up mechanism is gained by measuring the droplet size along the porous structure. Figure 7.5 shows the evolution of d_{32} in the foam-like porous structure and in the SMX. Measurements were made for volumetric transport fractions of $\dot{\varepsilon} = 4\,\%$ and $\dot{\varepsilon} = 10\,\%$. I first discuss the results for $\dot{\varepsilon} = 10\,\%$. The initial droplet size (produced by a nozzle of 1 mm diameter) was 1.20 mm in the experiment with the foam-like porous structure and 1.49 mm in the experiment with the Sulzer SMX$^{\text{TM}}$. The difference can be caused by several factors. One is that the measurement plane for the SMX was 2 mm off center owing to the requirements of the structure. Another reason is a difference in pressure drop between the two structures. This results in
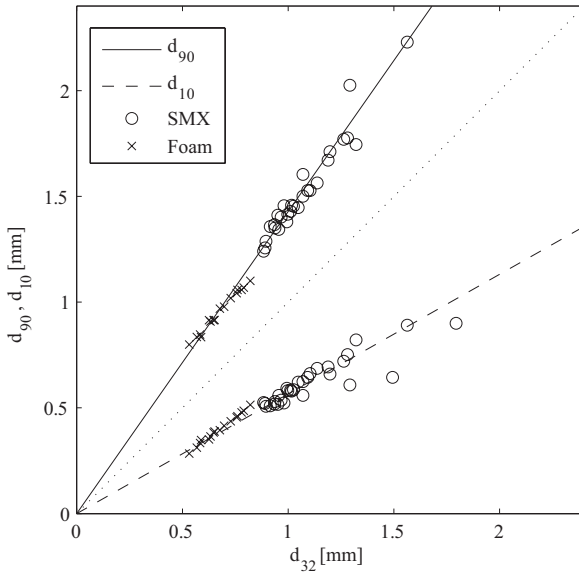
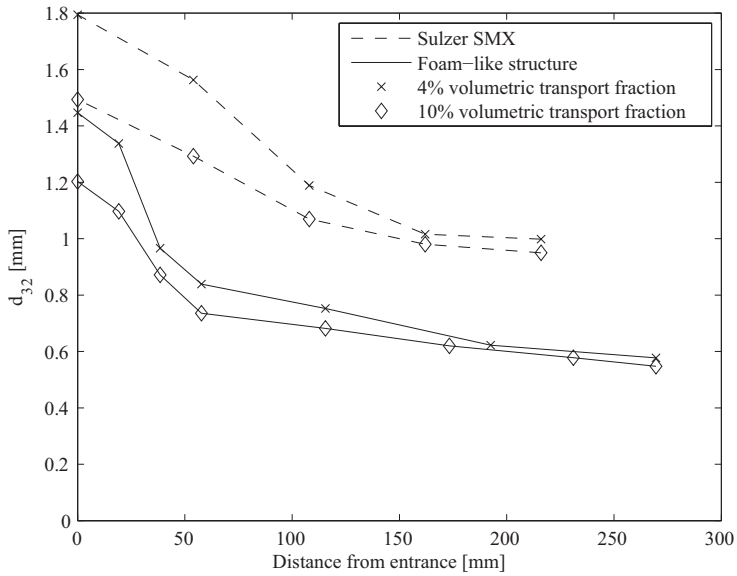**Figure 7.4:** Characteristic diameters d_{90}, d_{10} and d_{32} in comparison.

Figure 7.5: Break-up of droplets as they travel through porous structures.

different pressures at the nozzle, what eventually affected the operation of the nozzle. Another effect could be a coupling between pressure variations in the porous structure and at the nozzle. Notwithstanding these differences, the droplet size at the entrance varied by only 24 % between the foam-like structure and the SMX. In the foam-like porous structure, it was observed that within the first 50 mm, the droplet size was reduced from 1.20 mm to 0.74 mm. Further downstream, the droplets approached a diameter of approximately 0.55 mm. In the SMX, the reduction of droplet size was slower, and the droplets approached a final size of approximately 0.95 mm.

In the experiments with $\dot{\varepsilon} = 4\,\%$, the observations are similar. The initial droplet size was 1.45 mm in the experiment with the foam-like porous structure and 1.80 mm with the SMX. This corresponds to a difference of 24 %, and the same reasons as for the experiments with $\dot{\varepsilon} = 10\,\%$ apply. The difference in initial droplet size between the experiments with $\dot{\varepsilon} = 4\,\%$ and $\dot{\varepsilon} = 10\,\%$ can be explained by the production of the droplets by the nozzle. At a lower flowrate ($\dot{\varepsilon} = 4\,\%$), the nozzle produces smaller droplets. Toward the end of the structures, the difference in droplet size for the experiments with $\dot{\varepsilon} = 4\,\%$ and $\dot{\varepsilon} = 10\,\%$ diminishes.

7.4 Effect of flowrate and volumetric transport fraction

Figure 7.6 shows the droplet size as a function of the volumetric transport fraction and interstitial velocity. These measurements were conducted at ≈ 200 mm from the entrance of the two geometries. Again, I observed that the droplets in the foam-like structure are smaller than in the SMX. The interstitial velocity appears to have a strong effect on the droplet size. In comparison, changing the volumetric transport fraction from $\dot{\varepsilon} = 4\,\%$ to $\dot{\varepsilon} = 10\,\%$ appears to have a minor effect on the droplet size. A clear effect of the volumetric transport fraction cannot be identified. At high flowrates, larger droplets were observed at higher volumetric transport fractions. This is according to expectations as a higher droplet density generally leads to a higher droplet coalescence rate. However, at low flowrates, the droplets were smaller for higher volumetric transport fractions. This observation is made in the foam-like porous structure as
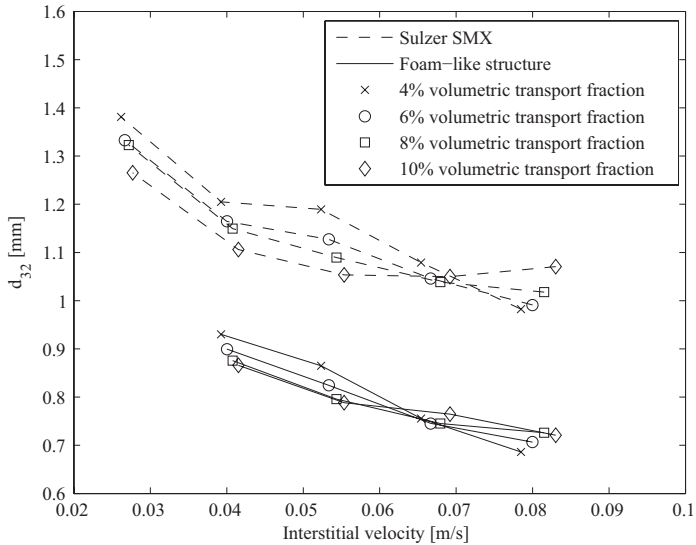
Figure 7.6: Droplet size as a function of interstitial velocity and volumetric transport fraction for Sulzer SMX$^{\text{TM}}$ static mixer and foam-like porous structure.

well as in the SMX because of variations in the inlet droplet size. As discussed above, the droplets were produced by a nozzle with an inner diameter of 1 mm. The size of the droplets produced by this nozzle depends on the flowrate through the nozzle. It is possible that some effect of the volumetric transport fraction stems from this. According to Fig. 7.5, small changes in the droplet size still occur even after 200 mm.

7.4.1 Comparison to literature

Middleman (1974) proposed a correlation assuming Kolmogoroff's theory of turbulence, and here, it is written according to hydraulic numbers:

$$\frac{d_{32}}{d_h} = C_1 We_h{}^{-0.6} f_h{}^{-0.4} \tag{7.6}$$

In the turbulent pipe flow, the friction factor f_h is a weak function of the Reynolds number. With the approximation

$$f_h \propto Re_h{}^{-0.25} \tag{7.7}$$

the droplet size was given as a function of the Weber and Reynolds numbers:

$$\frac{d_{32}}{d_h} = C_1 We_h{}^{-0.6} Re_h{}^{0.1} \tag{7.8}$$

Some authors estimated the value of the exponents by varying dimensionless numbers (e.g. Legrand et al., 2001). When operating in the turbulent flow regime, the exponent of the Weber number reported in the literature ranges from -0.5 to -0.859; however, most authors report a value close to -0.6 (Theron and Le Sauze, 2011).

At intermediate Reynolds numbers, the droplet size is still a function of the Reynolds and Weber number; however, the exponents change. Theoretically, experimental data could be used to fit the exponents of a correlation. However, to do so, the nondimensional numbers should be varied independently. This can be achieved by varying the viscosity and interface tension. In my case, the challenge is that the RI has to be constant. Therefore, I only varied the flowrate and volumetric transport fraction and compared my experiments to correlations available in the literature. A study of emulsification in a Sulzer SMX$^{\text{TM}}$ static mixer at
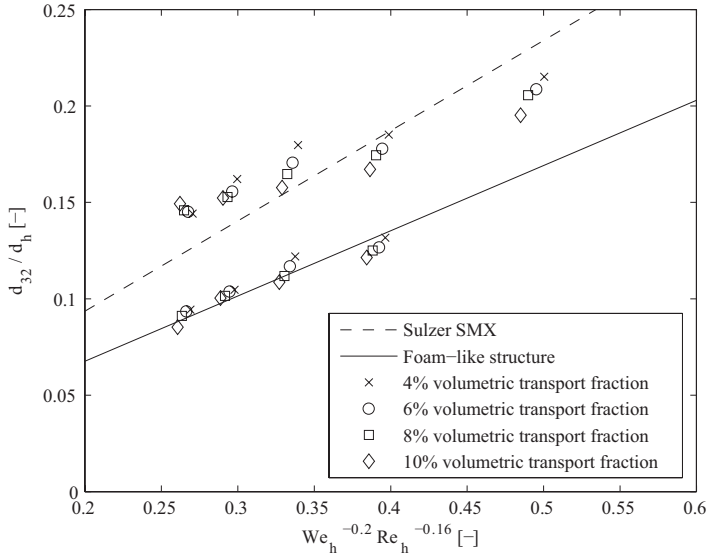
Figure 7.7: Correlation of experimental data in terms of the hydraulic Weber and Reynolds numbers.

similar Reynolds numbers was conducted by Legrand et al. (2001). They used three fluid pairs to investigate the droplet size at Reynolds numbers between 4 and 320. Their correlation in terms of hydraulic numbers is as follows:

$$\frac{d_{32}}{d_h} = C_2 \, We_h{}^{-0.2} Re_h{}^{-0.16} \tag{7.9}$$

It described their experimental values with a mean error of approximately 10 %. I found that my experiments could also be well described by an expression with these exponents. Figure 7.7 shows the droplet size as a function of $We_h{}^{-0.2} Re_h{}^{-0.16}$. It appears that the curves of the two static mixers show a different slope. The data of the SMX is correlated by $C_2 = 0.47$ and shows an error of 13 %. The data of the foam-like structure is correlated by $C_2 = 0.34$ and shows an error of 4 %.

The two investigated structures show different emulsification performances even though they have the same hydraulic diameter and the same porosity. The differences in droplet size therefore arise from differences in the geometry. A substantial difference between the structures is their free cross section. The average free cross section of the two structures is equal as they have the same porosity. However, the foam-like structure shows strong variations, as discussed in Section 2.3. Therefore, the fluid is repeatedly accelerated and decelerated. In my experiments, it was observed that in the structure that shows large changes in the free cross section, the droplets produced are smaller.

7.5 Conclusions

I introduced a system of two immiscible fluids and a solid (manufactured by rapid prototyping), all three of which have the same RI. This system permits optical measurements in two-phase flow through designed porous structures. I used this to investigate liquid-liquid two-phase flow through a foam-like porous structure and a Sulzer SMX$^{\text{TM}}$ static mixing element.

Using LIF, a fluorescent tracer in the disperse phase was observed. This enabled me to observe the droplet size and position inside a porous structure. I observed that at low flowrates, droplets follow preferred paths, whereas at higher flowrates, they are more homogeneously distributed within the structures.

The droplet size distribution was found to be well represented by the Sauter mean diameter d_{32}. By measuring along the porous structure, I found that the droplet size is quickly reduced in the foam-like porous structure. In comparison, the droplets in the SMX disintegrate more slowly, and the final droplet size is larger. As both geometries have the same porosity and hydraulic diameter, I conclude that the change in the free cross section is also an important parameter. I observed that in the geometry with large changes in the free cross section, the droplets are smaller.

Further, I investigated how the droplet size is affected by changes in flowrate and volumetric transport fraction. I observed that the droplets are smaller at higher flowrates. The effect of the volumetric transport fraction was found to be undetermined. Owing to droplet coalescence,

larger droplets are generally expected when the volumetric transport fraction is higher. However, this was only observed at high Reynolds numbers. I conclude that the measured droplet size is affected by the size produced by the nozzle. Small changes in droplet size are observed even after 200 mm of the structures.

Finally, droplet sizes were correlated as a function of dimensionless numbers. In accordance with Legrand et al. (2001), who studied emulsification in a SMX at similar Reynolds numbers, it was found that the droplet size correlates well to ($We_h^{-0.2} Re_h^{-0.16}$).

Chapter 8

Thesis outlook

8.1 Mass transfer in two-phase flow

Axial dispersion was investigated for single-phase flow. However, in many reactions encountered in the industry, two phases are present. Adding a second phase to the flow alters the axial dispersion of a tracer in the continuous phase. In microfluidic systems, Trachsel et al. (2005) observed a significantly lower dispersion coefficient in two-phase flow. The reason was that the segmented gas-liquid flow regime was encountered. The segments behave like batch reactors with few exchange of mass between them. Therefore the residence time distribution is narrow compared to single-phase flow in the same device.

The effect of a second phase on the dispersion coefficient in the bubbly flow regime is not straightforward to understand. The effect of the bubbles on the dispersion coefficient can be a function of their size. Figure 8.1 shows bubbly two-phase flow through an empty tube for varying bubble sizes. When the bubbles are large and approach the size of the tube (Fig. 8.1, left), the slug flow regime is approached. As discussed before, in this case the axial dispersion is reduced because the gas phase acts as a barrier for mass transfer in axial direction. For smaller droplets (Fig. 8.1, center and right) the liquid is no more segmented by the gas. Therefore, the dispersion coefficient is expected to be higher in bubbly flow compared to slug flow.

However, the dispersion coefficient in bubbly flow could be lower than in single-phase flow. The effects over which the disperse phase influences dispersion in the continuous phase are diverse. Depending on the size of the bubbles, turbulence can be augmented or reduced (Gore and Crowe,

Figure 8.1: Bubbly flow in empty pipes (adapted from Büchi (2011)).

1991). However, the knowledge of the effect of bubbles on the dispersion in the continuous phase is rather incomplete. Figure 8.2 shows experiments of axial dispersion by a wire mesh sensor. It was found that in bubbly flow, the dispersion coefficient is reduced compared to single-phase flow (Büchi, 2011). However, the data shows large uncertainties. The reason is that the signal measured by the wire-mesh sensor is not only a function of the tracer concentration but also of local bubble distribution within the sensor. An appropriate experimental technique would be able to exclusively measure the concentration of the tracer in the continuous phase. This could be done for example by optical measurements using RI matching. Such experiments are possible with the fluids introduced in this thesis if anisole is used as the continuous phase. In that case, Rhodamine B can be used as tracer substance, the concentration of which being measured inside a porous structure.

8.2 Laminar-turbulent transition

Within this thesis, particle image velocimetry was employed to study the velocity field inside the porous structure. Starting from $Re_h \approx 300$, isotropic velocity fluctuations were observed. This is an important characteristic of turbulent flow. While this Reynolds number compares well with literature values on flow regime transition in packed beds, a deeper understanding of flow regimes in flow through the regular foam-like porous structure is still missing. Especially, the Reynolds number at which onset of velocity fluctuation occurs, has not been investigated the
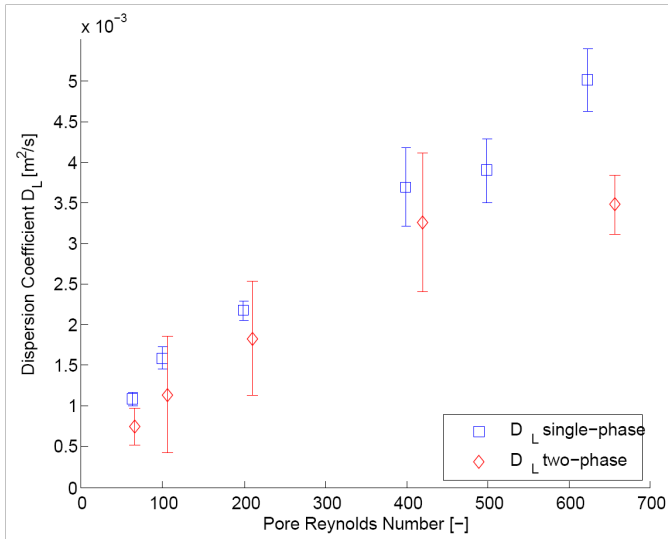
Figure 8.2: Longitudinal disperison coefficient in bubbly flow through porous structures as measured by a wire-mesh electrode (adapted from Büchi (2011)).

regular foam-like porous structure.

Flow regime transition could be studied by pressure drop measurements or by studying velocity fluctuations. Morancais et al. (1999) measured the presssure drop in a static mixer to distinguish between viscous and the inertial flow regime. Alternatively, flow regimes can be investigated by measuring velocity fluctuations. This could for example be achieved by electrochemical probes (e.g. Bu et al., 2015).

8.3 Optical measurements

In this thesis, two liquids are introduced which have the same RI as a porous structure manufactured by rapid prototyping. This allows to experiment with geometries that can not be manufactured by traditional manufacturing techniques. The drawback of the RI matching technique is that it is only available for few liquids. In single-phase flow this is a minor issue, as Reynolds similarity can be employed. Eventually, it can be of interest to modify the viscosity of the index matched fluid. This should be done in a way that does not affect the RI nor the transparency of the fluid.

In two phase flow, more non-dimensional numbers have to be similar. Apart from Reynolds number the Weber number, the viscosity ratio and the density ratio of the fluids are known to play a role for the droplet size. Experiments with the brine and anisole do not allow to vary these numbers independently. Therefore it could be of interest to change the molecular properties of the liquids or to find other liquids with the same RI. As some salts show a higher solubility at higher temperatures, the choice of materials can be expanded by raising the temperature of the experimental setup. Another option is to change the molecular properties of anisole and the brine. The surface tension can be changed by adding surfactants. The viscosity of the fluids can be adjusted by addition of viscosifiers.

8.4 Optimal design of a porous structure

Rapid prototyping allows to design porous structures of almost arbitrary geometry. This allows to modify traditional static mixing devices and

column internals in order to further optimize them for a certain application. The optimal geometry of a structure depends on the task for which it is intended. Typically requirements of catalyst supports, static mixers or column internals can be:

- Specific surface area for catalyst

- Heat transfer operation and thermal homogenization

- Mixing of miscible fluids

- Interface generation between non-miscible phases

Some of these requirements can be fulfilled by relatively simple design procedures, while others involve more complex phenomena. In the following, it will be shown how porous structures could be designed in order to fulfill these requirements.

For example, a high specific surface area requires the porous structure to be of small dimension. A given porous structure manufactured by rapid prototyping can be geometrically downscaled to reach a higher specific surface area. The limitations are given by the manufacturing procedure.

To homogenize temperature variations within a reactor the porous structure is preferably made of interconnected ligaments which are connected to the walls. Hutter et al. (2011c) found that this leads to a 30 % improvement of the heat transfer coefficient compared to a structure that is not physically connected to the wall. The porous structure could be further improved for heat transfer by designing the ligaments in such a way, that they are oriented in radial direction. A structure with ligaments all oriented in the same direction has an effective thermal conductivity that is 200 % higher than if the ligaments were oriented randomly, as can be seen by comparing Eq. (3.2) and Eq. (3.3). Alternatively, the ligaments could be designed such, that fluid streaming along the axis of the tube is guided towards the wall and vice versa. The effect of such a design on the effective thermal conductivity could be tested in experiments as described in Chapter 3.

Static mixers for mixing of miscible fluids can be operated in the laminar or turbulent regime. The commercially successful static mixers as Sulzer SMX$^{\text{TM}}$, Kenics, Lightnin Inliner, HEV and others all have rather

simple geometries. A detailed description of these static mixing devices is found in Thakur et a. (2003). With rapid prototyping it is possible to slightly modify these static mixers and to test their performance by experiments with laser induced fluorescence or with a wire-mesh sensor.

Interface generation between two immiscible fluids by a static mixer could be improved by varying the geometry. In the experiments on two-phase flow (Chapter 7), it was observed that in a structure with large variations in the free cross-sectional area the produced droplets are smaller. This could be an inspiration for static mixer design.

A Appendix

This appendix shows the distribution of droplets in the SMX static mixer and in the foam-like porous structure as a function of volumetric transport fraction and Reynolds numbers. The results for volumetric transport fractions of 4 % and the discussion can be found in Section 7.1.
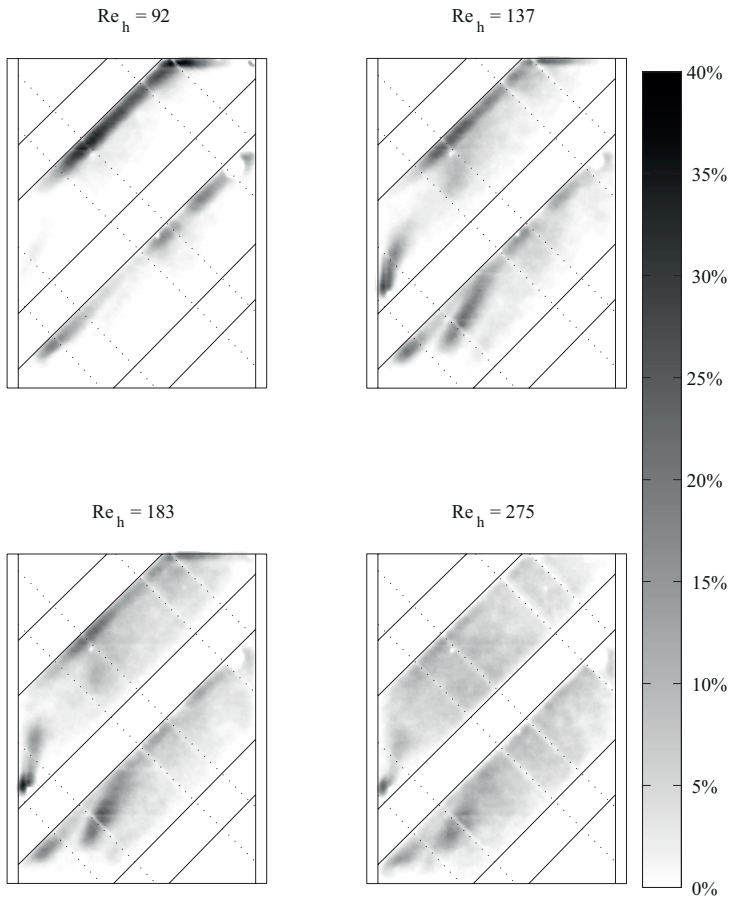
Figure A.1: Average distribution of hold-up in SMX static mixer at a volumetric transport fraction of 6 %.
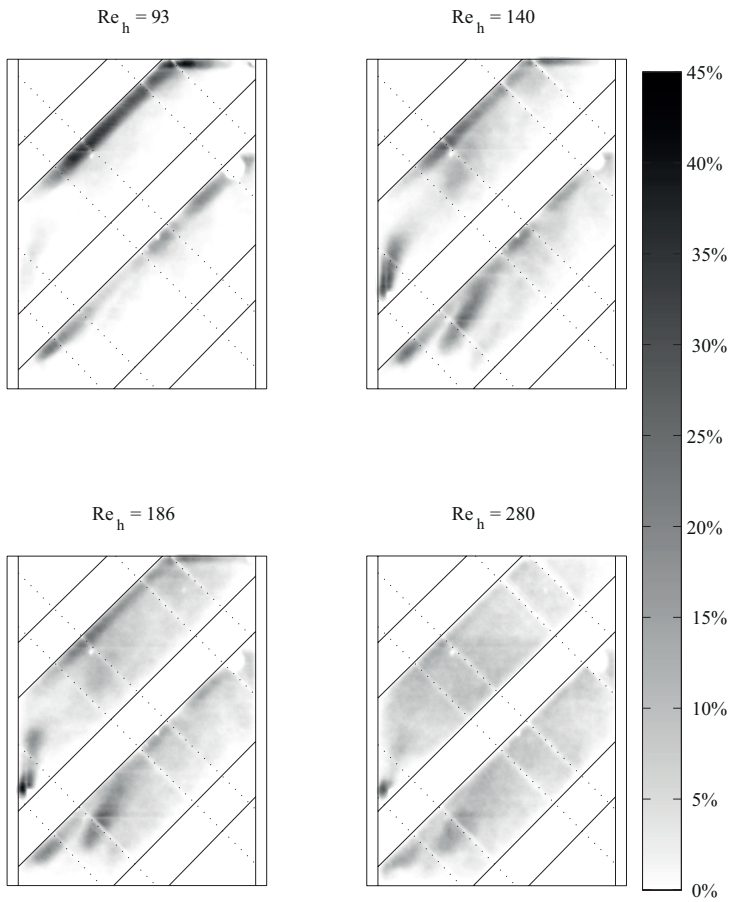
Figure A.2: Average distribution of hold-up in SMX static mixer at a volumetric transport fraction of 8 %.
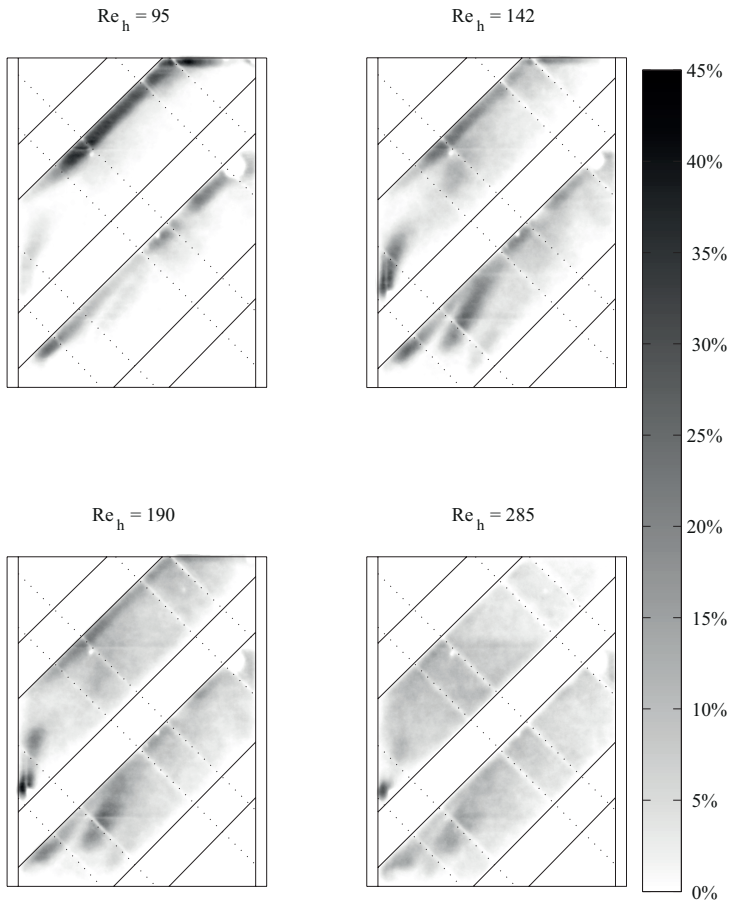
Figure A.3: Average distribution of hold-up in SMX static mixer at a volumetric transport fraction of 10 %.
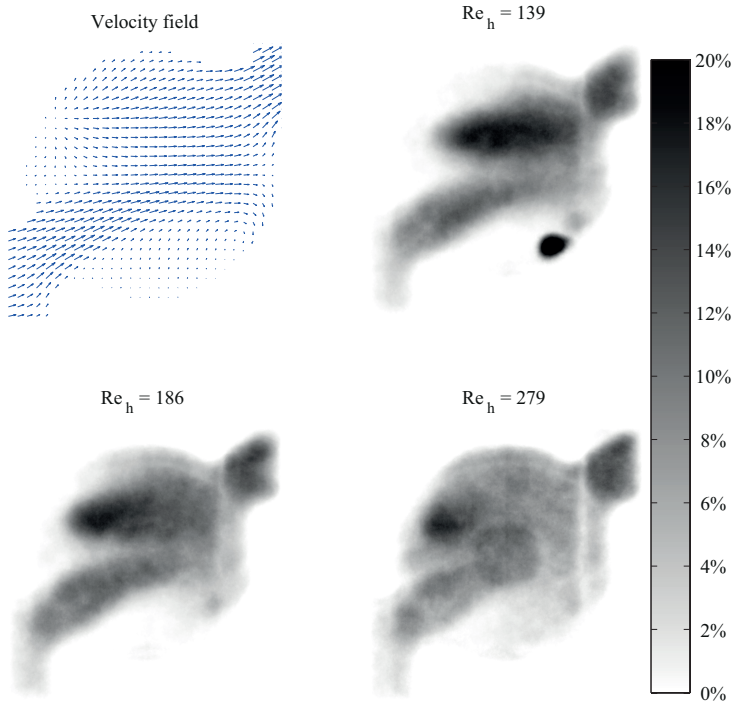
Figure A.4: Average distribution of hold-up in foam-like porous structure at a volumetric transport fraction of 6 %.
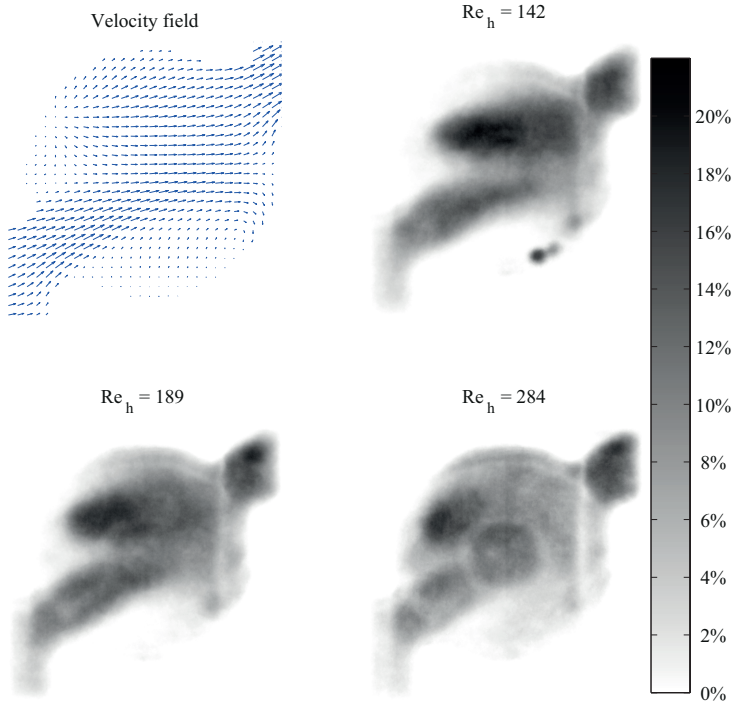
Figure A.5: Average distribution of hold-up in foam-like porous struc-
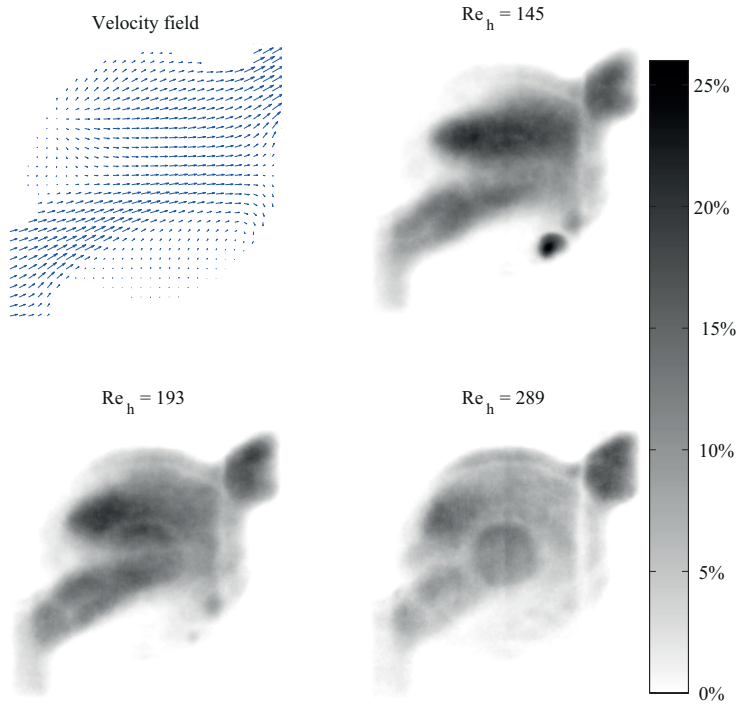ture at a volumetric transport fraction of 8 %.

Figure A.6: Average distribution of hold-up in foam-like porous struc-
ture at a volumetric transport fraction of 10 %.

Bibliography

Anderson M.R., Baughn J.W., (2004). Hysteresis in liquid crystal thermography. *J Heat Tranf*, 126, 339 − 346.

Augier F., Masbernat O., Guiraud P., (2003). Slip velocity and drag law in a liquid-liquid homogeneous dispersed flow. *AIChE J*, 49(9), 2300 − 2316.

Bağci Ö., Dukhan N., Özdemir M., (2014). Flow regimes in packed beds of spheres from pre-Darcy to turbulent. *Transp Porous Med*, 104, 501 − 520.

Baldi S., Yianneskis M., (2003). On the direct measurement of turbulence energy dissipation in stirred vessels with PIV. *Ind Eng Chem Res*, 42, 7006 − 7016.

Banhart J., (2001). Manufacture, characterisation and application of cellular metals and metal foams. *Prog Mater Sci*, 46, 559 − 632.

Barbin A.R., Jones J.B., (1963). Turbulent flow in the inlet region of a smooth pipe. *J Basic Eng-T ASME*, 85(1), 29 − 34.

Bonrath W., (2013). International Patent WO 2013/156502 A1.

Brenner H., (1980). Dispersion resulting from flow through spatially periodic porous media. *Philos T Roy Soc A*, 297.1430, 81 − 133.

Bröder D., Sommerfeld M., (2007). Planar shadow image velocimetry for the analysis of the hydrodynamics in bubbly flows. *Meas Sci Technol*, 18, 2513 − 2528.

Bu S., Yang J., Dong Q., Wang Q., (2015). Experimental study of flow transitions in structured packed beds of spheres with electrochemical technique. *Exp Therm Fluid Sci*, 60, 106 − 114.

Büchi D.., (2011). *Improvement of wire-mesh sensor for characterization of multiphase flow through chemical reactors.* (Master thesis). ETH Zürich, Switzerland.

Budwig R., (1994). Refractive index matching methods for liquid flow investigations. *Exp Fluids*, 17, 350 − 355.

Burdett I.D., Webb D.R., Davies G.A., (1981). A new technique for studying dispersion flow, holdup and axial mixing in packed extraction columns. *Chem Eng Sci*, 36(12), 1915 − 1919.

Butscher D., Hutter C., Kuhn S., Rudolf von Rohr Ph., (2012). Particle image velocimetry in a foam-like porous structure using refractive index matching: a method to characterize the hydrodynamic performance of porous structures. *Exp Fluids*, 53, 1123 − 1132.

Carman P.C., (1937). Fluid flow through granular beds. *Transactions-Institution of Chemical Engineers*, 15, 150 − 166.

Chaouki J., Larachi F., Dudukovic M., (1997). Noninvasive tomographic and velocimetric monitoring of multiphase flows. *Ind Eng Chem Res*, 36, 4476 − 4503.

Comiti J., Renaud M., (1989). A new model for determining mean structure parameters of fixed beds from pressure drop measurements: application to beds packed with parallelepipedal particles. *Chem. Eng. Sci.*, 44(7), 1539 − 1545.

Conan C., Masbernat O., Décarre S., Liné A., (2007). Local hydrodynamics in a dispersed stratified liquid-liquid pipe flow. *AIChE J*, 53(11), 2754 − 2768.

Danckwerts P.V., Continuous flow systems. *Chem Eng Sci*, 2 (1953), 1 − 13.

de Josselin de Jong G., (1958). Longitudinal and transverse diffusion in granular deposits. *EOS T Am Geophys Un*, 39(1), 67 − 74.

Delafosse A., Collignon M.-L., Crine M., Toye D., (2011). Estimation of the turbulent kinetic energy dissipation rate for 2D-PIV measurements

in a vessel stirred by an axial Mixel TTP impeller. *Chem Eng Sci*, 66, $1728 - 1737$.

Delgado J.M.P.Q., (2006). A critical review of dispersion in packed beds. *Heat Mass Transfer*, 42, $279 - 310$.

Doron P., Bertuccioli L., Katz J., (2001). Turbulence characteristics and dissipation estimates in the coastal ocean bottom boundary layer from PIV data. *J Phys Oceanogr*, 31, $2108 - 2134$.

DSM, (2012). Product Data Sheet, Somos®WaterShed XC 11122. Retrieved from `http://www.dsm.com/content/dam/dsm/somos/en_US/documents/Brand-Status-Product-Datasheets/US%20English%20-%20A4/Somos%20WaterShed%20XC%2011122%20-%20US%20English%20A4.pdf`

Dukhan N., Suleiman A.S., (2014). Simulation of entry-region flow in open-cell metal foam and experimental validation. *Transp Porous Med*, 101, $229 - 246$.

Dybbs A., Edwards R.V., (1984). A new look at porous media fluid mechanics - Darcy to turbulent. *Nato Adv Sci I E-App*, 82, $199 - 256$.

Efron B., (1979). Bootstrap methods: another look at the jackknife. *Ann Stat*, 7, $1 - 26$.

Fried J.J., Combarnous M.A., (1971). Dispersion in porous media. *Adv Hydrosci*, 7, $169 - 282$.

Fujiwara A., Danmoto Y., Hishida K., Maeda M., (2004). Bubble deformation and flow structure measured by double shadow images and PIV/LIF. *Exp Fluids*, 36, $157 - 165$.

Gendron P.-O., Avaltroni F., Wilkinson K.J., Diffusion coefficients of several rhodamine derivatives as determined by pulsed field gradient-nuclear magnetic resonance and fluorescence correlation spectroscopy. *J Fluoresc*, 18 (2008), $1093 - 1101$.

George W.K., Hussein H.J., (1991). Locally axisymmetric turbulence. *J Fluid Mech*, 233, $1 - 23$.

Gore R.A., Crowe C.T., (1991). Modulation of turbulence by a dispersed phase. *J Fluid Eng-T ASME*, 113(2), $304 - 307$.

Gray W.G., Hassanizadeh S.M., (1998). Macroscale continuum mechanics for multiphase porous-media flow including phases, interfaces, common lines and common points. *Adv Water Resour*, 21, $261 - 281$.

Han N.-W., Bhakta J., Carbonell R.-G., (1985). Longitudinal and lateral dispersion in packed beds: effect of column length and particle size distribution. *AIChE J*, 31(2) , $277 - 288$.

Häfeli R., Hutter C., Damsohn M., Prasser H.-M., Rudolf von Rohr Ph., (2013). Dispersion in fully developed flow through regular porous structures: Experiments with wire-mesh sensors. *Chem Eng Process*, 69, $104 - 111$.

Häfeli R., Altheimer M., Butscher D., Rudolf von Rohr Ph., (2014). PIV study of flow through porous structure using refractive index matching. *Exp Fluids*, 55 : 1717.

Harned H., Nuttall R. L., The diffusion coefficient of potassium chloride in dilute aqueous solutions. *J American Chem Soc*, 69 (1947), $736 - 740$.

Hirech K., Arhaliass A., Legrand J., (2003). Experimental investigation of flow regimes in an SMX Sulzer static mixer. *Ind Eng Chem Res*, 42, $1478 - 1484$.

Hlushkou D., Tallarek U., (2006).Transition from creeping via viscous-inertial to turbulent flow in fixed beds. *J Chromatogr A*, 1126, $70 - 85$.

Honkanen M., Saarenrinne P., Stoor T., Niinimäki J., (2005). Recognition of highly overlapping ellipse-like bubble images. *Meas Sci Technol.*, 16, $1760 - 1770$.

Horneber T., Rauh C., Delgado A., (2012). Fluid dynamic characterisation of porous solids in catalytic fixed-bed reactors. *Microporous Mesoporous Mater*, 154, $170 - 174$.

Hull D.E., Kent J.W., (1952). Radioactive tracers to mark interfaces and measure intermixing in pipelines. *Ind Eng Chem*, 44(11), $2745 - 2750$.

Hutter C., Allemann C., Kuhn S., Rudolf von Rohr Ph., (2010). Scalar transport in a milli-scale metal foam reactor. *Chem Eng Sci*, 65, 3169−3178.

Hutter C., Zenklusen A., Lang R., Rudolf von Rohr Ph., (2011*a*). Axial dispersion in metal foams and streamwise-periodic porous media. *Chem Eng Sci*, 66, 1132 − 1141.

Hutter C., Zenklusen A., Kuhn S., Rudolf von Rohr Ph., (2011*b*). Large eddy simulation of flow through a streamwise-periodic structure. *Chem Eng Sci*, 66, 519 − 529.

Hutter C., Büchi D., Zuber V., Rudolf von Rohr Ph., (2011*c*). Heat transfer in metal foams and designed porous media. *Chem Eng Sci*, 66, 3806 − 3814.

Hutter C., (2010). *Laser sintered meso scale reactor by design: characterization of heat and mass transfer* (Doctoral dissertation). ETH Zürich, Switzerland.

Jolls K.R., Hanratty T.J., (1966). Transition to turbulence for flow through a dumped bed of spheres. *Chem Eng Sci*, 21, 1185 − 1190.

Jones W.P., Launder B.E., (1972). The prediction of laminarization with a two-equation model of turbulence. *Int J Heat Mass Tran*, 15, 301 − 314.

de Jong J., Cao L., Woodward S.H., Salazar J.P.L.C., Collins L.R., Meng H., (2009). Dissipation rate estimation from PIV in zero-mean isotropic turbulence. *Exp Fluids*, 46, 499 − 515.

Kaviany M., (1991). *Principles of heat transfer in porous media*. New York: Springer-Verlag.

Koch D. L., Brady J. F., Dispersion in fixed beds. *J Fluid Mech*, 154 (1985), 399 − 427.

Koch D. L., Brady J. F., Nonlocal dispersion in porous media: nonmechanical effects. *Chem Eng Sci*, 42 (1987), 1377 − 1392.

Kockmann N., Gottsponer M., Zimmermann B., Roberge D.M., (2008). Enabling continuous-flow chemistry in microstructured devices for pharmaceutical and fine-chemical production. *Chem Eur J*, 14, 7470 − 7477.

Kong X.Z., Holzner M., Stauffer F., Kinzelbach W., (2011). Time-resolved 3D visualization of air injection in a liquid-saturated refractive-index-matched porous medium. *Exp Fluids*, 50, 1659 − 1670.

Krummel A.T., Datta S.S., Münster S., Weitz D.A., (2013). Visualizing multiphase flow and trapped fluid configurations in a model three-dimensional porous medium. *AIChE J*, 59(3), 1022 − 1029.

Kumara W.A.S., Halvorsen B.M., Melaaen M.C., Computational study on non-asymptotic behaviour of developing turbulent pipe flow. *Advances in Fluid Mechanics VIII*, 69 (2010), 39 − 52.

Latifi M.A., Midoux N., Storck A., Gence J.N., (1989). The use of micro-electrodes in the study of the flow regimes in a packed bed reactor with single phase liquid flow. *Chem Eng Sci*, 44, 2501 − 2508.

Launder B.E., Sharma B.I., (1974). Application of the energy-dissipation model of turbulence to the calculation of flow near a spinning disc. *Lett Heat Mass Trans*, 1, 131 − 138.

Legrand J., Morançais P., Carnelle G., Liquid/liquid dispersion in an SMX-Sulzer static mixer. *Chem Eng Res Des*, 79(8) (2001), 949 − 956.

Lelouvetel J., Nakagawa M., Sato Y., Hishida K., (2011). Effect of bubbles on turbulent kinetic energy transport in downward flow measured by time-resolved PTV. *Exp Fluids*, 50, 813 − 823.

Lemenand T., Della Valle D., Zellouf Y., Peerhossaini H., Droplets formation in turbulent mixing of two immiscible fluids in a new type of static mixer. *Int. J. Multiphase Flow*, 29 (2003), 813 − 840.

Levenspiel O., Smith W.K., Notes on the diffusion-type model for the longitudinal mixing of fluids in flow. *Chem Eng Sci*, 6 (1957), 227−235.

Levenspiel O., Chemical Reaction Engineering. 3rd ed. John Wiley and Sons, 1999.

Lindken R., Gui L., Merzkirch W., (1999). Velocity measurements in multiphase flow by means of particle image velocimetry. *Chem Eng Technol*, 22, 202 − 206.

Liu L., Matar O.K., Perez de Ortiz E.S., Hewitt G.F., (2005). Experimental investigation of phase inversion in a stirred vessel using LIF. *Chem Eng Sci*, 60, 85 − 94.

Melling A., (1997). Tracer particles and seeding for particle image velocimetry. *Meas Sci Technol*, 8, 1406 − 1416.

Middleman S., 1974. Drop size distributions produced by turbulent pipe flow of immiscible fluids through a static mixer. *Ind. Eng. Chem. Proc. D.D.*, 13(1), 78 − 83

Mills P.L., Chaudhari R.V., (1997). Multiphase catalytic reactor engineering and design for pharmaceuticals and fine chemicals. *Catal Today*, 37, 367 − 404.

Mokrani A., Castelain C., Peerhossaini H., Experimental study of the influence of the rows of vortex generators on turbulence structure in a tube. *Chem Eng Proc*, 48 (2009), 659 − 671.

Montemagno C.D., Gray W.G., (1995). Photoluminescent volumetric imaging: a technique for the exploration of multiphase flow and transport in porous media. *Geophy Res Lett*, 22(4), 425 − 428.

Morancais P., Hirech K., Carnelle G., Legrand J, (1999). Friction factor in static mixer and determination of geometric parameters of SMX Sulzer mixers. *Chem Eng Comm*, 171, 77 − 93.

Morgan R.G., Markides C.N., Zadrazil I., Hewitt G.F., (2013). Characteristics of horizontal liquid-liquid flows in a circular pipe using simultaneous high-speed laser-induced fluorescence and particle velocimetry. *Int J Multiphase Flow*, 49, 99 − 118.

Narrow T.L., Yoda M., Abdel-Khalik S.I., (2000). A simple model for the refractive index of sodium iodide aqueous solutions. *Exp Fluids*, 28, 282 − 283.

Ng K.M., Davis H.T., Scriven 1L.E., (1978). Visualization of blob mechanics in flow through porous media. *Chem Eng Sci*, 33, $1009 - 1017$.

Ovdat H., Berkowitz B., (2006). Pore-scale study of drainage displacement under combined capillary and gravity effects in index-matched porous media. *Water Resour Res*, 42, $W06411$.

Perrot C., Panneton R., Olny X., (2007). Periodic unit cell reconstruction of porous media: Application to open-cell aluminum foams. *J Appl Phys*, 101(11), 113538.

Petrasch J., Schrader B., Wyss P., Steinfeld A., (2008). Tomography-based determination of the effective thermal conductivity of fluid-saturated reticulate porous ceramics. *J Heat Transf*, 130, 032602.

Pfannkuch H.O., (1963). Contribution a l'étude des déplacements de fluides miscibles dans un milieu poreux. *Rev I Fr Petrol*, 18(2), $215 - 270$.

Piela K., Delfos R., Ooms G., Westerweel J., Oliemans R.V.A., Mudde R.F., (2006). Experimental investigation of phase inversion in an oil-water flow through a horizontal pipe loop. *Int J Multiphase Flow*, 32, $1087 - 1099$.

Prasser H.-M., Böttger A., Zschau J., (1998). A new electrode-mesh tomograph for gas-liquid flows. *Flow Meas Instrum*, 130, 032602.

Prasser H.-M., Misawa M., Tiseanu I., (2005). Comparison between wire-mesh sensor and ultra-fast X-ray tomograph for an air-water flow in a vertical pipe. *Flow Meas Instrum*, 16, $73 - 83$.

Roberge D.M., Ducry L., Bieler N., Cretton Ph., Zimmermann B., (2005). Microreactor technology: a revolution for the fine chemical and pharmaceutical industries? *Chem Eng Technol*, 28(3), $318 - 323$.

Saarenrinne P., Piirto M., (2000). Turbulent kinetic energy dissipation rate estimation from PIV velocity vector fields. *Exp Fluids*, 29(1), $S300 - S307$.

Saarenrinne P., Piirto M., Eloranta H., (2001). Experiences of turbulence measurement with PIV. *Meas Sci Technol*, 12, $1904 - 1910$.

Sabatino D.R., Praisner T.J., Smith C.R., (2000). A high-accuracy cali-
bration technique for thermochromic liquid crystal temperature mea-
surements. *Exp Fluids*, 28, $497 - 505$.

Sahimi M., (1995). *Flow and transport in porous media and fractured
rock*. Weinheim: VCH.

Salami L.A., (1986). An investigation of turbulent developing flow at the
entrance to a smooth pipe. *Int J Heat Fluid Fl*, 7(4), $247 - 257$.

Schenk R., Hessel V., Hofmann C., Kiss J., Löwe H., Ziogas A., (2004).
Numbering-up of micro devices: a first liquid-flow splitting unit. *Chem
Eng J*, $101(1 - 3)$, $421 - 429$.

Seguin D., Montillet A., Comiti J., (1998*a*). Experimental characterisa-
tion of flow regimes in various porous media - I:Limit of laminar flow
regime *Chem Eng Sci*, 53(21), $3751 - 3761$.

Seguin D., Montillet A., Comiti J., Huet F., (1998*b*). Experimental char-
acterisation of flow regimes in various porous media - II: Transition to
turbulent regime *Chem Eng Sci*, 53(22), $3897 - 3909$.

Sharp K.V., Adrian R.J., (2001). PIV study of small-scale flow structure
around a Rushton turbine. *AIChE J*, 47(4), $766 - 778$.

Sprow F.B., (1967). Distribution of drop sizes produced in turbulent
liquid-liquid dispersion. *Chem. Eng. Sci.*, 22, $435 - 442$.

Stankiewicz A., Moulijn J.A., (2004). *Re-engineering the chemical pro-
cessing plant*. New York: Marcel Dekker Inc.

Stemmet C.P., Jongmans J.N., van der Schaaf J., Kuster B.F.M.,
Schouten J.C., (2005). Hydrodynamics of gas-liquid counter-current
flow in solid foam packings. *Chem Eng Sci*, 60, $6422 - 6429$.

Stitt E.H., (2002). Alternative multiphase reactors for fine chemicals. A
world beyond stirred tanks? *Chem Eng J*, 90, $47 - 60$.

Stöhr M., Roth K., Jähne B., (2003). Measurement of 3D pore-scale flow
in index-matched porous media. *Exp Fluids*, 35, $159 - 166$.

Streiff F.A., Jaffer S., Schneider G., (1999). The design and application of static mixer technology. *Proceedings of 3rd International Symposium on Mixing in Industrial Processes, Osaka, Japan*, $107 - 114$.

Svensson F.J.E., Rasmuson A., (2006). PIV measurement in a liquid-liquid system at volume percentages up to 10% dispersed phase. *Exp Fluids*, 41, $917 - 931$.

Taylor G., (1953). Dispersion of soluble matter in solvent flowing slowly through a tube. *P Roy Soc Lond A Mat*, 219(1137), $186 - 203$.

Taylor G., (1954). The dispersion of matter in turbulent flow through a pipe. *Proc R Soc Lond A*, 223(1155), $446 - 468$.

Thakur R.K., Vial Ch., Nigam K.D.P., Nauman E.B., Djelveh G., (2003). Static mixers in the process industries - a review. *Trans IChemE*, 81(7), $787 - 826$.

Theron F., Le Sauce N., (2011). Comparison between three static mixers for emulsification in turbulent flow. *Int. J. Multiphase Flow*, 37, $488 - 500$.

Trachsel F., Günther A., Khan S., Jensen K.F., (2005). Measurement of residence time distribution in microfluidic systems. *Chem Eng Sci*, 60, $5729 - 5737$.

Unadkat H., Rielly C.D., Hargrave G.K., Nagy Z.K., (2009). Application of fluorescent PIV and digital image analysis to measure turbulence properties of solid-liquid stirred suspensions. *Chem Eng Res Des*, 87, $573 - 586$.

Wadley R., Dawson M.K., (2005). LIF measurements of blending in static mixers in the turbulent and transitional flow regimes. *Chem Eng Sci*, 60, $2469 - 2478$.

Wegner T.H., Karabelas A.J., Hanratty T.J., (1971). Visual studies of flow in a regular array of spheres. *Chem Eng Sci*, 26, $59 - 63$.

Weir J., Priest A.J., Sharan V.K., (1974). The effect of inlet disturbances on turbulent pipe flow. *J Mech Eng Sci*, 16(3), $211 - 213$.

Wiberg R., Lior N., (2004). Errors in thermochromic liquid crystal thermometry. *Rev Sci Instrum*, 75(9), $2985 - 2994$.

Wiederseiner S., Andreini N., Epely-Chauvin G., Ancey C., (2011). Refractive-index and density matching in concentrated particle suspensions: a review. *Exp Fluids*, 50, $1183 - 1206$.

Xu D., Chen J., (2013). Accurate estimate of turbulent dissipation rate using PIV data. *Exp Therm Fluid Sci*, 44, $662 - 672$.

Zenklusen A., Kenjeres S., Rudolf von Rohr Ph., (2014). Vortex shedding in a highly porous structure. *Chem Eng Sci*, 106, $253 - 263$.

List of publications

Journal publications

1. Häfeli R., Rüegg O., Altheimer M., Rudolf von Rohr Ph., (2015). Investigation of emulsification in static mixers by optical measurement techniques using refractive index matching. *submitted*.

2. Häfeli R., Altheimer M., Butscher D., Rudolf von Rohr Ph., (2014). PIV study of flow through porous structure using refractive index matching. *Exp Fluids*, 55 : 1717.

3. Häfeli R., Hutter C., Damsohn M., Prasser H.-M., Rudolf von Rohr Ph., (2013). Dispersion in fully developed flow through regular porous structures: Experiments with wire-mesh sensors. *Chem Eng Process*, 69, $104 - 111$.

Conference contributions

1. Häfeli R., Ph. Rudolf von Rohr. Total thermal diffusivity in a porous structure measured by full field liquid crystal thermography. *International Conference on Heat Transfer and Fluid Flow (HTFF14)*, Prague, 2014.

2. Häfeli R., Altheimer M., Ph. Rudolf von Rohr. Dependence of mass transport on the length of a tubular reactor with a porous structue. 9th *World Congress of Chemical Engineering (WCCE 9)*, Seoul, 2013.

3. Häfeli R., Elias Y., Hutter C., Ph. Rudolf von Rohr. Flow characterisation in designed porous structures. 9th *International Symposium on the Characterisation of Porous Solids (COPS IX)*, Dresden, 2011.

Curriculum Vitae

Richard Häfeli

Date of birth:	October 19, 1985
Place of birth:	St.Gallen, Switzerland
Nationality:	Swiss
2010–2015	Doctoral studies at the Institute of Process Engineering, ETH Zurich (Prof. Dr. Ph. Rudolf von Rohr)
2009–2010	Master studies in Process Engineering, ETH Zürich (academic degree: MSc ETH PE)
2008–2009	Internship at Alstom Power, Baden, Switzerland
2005–2008	Bachelor studies in Mechanical Engineering, ETH Zürich (academic degree: BSc ETH ME)
2004–2005	Military service
2000–2004	Kantonsschule am Burggraben, St.Gallen (academic degree: Matura)
1992–2000	Primary school, St.Gallen

Zurich, July 2015